Global surface urban heat islands research for the spatiotemporal dynamics and driving factors

Menglin Si

UNIVERSITÉ DE STRASBOURG

ÉCOLE DOCTORALE MSII (ED n°269)

Laboratoire des sciences de l'ingénieur, de l'informatique et de l'imagerie (ICUBE) - UMR 7357

THÈSE

présentée par :

Menglin SI

soutenue le : **22 December 2021**

pour obtenir le grade de : **Docteur de l'université de Strasbourg**

Discipline : Sciences de l'imagerie

Spécialité : Télédétection

Global surface urban heat islands research for the spatiotemporal dynamics and driving factors

THÈSE dirigée par :

Mme Françoise NERRY	Directeur de Recherches, CNRS, France

RAPPORTEURS :

M. José SOBRINO	Professeur, Université de Valence, Espagne
Mme Lingling MA	Directeur de Recherches, CAS, Chine

AUTRES MEMBRES DU JURY :

M. Georges NAJJAR	Directeur de Recherches, CNRS, France
M. Guangjian YAN	Professeur, Université Normale de Beijing, Chine
M. Zhao-Liang LI	Directeur de Recherches, CNRS, France

Acknowledgements

From the very beginning of my thesis, I wish to acknowledge with my sincere gratitude to everyone I met and everything I experienced in this journey.

First and foremost, I would like to extend my most sincere gratitude to my supervisor Pr. NERRY Françoise. During my doctoral study, I was deeply impressed by her profound academic attainments, rigorous academic attitude, and open-minded personality. Whenever I got confused, Pr. NERRY would ignite the spark of wisdom with her keen perspective to uncover the essence of the scientific issues. Thank you for your meticulous guidance, which finally made me better on the road of scientific research.

Second, I would like to thank my dearest colleagues in our team – TRIO/ICube - for being so kind and generous. Special thanks to Pr. LI Zhao-Liang, Pr. YÉSOU Hervé, and Pr. COLIN Jérôme for their kind help during my research.

Third, I would like to thank the reporters of my thesis, M. José SOBRINO and Mme Lingling MA; and the jury members, M. Georges NAJJAR, M. Guangjian YAN, M. Zhao-Liang LI, and Mme F. NERRY; for their valuable comments, which are really helpful for this thesis as well as for my future researches.

Four, I would like to thank all the Ph.D students I met here in France: Changsen ZHAO, Yazhen JIANG, Xiaopo ZHENG, Xinyu LAN, Xiangyang LIU, Zefeng XING, Hongyu LI, Jing LI, Lei HE, Mingsong LI, Ling WU, Ying YANG, et. al, for their help, encouragement, and the memorable times we have spent together. Special thanks to Dr. Xiaopo ZHENG and Dr. Xinyu LAN for their very kind assistants at the very beginning of my doctoral study in France. With their help, I could get adapt to the new life quickly.

Five, the financial support by China Scholarship Council (CSC) is quite appreciated. Without the generous funding support from my country, I can never get the opportunity to complete my doctoral study in France.

Last but not least, I would like to thank my parents for their unconditional support and endless love, which enable me to focus on my study and research.

Abstract

In the context of accelerating urbanization and global warming, the urban heat island effect has gradually become an urban thermal environmental problem that has been widely concerned by academia and even the whole society. With the development of satellite remote sensing technology, a large number of studies have focused on the surface urban heat islands (SUHI) phenomenon at multiple temporal and spatial scales around the world. However, the systematic research on global SUHI is lacking. The quantification of SUHI intensity (SUHII) has generally ignored the dynamic land use change and needs to be unified. In addition, as the urban background climate and urbanization process have a significant impact on the driving mechanism of SUHI, the spatial non-stationarity of them has not yet been fully explored. Given these problems, this paper first constructed a global long-term SUHII database to analyze its spatial pattern and temporal dynamics at multiple scales. With that, the potential driving factors were employed to analyze the driving mechanism of global SUHII under different background conditions based on the surface energy balance model. Subsequently, a multiscale spatial statistical model was adopted to quantitatively analyze the effect of urbanization and background climate condition and its spatiotemporal non-stationarity. Finally, the indices to quantify SUHII with different rural land use types were constructed to verify the feasibility of the urban-rural temperature difference method in regional studies, meanwhile reveal the spatiotemporal pattern of SUHI in 34 China's major cities. The main content of this paper is presented as follows.

(1) The yearly urban and rural range of global urban/urban agglomerations were identified based on the city clustering algorithm with the help of the Google Earth Engine (GEE) cloud computing platform. The spatial and temporal patterns of global SUHII from 2003 to 2019 was presented at annual, summer, winter and monthly averaged scales. Afterwards, the regional effects of SUHII were revealed along with the latitudinal and climatic zones. Finally, the inter-annual trends of global SUHII were disclosed at different temporal scales. The results have shown that the global annual daytime and nighttime SUHII are 0.97 ℃ and 0.94 ℃, respectively; the global SUHI has significant latitudinal

variability, climatic differences and seasonal variations; Both annual and summer daytime SUHII have a significant increase trend during the year 2003 and 2019 with the changing rate of 0.05 ℃/decade and 0.11 ℃/decade, respectively. The winter daytime SUHII has a decrease trend at the slope of -0.03 ℃/decade. While at night, only summer SUHII has significant increase trend with inconspicuous slope of 0.02 ℃/decade.

(2) Based on the surface energy balance equation, the surface vegetation index, surface albedo index, precipitation, wind speed, population density and city size were selected as potential factors to affect SUHII at annual average, summer average, winter average, and diurnal scales. The contribution of multiple factors was explored from global to regional scales. The results show that the difference of surface vegetation index between urban and rural is negatively correlated with daytime SUHII; the difference of white-sky albedo between urban and rural surface is positively correlated with daytime SUHII and negatively correlated with nighttime SUHII; the mean precipitation is positively correlated with daytime SUHII and is negatively correlated with nighttime SUHII; the average wind speed mainly have a negative contribution to SUHII, and the positive correlation between population density and urban area size and SUHII is more significant at night. The interannual trends of daytime and nighttime SUHIIs were negatively dominated by the slope of vegetation condition (ΔEVI) and the slope of physical properties (ΔWSA), respectively. The contribution rates are 34%, 54%, and 38% (daytime), and 17%, 33%, and 22% (nighttime), for annual, summer, and winter scales, respectively. Based on the multiscale geographically weighted regression model, the spatial non-stationarity of these driving factors on SUHII was explored.

(3) 34 major cities in China were picked out to analyze the changes in their urban form and scale from 2003 to 2019. The results show that most cities have significant urban expansion trend. It supports the necessity of defining the dynamic urban-rural scope in the quantification of SUHI. Subsequently, SUHII was quantified by different rural land use types to verify the feasibility of the urban-rural temperature difference method. Finally, the multi-scale analysis of SUHII in China's sub-regions reveals that the SUHII quantified with the entire rural land use type is not affected by diverse land use when exploring regional temporal and spatial patterns.

Keywords: Global surface urban heat island, Spatiotemporal dynamic, Driving factors, Google Earth Engine

Résumé

Dans un contexte d'accélération de l'urbanisation et de réchauffement climatique, l'effet d'îlot de chaleur urbain est progressivement devenu un problème environnemental thermique urbain largement concerné par le monde universitaire voire la société tout entière. Avec le développement de la technologie de télédétection par satellite, un grand nombre d'études se sont concentrées sur le phénomène des îlots de chaleur urbains de surface (SUHI) à de multiples échelles temporelles et spatiales à travers le monde. Cependant, la recherche systématique sur le SUHI mondial fait défaut. La quantification de l'intensité SUHI (SUHII) a généralement ignoré le changement dynamique d'utilisation des terres et doit être unifiée. De plus, comme le climat de fond urbain et le processus d'urbanisation ont un impact significatif sur le mécanisme de conduite de SUHI, leur non-stationnarité spatiale n'a pas encore été pleinement explorée. Compte tenu de ces problèmes, cet article a d'abord construit une base de données SUHII mondiale à long terme pour analyser son modèle spatial et sa dynamique temporelle à plusieurs échelles. Avec cela, les facteurs moteurs potentiels ont été utilisés pour analyser le mécanisme moteur du SUHII global dans différentes conditions de fond sur la base du modèle de bilan énergétique de surface. Par la suite, un modèle statistique spatial multi-échelle a été adopté pour analyser quantitativement l'effet de l'urbanisation et des conditions climatiques de fond et sa non-stationnarité spatio-temporelle. Enfin, les indices pour quantifier SUHII avec différents types d'utilisation des terres rurales ont été construits pour vérifier la faisabilité de la méthode de différence de température urbaine-rurale dans les études régionales, tout en révélant le modèle spatio-temporel de SUHI dans 34 grandes villes chinoises. Le contenu principal de cet article est présenté comme suit.

(1) La portée annuelle urbaine et rurale des agglomérations urbaines mondiales a été identifiée sur la base de l'algorithme de regroupement des villes à l'aide de la plateforme informatique Google Earth Engine (GEE). Les modèles spatiaux et temporels du SUHII mondial de 2003 à 2019 sont présentés à des échelles annuelles, estivales, hivernales et mensuelles. Ensuite, les effets régionaux de SUHII sont montrés en fonction des zones

latitudinales et climatiques. Enfin, les tendances interannuelles du SUHII global ont été révélées à différentes échelles temporelles. Les résultats ont montré que le SUHII diurne et nocturne annuel global est de 0,97 °C et 0,94 °C, respectivement; le SUHI global a une variabilité latitudinale, des différences climatiques et des variations saisonnières significatives; le SUHII diurne annuel et estival a une tendance significative à l'augmentation au cours des années 2003 et 2019 avec un taux de changement de 0,05 °C/décennie et 0,11 °C/décennie, respectivement. Le SUHII diurne d'hiver a une tendance à la baisse avec une pente de -0,03 °C/décennie alors que la nuit, seul le SUHII d'été a une tendance significative à l'augmentation avec une pente discrète de 0,02 °C/décennie.

(2) Sur la base de l'équation du bilan énergétique de surface, l'indice de végétation de surface, l'albédo de surface, les précipitations, la vitesse du vent, la densité de population et la taille des villes ont été sélectionnés comme facteurs potentiels pouvant affecter le SUHII aux échelles de moyenne annuelle, de moyenne estivale et de moyenne hivernale et diurne. La contribution de plusieurs facteurs a été étudiée de l'échelle globale à l'échelle régionale. Les résultats montrent que la différence d'indice de végétation de surface entre les zones urbaines et rurales est négativement corrélée avec le SUHII diurne; la différence d'albédo du ciel blanc entre les zones urbaines et rurales est positivement corrélée avec le SUHII diurne et négativement corrélée avec le SUHII nocturne; les précipitations moyennes sont positivement corrélées avec le SUHII diurne et négativement corrélées avec le SUHII nocturne; la vitesse moyenne du vent a principalement une contribution négative au SUHII, et la corrélation positive entre la densité de population et la taille de la zone urbaine et le SUHII est plus significative la nuit. La corrélation positive entre la densité de population, la taille de la zone urbaine et l'indice SUHII est plus importante la nuit. Sur la base du modèle de régression multi-échelle géographiquement pondéré, la non-stationnarité spatiale de ces facteurs sur l'indice SUHII a été étudiée.

(3) 34 grandes villes de Chine ont été sélectionnées pour analyser les changements de leur forme urbaine et de leur échelle entre 2003 et 2019. Les résultats montrent que la plupart des villes ont une tendance significative à l'expansion urbaine. Ils confirment la nécessité de définir l'étendue dynamique urbaine-rurale dans la quantification du SUHI. Par

la suite, le SUHII a été quantifié pour différents types d'utilisation des terres rurales afin de vérifier la faisabilité de la méthode de la différence de température urbaine-rurale. Enfin, l'analyse multi-échelle du SUHII dans les sous-régions de la Chine révèle que le SUHII quantifié avec l'ensemble du type d'utilisation des terres rurales n'est pas affectée par la diversité de l'utilisation des terres lors de l'exploration des modèles temporels et spatiaux régionaux.

Mots-clés: Surface d'îlot de chaleur urbain mondial, Dynamique spatio-temporelle, Facteurs moteurs, Google Earth Engine

List of abbreviations

LST	Land surface temperature
UHI	Urban heat island
SUHI	Surface urban heat island
SUHII	Surface urban heat island intensity
MODIS	Moderate Resolution Imaging Spectroradiometer
LULC	Land use and land cover
EVI	Enhance vegetation index
WSA	White-sky albedo
DEM	Digital elevation model
DUE	Dynamic urban-extent
SUE	Simplified urban-extent
CCA	City clustering algorithms
SEB	surface energy balance
ΔEVI	EVI differences between urban and rural regions
ΔWSA	WSA differences between urban and rural regions
MAP	Mean urban precipitation
WS	Mean urban wind speed
PD	Mean urban population density
UA	Urban area
OLS	Ordinary least squares
GWR	Geographically weighted regression
MGWR	Multi-scale geographically weighted regression
VIF	Variance Inflation Factor
AD	Annual daytime
AN	Annual nighttime
SD	Summer daytime

SN	Summer nighttime
WD	Winter daytime
WN	Winter nighttime

Contents

List of Figures

List of Tables

1 Introduction

1.1. Background

Since the beginning of the 21st century, rapid urbanization has caused tremendous pressure on the urban ecological environment (Vitousek et al., 1997). Urban population is increasing continuously, and is expected to increase from the present 55% to nearly 70% by 2050 (United-Nations, 2019). Urban expansion and its associated anthropogenic activities regularly influence the ground surface properties and urban climate conditions, thereby disturbing the surface energy balance (Grimm et al., 2008b). Consequently, the phenomenon of urban heat island (UHI), in which urban regions are warmer than their neighboring hinterlands, occurs in most global cities and urban clusters. The UHI effect can threaten the sustainable development of mankind and has gradually become an urban thermal environmental problem widely concerned by academia and even the whole society; therefore, scientific characterization of the global UHI patterns under a systematic research framework is urgently required (Oke, 1982; Bai et al., 2018).

In early years, the UHI effect has been quantified using air temperature records acquired from ground observations across urban zones and their vicinities, a phenomenon known as canopy UHI (Arnfield, 2003). Remote sensing technology can overcome the limitations of the ground observations, by providing sufficient land surface temperature (LST) data, thus, encouraging the study of the surface UHI (SUHI) through new perspectives (Jin, 2012). Up to present, multiple studies on the SUHI spatiotemporal patterns, driving mechanisms, and mitigation strategies, ranging from local, national, and regional to global scales, have been reported based on satellite data (Quan et al., 2014; Zhou et al., 2014a; Peng et al., 2018b; Yu et al., 2019; Zhou et al., 2013; Peng et al., 2012; Clinton and Gong, 2013). Specifically, satellite-based LST data is preferred for research on global

SUHI since it has the advantages of large-scale spatial coverage (Peng et al., 2012; Clinton and Gong, 2013; Chakraborty and Lee, 2019). However, systematic research on global SUHI still needs to be further expanded. To better investigate the global SUHI dynamics and reveal potential findings, improvements on the quantifications of long-term SUHI with rapid urbanization, and an increased time range with expanded research coverage are required.

First, the systematic research on global SUHI is to be enriched.

Depicting the characteristics of global SUHI in recent years as a hot spot involving the urban thermal environment and human well-being is essential. However, the SUHI phenomenon in developing or developed countries in Asia, North America, and Europe has received more attention, while that in the underdeveloped countries in Africa, South America, and Oceania, have rarely been investigated (Zhou et al., 2019; Li et al., 2020c; Simwanda et al., 2019). Moreover, most SUHI studies have focused on a single city or representative cities and urban clusters on a national or regional scale (Sun et al., 2020; Li et al., 2020b; Hu et al., 2019; Yue et al., 2019; Sun et al., 2019; Lai et al., 2021), whereas long-term SUHI research in multi-cities on a global scale has been less conducted (Wu and Ren, 2019). The limited global studies (Zhang et al., 2010; Peng et al., 2012; Clinton and Gong, 2013) did not completely analyze the long-term evolution of SUHI or its driving factors. Therefore, it is necessary to improve the ongoing research by exploiting the most comprehensive and retrievable LST dataset to explore the global SUHI at multiple spatial and temporal scales.

Second, the quantification of SUHI intensity has generally ignored the dynamic land use change and need to be unified.

Two quantification methods exist for calculating SUHI intensity (SUHII) using either land use/land cover (LULC) or LST patterns. Other than the massive computation process in LST pattern methods (Zhou et al., 2016c; Rajasekar and Weng, 2009; Quan et al., 2014; Anniballe and Bonafoni, 2015), the LST difference method based on the LULC were generally employed; that is, the rural LST was subtracted from urban LST to indicate the

SUHII (Zhou et al., 2015; Santamouris, 2015; Yao et al., 2018b; Yao et al., 2017; Chakraborty et al., 2020). After identifying the urban clusters, a buffer at a fixed distance from the urban center or an area with a fixed multiple of the urban area is generally defined as its rural region. It is convenient and proved feasible to provide reliable results for global SUHI (Peng et al., 2012; Clinton and Gong, 2013; Zhou et al., 2014a). Generally, the urban and rural was identified by differentiating the continuous urban regions from rural pixels enclosed in fixed urban boundaries (Chakraborty and Lee, 2019). However, with the recent urban development, urban regions expand considerably, which can probably lead to imprecise results in qualifying SUHI, especially over rapidly-expanding regions. It supports the necessity of defining the dynamic urban-rural scope in the quantification of SUHI. Moreover, the rural pixels close to the urban cluster will overestimate the rural background LST, as a consequence need to be purified. Therefore, it is necessary to quantify the SUHI by improved scheme by better capturing the urban sprawl to reveal the spatiotemporal variations of long-term SUHI in the urbanization process.

Third, the driving factors of global SUHI and its spatial non-stationarity needs to be fully explored.

The phenomenon of UHI is an intuitive reflection of the impact of human activities on the urban climate. The crucial driving factors for SUHI have been explored by combing global products involving meteorology, urbanization and human activity with statistical models for decades(Weng et al., 2004; Yang et al., 2017; Peng et al., 2018a; Wang and Shu, 2020). However, the global SUHI is not only affected by the surface properties and human activities, but also exhibits different spatiotemporal response under different background climate conditions (Chapman et al., 2017). The spatially varied driving mechanisms for global SUHI in different geographic regions still need to be further detected (Li et al., 2020a). Moreover, the relationship between spatially distributed SUHII and associated drivers may not necessarily be consistent with the relationships between interannual variations in SUHII and its associated factors for certain cities across years (Yao et al., 2018b). Specifically, few studies have concerned on the driving factors for long-term

SUHII dynamics at global scale. Therefore, it is necessary to employ advanced analytical method to explore the driving factors for SUHII from not only spatial but also temporal perspectives with the urbanization process.

Fourth, **the effect of multiple rural land types on the quantification of SUHII needs to be verified in support of the large-scale SUHI studies.**

In the SUHII quantification, the differences in the rural and urban LST depended on the LULC information. Since the LST variations in urban clusters are generally minor, the definition of "rural" regions is crucial for rationally quantifying SUHII (Martin-Vide et al., 2015). The rural LST with compound LULC types uses rural pixels of different LULC types is probably to produce different SUHIIs for a single city (Zhou et al., 2016c). The similarities and differences between the SUHII quantified by "full rural" and "rural with certain land use" was unclear. In a large-scale study, the problem of whether the spatial and temporal pattern of regional SUHII quantified using all the rural LULC types is feasible and not affected by the heterogeneity of rural LST has rarely been investigated. Therefore, it is necessary to construct new indices for SUHI quantification under different rural background to verify the reliability and feasibility of urban rural difference methods in global SUHI study.

1.2. Objective and structure of this thesis

This thesis is dedicated to the investigation of the spatiotemporal patterns of global surface urban heat islands from 2003 to 2019 by an improved dynamic urban extent scheme, whereafter to explore the driving factors for the spatial variations and long-term trends of SUHII, the final purpose of which is to enhance the systemic research on global SUHI and provide indications for SUHI mitigation in urban planning.

Specifically, three research objectives have been involved in this thesis as below:

(1) Firstly, a global long-term SUHII database is built to analyze its spatial pattern and temporal dynamics at multiple scales.

(2) Secondly, the potential driving factors is to be employed to analyze the driving mechanism of global SUHII from spatial and temporal perspectives. Meanwhile, the multiscale spatial statistical model is adopted to quantitatively analyze the spatiotemporal non-stationarity of multiple factors.

(3) Finally, the indices to quantify SUHI with different rural land use types needs to be constructed to verify the feasibility of the urban-rural temperature difference method in regional SUHI studies.

Following the research objectives, the main content of this thesis is organized into six chapters as follows.

Chapter 1 gives a brief introduction on the backgrounds, research meanings, and the objectives of this thesis.

Chapter 2 presents the information of study area and main data sources. Firstly, the principals for determining the study area, and the spatial pattern and population size of target cities are introduced. Secondly, the remote sensing image data, meteorological data, population data, and so forth, involved in this study are described in detail.

In chapter 3, the yearly urban and rural range of global urban/urban agglomerations were identified based on the improved dynamic urban-extent (DUE) scheme. The spatial and temporal patterns of global SUHII from 2003 to 2019 was presented at annual, summer, winter and monthly averaged scales. Afterwards, the regional contrasts of SUHII were revealed along with the latitudinal and climatic zones. Finally, the inter-annual trends of global SUHII were disclosed at different temporal scales.

In chapter 4, based on the surface energy balance equation, the factors in in terms of surface properties, climate condition and urbanization process were selected as potential drivers for SUHII at annual average, summer average, winter average, and diurnal scales. The contribution of multiple factors was explored from spatial and temporal perspectives, separately. Based on the multiscale geographically weighted regression model, the spatial non-stationarity of these driving factors on SUHII was explored.

In chapter 5, several major cities in China were picked out to analyze the changes in their urban form and scale from 2003 to 2019. SUHII was quantified by different rural land use types to verify the feasibility of the urban-rural temperature difference method. Subsequently, Finally, the multi-scale analysis of SUHII in China's sub-regions reveals that the SUHII quantified with the entire rural land use type is not affected by diversity land use when exploring regional temporal and spatial patterns.

Chapter 6 presents the conclusions and perspectives of the thesis.

Additionally, the chapter structure of this thesis and relationships between these three specific research objectives have been illustrated in the Figure 1.1.

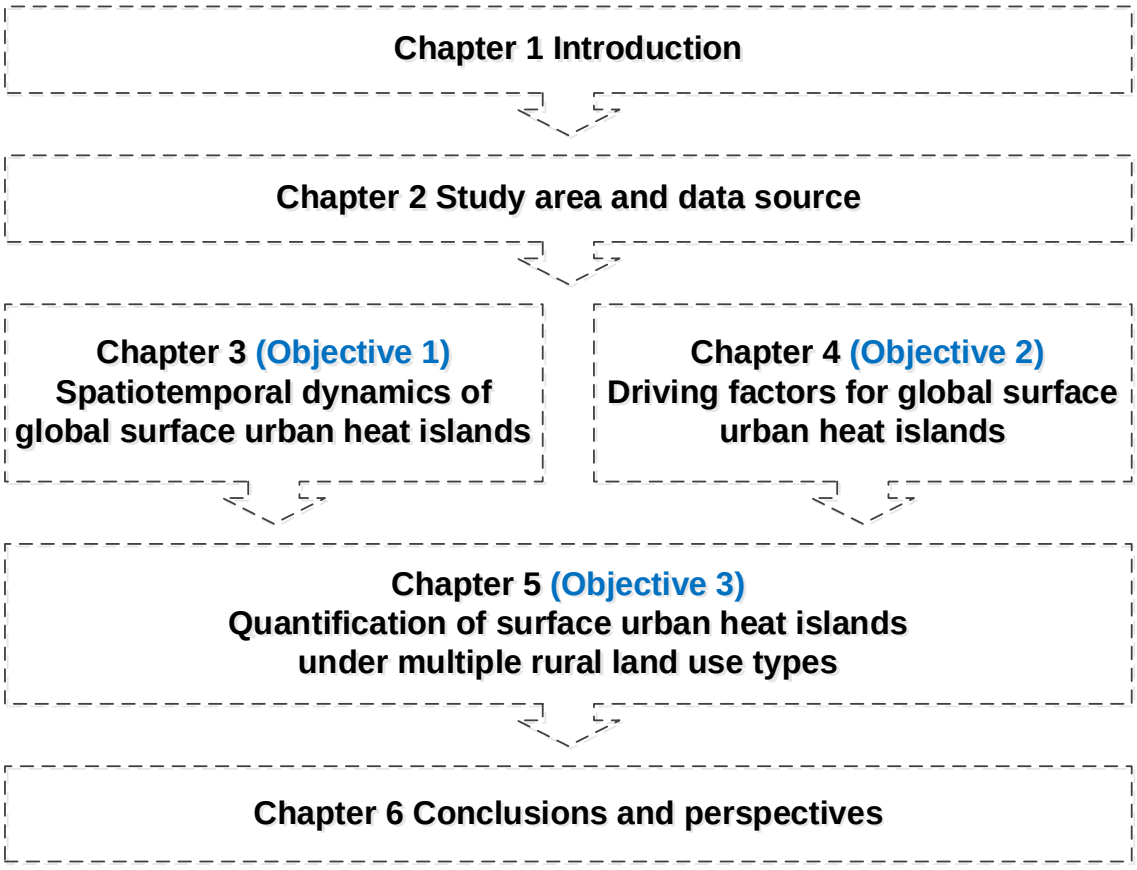

Figure 1.1 Illustration of the chapter structure of this thesis.

2 Study area and data source

In order to study the SUHI phenomenon in major cities around the world, it is necessary to make full use of the existing large-scale and long-term remote sensing and other auxiliary datasets. This chapter introduces the overview of the study area and the source of the involved data. The spatial distribution of the research target and the its population growth trends in the past decades was introduced, followed by the descriptions of the data sources, data usage, spatial and temporal resolution, and time range in detail.

2.1. Overview of the study area

In the study of global SUHI, large cities worldwide are selected as the research target based on its population size. According to the World Population Prospect (WUP) issued by the United Nations, there are 1,860 cities in the world with a population of more than 300,000 as of 2019. Between 1990 and 2018, the average annual population growth in these cities was 1.8%, and 60% of them were often exposed to natural disaster risks (United-Nations, 2019). The cities with a population of more than 300,000, which are undergoing rapid population growth and gradual environmental problems, are selected as the objects of this study. According to the urban population classification in 2019, the distribution of global cities at different levels is shown in Figure 2.1.

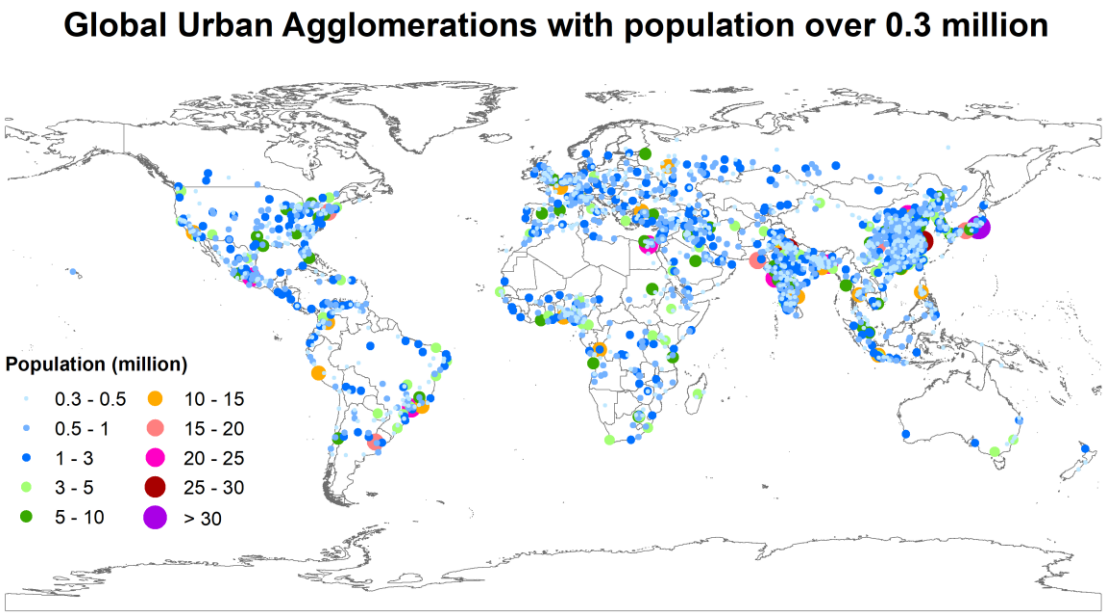

Figure 2.1 Global cities with population over 0.3 million by 2019.

As of 2019, the global population is about 7.63 billion, of which about 4.22 billion people (55%) live in cities. By 2050, the total global population prospects to reach 9.75 billion, and the urbanization rate of the world's population will increase to 68.4%. Figure 2.2 shows the trends and prospects of urban and rural populations at different levels of development in the world: 1) More developed regions comprise Europe, Northern America, Australia/New Zealand and Japan.; 2) Less developed regions comprise all regions of Africa, Asia (except Japan), Latin America and the Caribbean plus Melanesia, Micronesia

and Polynesia.; 3) The least developed countries include 47 countries defined by the United Nations: 33 in Africa, 9 in Asia, 4 in Oceania and one in Latin America and the Caribbean, with other less developed countries comprise the less developed regions excluding the least developed countries(United-Nations, 2019). It can be seen that from 1950 to 2050, the urban population in developed countries will increase from 0.45 billion to 1.11 billion, which is 2.48 times of the original; while the urban population in developing and underdeveloped countries will increase from 0.30 to 5.56 billion. It is estimated that the urban population will increase to 18.27 times of the original amount within a century.

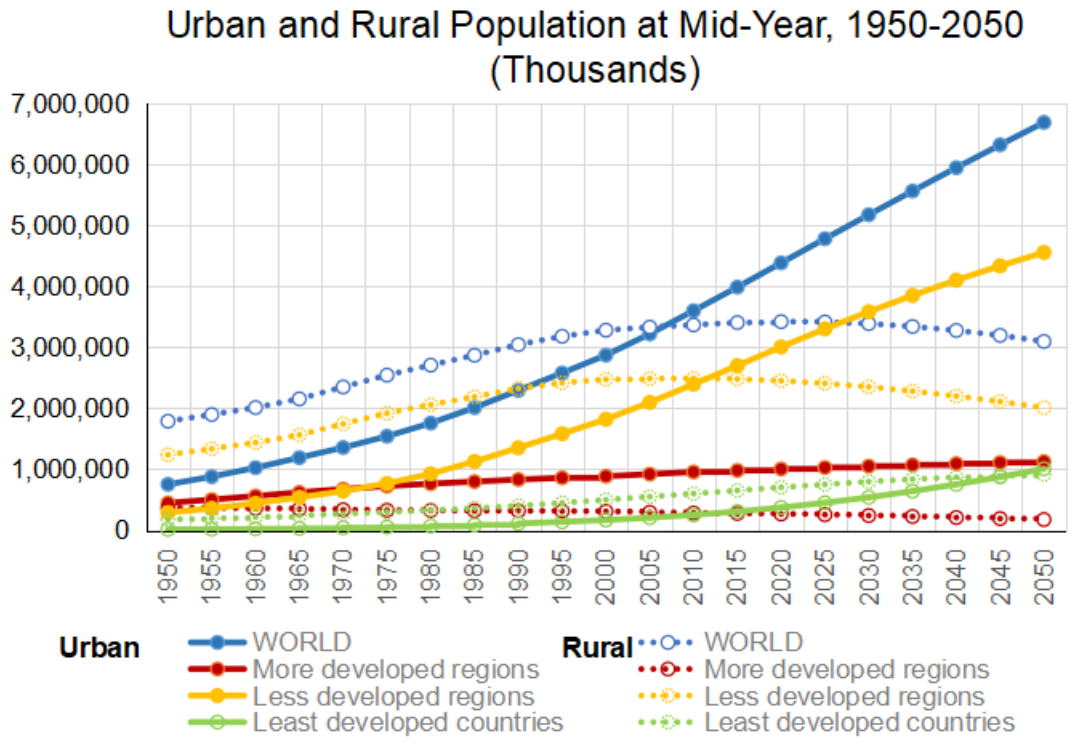

Figure 2.2 Urban and rural population around the world, and in developed, developing and less developed Countries, 1950-2050 (World Urbanization Prospect, 2019).

Since 2005, the proportion of the world's urban population has surpassed that of the rural population for the first time. The urban population of developing countries in particular has shown an exponential growth trend with increase rate far exceeded that of developed countries, taking the lead in the global urban population growth (Figure 2.3). It can be seen that since the beginning of the 21st century, the urbanization process has evolved into an unprecedented wave around the world. Therefore, this study selects global

cities or urban agglomerations as the research object for SUHI phenomenon.

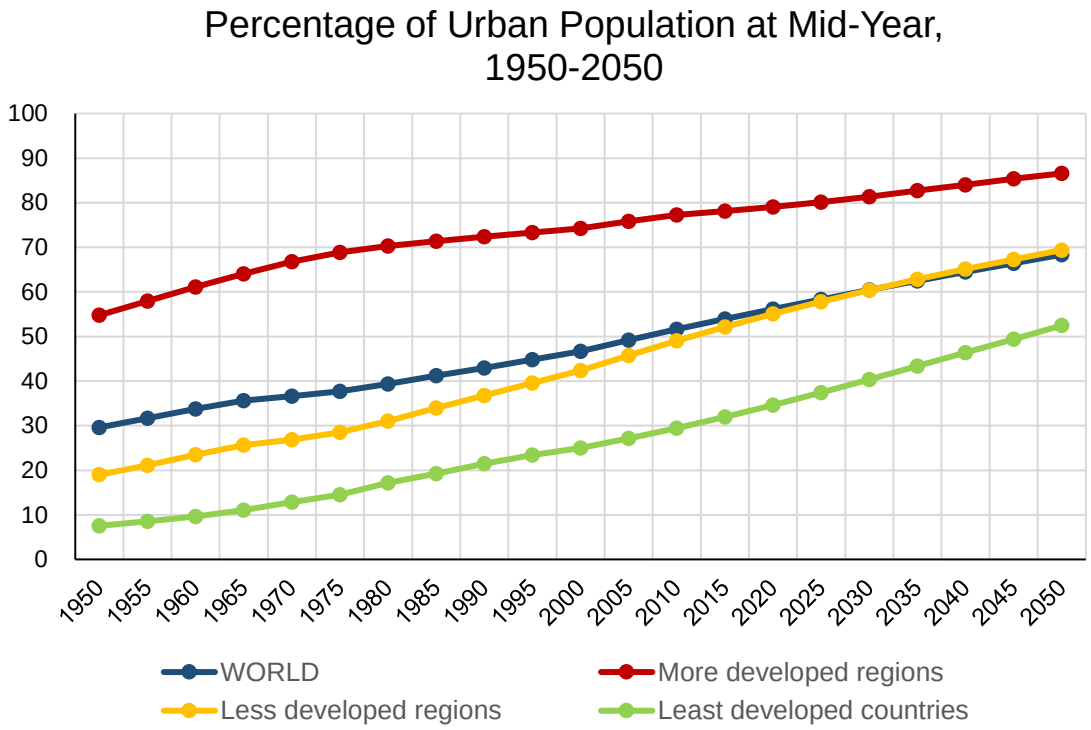

Figure 2.3 Proportion of urban population around the world, and in developed, developing and less developed Countries, 1950-2050 (World Urbanization Prospect, 2019).

2.2. Data source

The data sets involved in this study include urban population and geographic location data, Moderate Resolution Imaging Spectroradiometer (MODIS) data, global grid data sets of population and other data. The details are introduced as follows.

2.2.1. Population and Location

The population and geographic location data come from the latest WUP (2018 Revised Edition) released by the Population Division of the United Nations Department of Economic and Social Affairs (United-Nations, 2019). This data set provides estimation of the existing urban and rural populations and its prospects for the major urban agglomerations and all countries worldwide (https://population.un.org/wpp/Download/Standard/Population/). It has been widely used

throughout the United Nations and many international organizations, research centers, academic researchers and media.

2.2.2. MODIS Land surface temperature

The land surface temperature can be extracted from the LST product (MOD11A1 and MOD11A1, Version 6) onboard the Terra and the Aqua satellites, either of which is a daily surface temperature/emissivity product data set for each pixel with a spatial resolution of 1km and a sinusoidal projection. The transit time of the Terra and Aqua satellites are approximately 10:30 and 22:30 at local solar time, and 01:30 and 13:30 at local solar time, respectively. The time span of available datasets is from February 24, 2000 to present for MOD11A1, and from July 4, 2002 to present for MYD11A1. All the available global day/night LST data sets from January 1, 2003 to December 31, 2019 were selected for this study.

2.2.3. MODIS Land Cover Type

The annual land cover types are extracted from the MODIS land cover type product (MCD12Q1, Version 6), which provides the distribution of global land cover types at annual intervals. The product is obtained by supervising decision tree classification technology with MODIS Terra/Aqua reflectance data, with a spatial resolution of 500m and a time range from 2001 to 2019. Corresponding to the time range of the LST data set, the MCD12Q1 data from 2003 to 2019 were selected to obtain the land use and land cover (LULC) types.

The dataset includes five different land cover classification schemes, namely the International Geosphere-Biosphere Programme (IGBP), the University of Maryland (UMD), the MODIS-derived Leaf Area Index/ Photosynthetically Active Radiation of Vegetation Component scheme (Leaf Area Index legend, LAI/fPAR), and the MODIS-derived Net Primary Productivity Scheme (Annual BIOME-Biogeochemical Cycles, NPP/BGC) and Vegetation Functional Types Scheme (Annual Plant Functional Types,

PFT). In this study, the land cover types are divided into 17 categories using the IGBP classification scheme (Sulla-Menashe and Friedl, 2018) as detailed in Table 2.1:

Table 2.1 IGBP legend and classification for MCD12Q1

Value	Name	Description
1	Evergreen Needleleaf Forests	Dominated by evergreen conifer trees (canopy >2m). Tree cover >60%.
2	Evergreen Broadleaf Forests	Dominated by evergreen broadleaf and palmate trees (canopy >2m). Tree cover >60%.
3	Deciduous Needleleaf Forests	Dominated by deciduous needleleaf (larch) trees (canopy >2m). Tree cover >60%.
4	Deciduous Broadleaf Forests	Dominated by deciduous broadleaf trees (canopy >2m). Tree cover >60%.
5	Mixed Forests	Dominated by neither deciduous nor evergreen (40-60% of each) tree type (canopy >2m). Tree cover >60%.
6	Closed Shrublands	Dominated by woody perennials (1-2m height) >60% cover.
7	Open Shrublands	Dominated by woody perennials (1-2m height) 10-60% cover.
8	Woody Savannas	Tree cover 30-60% (canopy >2m).
9	Savannas	Tree cover 10-30% (canopy >2m).
10	Grasslands	Dominated by herbaceous annuals (<2m).
11	Permanent Wetlands	Permanently inundated lands with 30-60% water cover and >10% vegetated cover.
12	Croplands	At least 60% of area is cultivated cropland.
13	Urban and Built-up Lands	At least 30% impervious surface area including building materials, asphalt, and vehicles.
14	Cropland/Natural Vegetation Mosaics	Mosaics of small-scale cultivation 40-60% with natural tree, shrub, or herbaceous vegetation.
15	Permanent Snow and Ice	At least 60% of area is covered by snow and ice for at least 10 months of the year.
16	Barren	At least 60% of area is non-vegetated barren (sand, rock, soil) areas with less than 10% vegetation.
17	Water Bodies	At least 60% of area is covered by permanent water bodies.

2.2.4. MODIS Vegetation indices

The vegetation index is extracted from the vegetation index product (MOD13A2 and

MYD13A2, Version 6) onboard the Terra and the Aqua satellites with a spatial resolution of 1km. The data set contains two vegetation indices: the Normalized Difference Vegetation Index (NDVI) and the Enhanced Vegetation Index (EVI). The algorithm of this product is based on the criteria of low cloud cover, low observation angle and high NDVI/EVI, and selects the best available pixel value from all samples in the adjacent 16-day period. The EVI index is selected in this study as it can better reflect the canopy structure of vegetation than NDVI(Peng et al., 2012). The time span of available datasets is from February 24, 2000 to present for MOD13A2, and from July 4, 2002 to present for MYD13A2. All the available global EVI data sets from January 1, 2003 to December 31, 2019 were selected for this study.

2.2.5. MODIS Albedo

The surface albedo is extracted from the MCD43A3 (Version 6) data set. The daily image is generated using 16 days of data (centered on a given date) with a spatial resolution of 500m. This product provides directional hemispherical reflectance (black-sky albedo) and double hemispherical reflectance (white-sky albedo) for each MODIS reflection band (band 1 to band 7) and 3 broad spectrum bands (visible light, near-infrared and shortwave). The white sky albedo (WSA) is selected in this study as it is linearly related to the white sky albedo, and demonstrates similar impact on SUHI (Peng et al., 2012). The time span of available datasets is from February 18, 2000 to present. All the available global WSA data sets from January 1, 2003 to December 31, 2019 were selected for this study.

2.2.6. Elevation

The surface elevation is extracted from the GTOPO30 dataset with a spatial resolution of 1km from the US Geological Survey (USGS). The center point for the digital elevation model (DEM) is given every 30 seconds of latitude and longitude worldwide. The latitude and longitude grid composed of these discrete points divides the earth's surface into many quadrilateral grid areas, so that the elevation value of any point in the grid area can be

obtained by interpolation from the surrounding four grid points.

2.2.7. Climate

The meteorological elements are extracted from the monthly climate and climatic water balance datasets for global terrestrial surfaces - TerraClimate with a spatial resolution of 2.5 arc minutes (~ 5 km). The climate-assisted interpolation was employed by combining the high spatial resolution climate standard of the WorldClim data set with the coarser spatial resolution but time-varying CRU Ts4.0 and the Japan 55-year reanalysis (JRA55) data set. The TerraClimate data set contains the monthly average precipitation, wind speed, surface solar radiation, maximum and minimum temperature, water vapor pressure and other elements on the global land surface. The time span of available datasets is from 1958 to present (Abatzoglou et al., 2018). The monthly averaged precipitation and wind speed data sets from January 2003 to December 2019 was selected for this study.

2.2.8. Population Density

The population density comes from the Gridded Population of the World (GPW, v4.11) population grid density estimation data set, which uses the population proportions of the census and administrative units to allocate the population to each grid. The global population in the year 2000, 2005, 2010, 2015 and 2020 are simulated with a spatial resolution of 30 arc seconds (~ 1 km). The data set contains estimates of the population per square kilometer with one global image for each modeling year. In this study, five images from 2000 to 2020 are selected. For the years with missing data between 2003 and 2019, the annual global population density can be constructed by borrowing the data set of its neighboring years.

2.2.9. Others

The vector map of global administrative divisions at all levels from GADM (https://gadm.org/data.html), and administrative divisions of China from the Resource and

Environmental Science Data Center of the Chinese Academy of Sciences (https://www.resdc.cn/data.aspx?DATAID=201) were also employed. In addition, the division of Köppen climate zone is from a vector format map (http://koeppen-geiger.vu-wien.ac.at/shifts.htm).

2.2.10. Summary

In general, the historical population data and the global administrative division data of global major cities are all openly accessible from the Internet. Global-scale remote sensing data, such as MODIS LST, WSA, EVI and land use data, meteorological data, population grid data, etc., can be obtained freely and directly on the Google Earth Engine (GEE) platform with online processing. In addition, the GEE platform also supports the import of external data. Local data can be uploaded online and employed in conjunction with the existing data on the platform. Table 2.2 lists a summary of the data used in this study.

2.3. Conclusions

This chapter first provides an overview of the selected study area, the spatial distribution of the target cities and its population variations. The global scale long-term remote sensing data sets are described in detail. As the most widely used satellite data, MODIS can provide long-term products and reliable data acquisition methods, which is basically the core data source of this research. In addition, open and accessible urban population and geographic data, global grid meteorological data sets, and global grid population density data provide the feasibility for the implementation of this study. The data preparation in this chapter provides sufficient guarantee for subsequent research on the spatiotemporal pattern of SUHI and its driving factors.

Table 2.2 Data source and description

Data usage		Data source	Spatiotemporal resolution	Description	Time
Study area		WUP	-	Urban Population	2019
		GADM	-	Urban Center	-
			-	Administrative Boundary	-
Spatiotemporal SUHI		MOD11A1/ MYD11A1	1 km, day/night	Instantaneous LST	2003 - 2019
		MCD12Q1	500 m, yearly	LULC	
Drivers	Surface Property	MOD13A2/ MYD13A2	1 km, 16 - day	EVI	2003 - 2019
		MCD43A3	500 m, daily	WSA	
		GTOPO30	1 km	DEM	-
	Climate	TerraClimate	2.5 ″, monthly accumulation	Precipitation	2003 - 2019
			2.5 ″, monthly average	Wind Speed	
	Urbanization	GPW	30 ″， 5-year	Population Density	2003 - 2019
		MCD12Q1	500 m, yearly	Urban Size	

3 Spatiotemporal dynamics of global surface urban heat islands

This chapter mainly conducts the research on the spatiotemporal dynamics of global SUHIs in major cities from 2003 to 2019. First, an improved dynamic urban-extent scheme is used to identify the yearly urban region and the corresponding rural area from 2003 to 2019. Subsequently, based on the global daily (day/night) LST data set from 2003 to 2019, the urban-rural temperature difference method was used to calculate the global SUHII. The spatiotemporal pattern of SUHIIs at the global scale, across the climatic zones, and along the latitudinal variations are displayed. The monthly variation and day-night cycle of SUHIIs are also explored by major climate zones. Finally, the interannual trends of global and regional SUHIIs are revealed on the annual average, summer average, and winter average scales.

3.1. Introduction

Urban expansion and its associated anthropogenic activities regularly influence the ground surface properties and urban climate conditions, thereby disturbing the surface energy balance (Grimm et al., 2008b). Consequently, the phenomenon of UHI, in which urban regions are warmer than their neighboring hinterlands, occurs in most global cities and urban clusters and can threaten the sustainable development of mankind. Therefore, scientific characterization of the global UHI patterns and its long-term variation is urgently required (Oke, 1982; Bai et al., 2018).

Conventionally, the UHI effect has been quantified using air temperature records acquired from ground observations across urban zones and their vicinities, a phenomenon known as canopy UHI (Arnfield, 2003; Hu et al., 2019). Remote sensing technology can overcome the limitations of the ground observations, by providing sufficient LST data with large spatial coverage, thus, encouraging the study of the SUHI through new perspectives (Jin, 2012). Up to present, multiple studies on the spatiotemporal patterns, driving mechanisms, and mitigation strategies of SUHI, ranging from local, national, and regional to global scales, have been reported based on satellite data (Quan et al., 2014; Zhou et al., 2014a; Peng et al., 2018b; Yu et al., 2019; Zhou et al., 2013; Peng et al., 2012; Clinton and Gong, 2013; Lai et al., 2021). However, the global long-term SUHI patterns and its variations have rarely been fully detected at multiple scales (Zhou et al., 2019; Li et al., 2020c; Simwanda et al., 2019; Wu and Ren, 2019).

The quantification methods for SUHII by using either LULC or LST patterns were most popular in current SUHI studies. Other than the massive computation process in LST pattern methods (Zhou et al., 2016c; Rajasekar and Weng, 2009), the LST difference method based on the LULC were generally employed; that is, the rural LST was subtracted from urban LST to indicate the SUHII (Zhou et al., 2015; Santamouris, 2015; Yao et al., 2018b; Yao et al., 2017; Chakraborty et al., 2020). After identifying the urban clusters and rural regions based on LULC, the SUHII is readily calculated (Peng et al., 2012; Clinton and Gong, 2013; Zhou et al., 2014a). The MODIS sensors observe the ground surface

nearly four times in a day and have been recording data regularly for over 20 years. It can not only provide global LST data with a spatial resolution of 1 km (Li et al., 2013), but also is able to observe atmospheric and surface properties concomitantly, making it the most suitable data source for comprehensive research on the SUHI patterns and its driving mechanisms (Li et al., 2018). Nowadays, with the global long-term thermal infrared remote sensing LST data, it is convenient and feasible to provides reliable results for spatiotemporal studies of the SUHI at multiple scales (Zhou et al., 2014b; Clinton and Gong, 2013; Pede and Mountrakis, 2018; Weng et al., 2004; Weng et al., 2019; Fu and Weng, 2018). However, the identification scheme of urban extent in current global SUHII studies is inconsistent, and generally ignored the fact of urban sprawl by employing relatively obsolete urban extent, which is certainly deem to affect the estimation of SUHII (Yao et al., 2018a).

For an instance, SUHI for more than 3000 global settlements was first characterized using MODIS LST data averaged over a short period from 2003 to 2005 with impervious surface product in 2001 to identify individual urban areas (Zhang et al., 2010), followed by the SUHI study on 419 global large cities using the MODIS Aqua LST dataset over 2003–2008 after defining the urban clusters with land cover datasets (Peng et al., 2012), and the SUHI study on global cities between 55 °S–71 °N (defined by a global urban extent datasets) in 2010 with the MODIS Terra/Aqua LST data by a comparison of 5 km and 10 km buffers as the rural region (Clinton and Gong, 2013). These limited global studies did not completely analyze the long-term evolution of land use changes or the global SUHI patterns. To better understand the global SUHI dynamics, further investigations on the land use change using satellite data and an increased time range are required. In a most recent study, 15 years of the MODIS LST data prior to 2017 were used to detect the global SUHII by differentiating the continuous urban regions from rural pixels enclosed in fixed urban boundaries (Chakraborty and Lee, 2019). With the urban expansion in later years, some urban pixels transcend the urban extents, leading to a reduction of urban data and imprecise results in quantifying SUHI. To accurately identify the dynamic urban and rural regions for

populous cities, urban targets should not be restricted to fixed urban boundaries. Moreover, the rural pixels close to the urban cluster will overestimate the rural background LST, as a consequence need to be purified. Given this, the quantification methodology of urban extent is necessary in updating to improve the rigor and credibility of the global SUHI research.

To this end, this chapter aims to investigate the spatiotemporal characteristics of long-term global SUHI during 2003 and 2019 over major large cities, where the urban clusters and their rural regions for these major global cities were detected each year by an improved DUE scheme.

3.2. Methodology

3.2.1. Dynamic urban-extent (DUE) method

Urban and rural regions were initially recognized to mask the LST datasets prior to calculating the SUHII. To capture the dynamic urban extents across years, the urban and rural regions were defined year-by-year, which we call the DUE scheme. Firstly, the city clustering algorithms (CCA) was employed, which have been widely introduced to identify urban clusters for large-scale SUHI studies (Rozenfeld et al., 2008). Based on the interconnection of urban regions, an iterative search was executed to identify the urban clusters with MATLAB. The longitudes and latitudes of each urban center were selected as initial points to activate the CCA (Peng et al., 2012; Peng et al., 2018b). In total, 1711 global cities with total population above 0.3 million in 2019 were predefined, and the urban clusters during 2003–2019 were annually identified for each city. Secondly, the rural areas were annually defined as the equiareal buffer zone around each urban cluster. Considering the interaction between the urban centers and their suburbs, the first buffer ring was an urban fringe, which was excluded to acquire a relatively pure rural region (Peng et al., 2018b). Finally, water body pixels were eliminated because of their high specific heat capacity, which could overestimate SUHII at daytime and underestimate SUHII at nighttime. Additionally, discrete urban pixels enclosed in rural regions were excluded. Furthermore, since elevation differences between urban and rural pixels also influence

SUHII, rural pixels with an elevation difference of 200 m from the mean urban elevation were excluded. The comparison of urban and rural regions identified by DUE and SUE schemes (Chakraborty and Lee, 2019) are illustrated in Figure 3.1. With the obsolete landcover information, both the urban and rural regions defined by SUE is incomplete in contrast with the latest urban extent in 2019 by DUE.

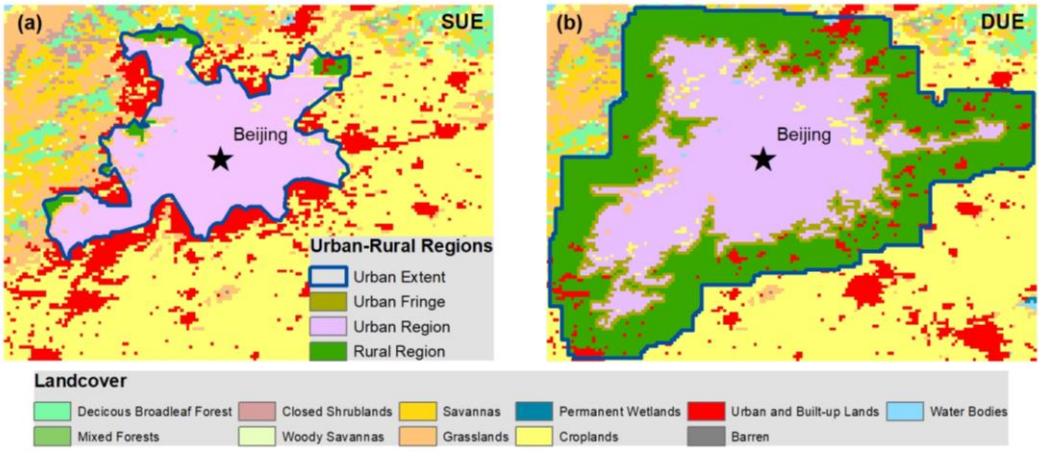

Figure 3.1 Comparison of urban and rural regions identified by (a) SUE and (b) DUE methods with background landcover in Beijing, 2019.

3.2.2. Quantification of SUHI at multiple scales

The yearly dynamic urban and rural regions during 2003-2019 were uploaded to the GEE platform, and the SUHII was calculated as the mean LST difference between the urban and rural regions with the MODIS datasets in GEE. The daily SUHIIs for a single city at four time points t were calculated using Equation (3.1):

$$SUHII_t = T_{t\_urban} - T_{t\_rural} \tag{3.1}$$

here, the subscript t represents the four time points when Terra transits at 10:30 and 22:30, and Aqua transits at 13:30 and 01:30, respectively. T_{t_urban} and T_{t_rural} are the mean LSTs for the urban and rural regions. Later, the daytime and nighttime SUHIIs from MOD and MYD were averaged, respectively, for each urban cluster using Equations (3.2)–(3.3):

$$SUHII_D = \frac{SUHII_{day1030} + SUHII_{day1330}}{2} \tag{3.2}$$

$$SUHII_N = \frac{SUHII_{night2230} + SUHII_{night0130}}{2} \quad (3.3)$$

Here, $SUHII_D$ and $SUHII_N$ are the integrated daytime and nighttime SUHIIs, respectively. The subscripts $day1030$, $night2230$, $day1330$, and $night0130$ denote the timepoints when Terra or Aqua transits. Thereafter, $SUHII_D$ and $SUHII_N$ were averaged for the daytime and nighttime SUHIIs at annual ($SUHII_{AD}$ and $SUHII_{AN}$), summer ($SUHII_{SD}$ and $SUHII_{SN}$) and winter ($SUHII_{WD}$ and $SUHII_{WN}$) scales for each city. The summer months of June, July, and August and the winter months of December, January, and February for the Northern Hemisphere are opposite to that for the Southern Hemisphere. The workflow used to calculate the daily SUHIIs by DUE is shown in Figure 3.2.

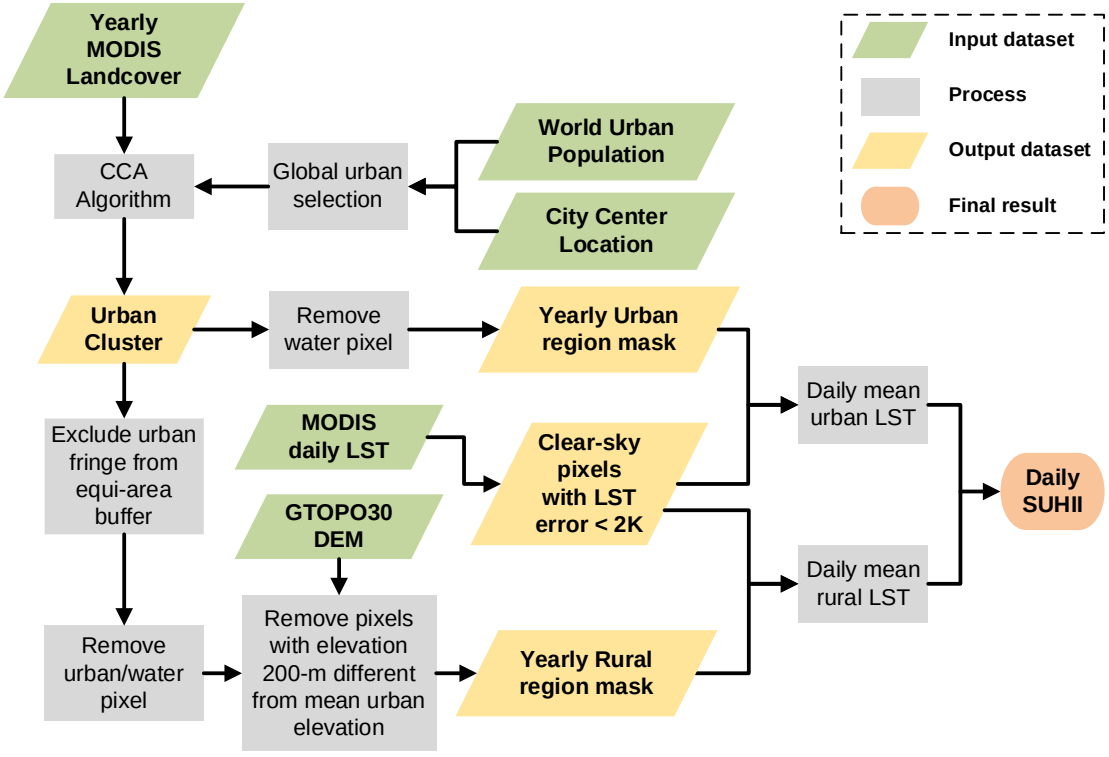

Figure 3.2 Workflow to calculate the daily SUHII. The green parallelograms represent input dataset, the gray rectangles denote processing procedure, the yellow parallelograms are output dataset, and the ellipse is the final result.

3.2.3. Regional and latitudinal variation

Since background climate conditions are a driving force for global SUHI patterns, a partition scheme based on climate conditions was employed to analyze the zonal characteristics of global SUHII. Global region was categorized into five major climate zones, including equatorial, arid, warm temperate, snow, and polar zones referring to the Köppen-Geiger climate classification scheme (Rubel and Kottek, 2010) (Figure 3.3). Subsequent regrouping of the urban clusters according to these categories resulted in 430, 280, 806, 188, and 2 urban clusters in the equatorial, arid, warm temperate, snow, and polar zones, respectively. The polar zone containing only two urban clusters was excluded and only the first four climate zones were adopted. In addition, five urban clusters not enclosed in any climate zone were excluded from the following analysis. Subsequently, the regional SUHIIs were spatially averaged at the annual, summer, and winter scales. Finally, the spatial pattern and interannual trends of the regional SUHIIs were analyzed.

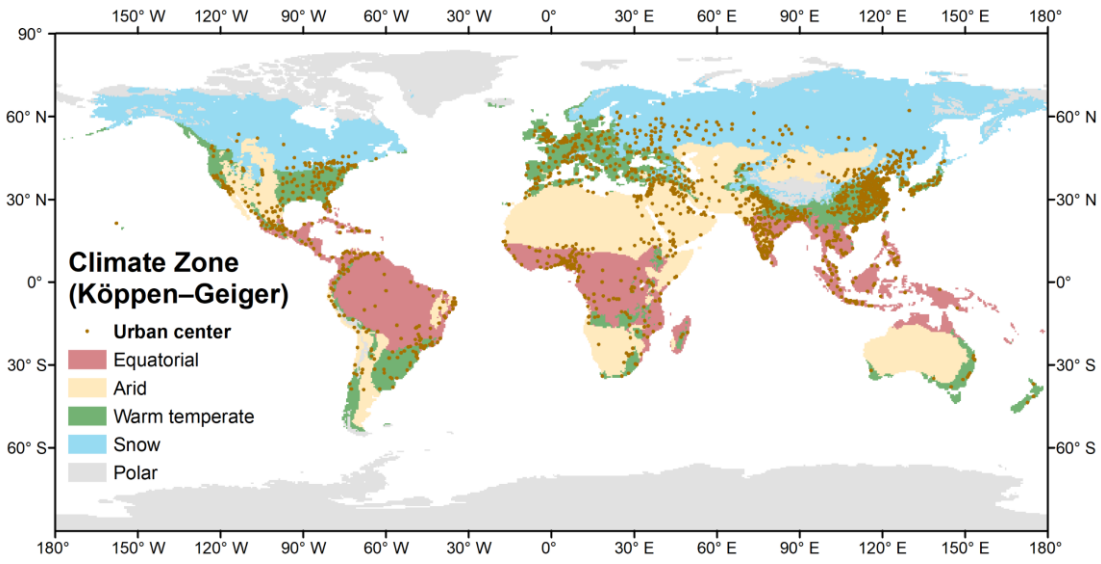

Figure 3.3 Spatial distribution of 1711 global urban clusters with population over 0.3 with the background climate zones.

Considering the effect of solar radiation on SUHI along different latitude zones, the global urban regions were divided latitudinally into 5° intervals to investigate the regional SUHII variations (Chakraborty and Lee, 2019). The city centers of the 1711 global urban

clusters were used to determine their latitudinal zone locations. Subsequently, the global SUHIIs were spatially averaged across the latitudinal division at the annual, summer, and winter scales.

3.2.4. Interannual trend

The Mann-Kendal (MK) test was used to detect whether interannual trends exist for each urban cluster. Later, slope (Sen's slope) was calculated using the Theil-Sen estimator. Compared with the conventional parametric tests for assessing the trends, the MK test does not require normally distributed data and is more suitable for small sample sizes (Fernandes and G. Leblanc, 2005). Sen's slope was used to compute the linear rate of change using the median of the slopes of all the lines through pairs of points in a particular time series. It is not sensitive to outliers and more robust than the least squares method; thus, it is applicable in univariate time series (Mondal et al., 2015). These non-parametric tests have been widely used to study the trends of environmental changes (Hamed, 2008; Thompson and Paull, 2017; Planque et al., 2017). Finally, the interannual trends of SUHIIs at multiple spatiotemporal scales were determined by the MK test ($p<0.05$) for four levels: significant increase, insignificant increase, significant decrease, and insignificant decrease. Later, the rate of change was calculated using Sen's slope at the annual, summer, and winter averaged scales.

3.3. Results

3.3.1. Spatiotemporal pattern of global SUHI

3.3.1.1. Global pattern

Figure 3.4 shows the spatial distribution of $SUHII_{AD}$ and $SUHII_{AN}$ averaged over 2003–2019 for each city. Globally, the average $SUHII_{AD}$ varied between -4.9 and +4.7 °C, while the average $SUHII_{AN}$ varied between -0.9 and +2.9 °C. Negative SUHIIs (i.e., cold

islands) were observed frequently during the daytime, particularly in northern Africa, the Middle East, and parts of western India, where the urban clusters were generally enclosed by a desert terrain. The urban LST in these regions is generally affected by evapotranspiration cooling of surface vegetation at daytime (Mohajerani et al., 2017) The vegetation activities weaken at nighttime, while the thermal storage at daytime and anthropogenic heat flux cause a positive nighttime SUHII. The findings were consistent with the global SUHII findings of other studies (Peng et al., 2012; Chakraborty and Lee, 2019).

The averaged summer $SUHII_{SD}$ and $SUHII_{SN}$ during 2003–2019 for each city varied from -5.5 to +5.9 °C and from -1.8 to +3.3 °C, respectively (Figure 3.5). The summer daytime SUHII was higher than that of nighttime; however, the spatial trends were similar to that of the annual daytime SUHII. The winter averaged $SUHII_{WD}$ ranged between -4.5 and +4.5 °C, which was lower than that of averaged $SUHII_{WN}$ ranging between - 0.8 and +3.8 °C (Figure 3.6). Compared with the summer SUHIIs, the averaged $SUHII_{WD}$ and $SUHII_{WN}$ were generally weaker; additionally, a negative $SUHII_{WD}$ was observed in north China, with arid and semi-arid cities distributed in the northwest region and frequent heavy air pollution events observed in the northeast region due to cold winters.

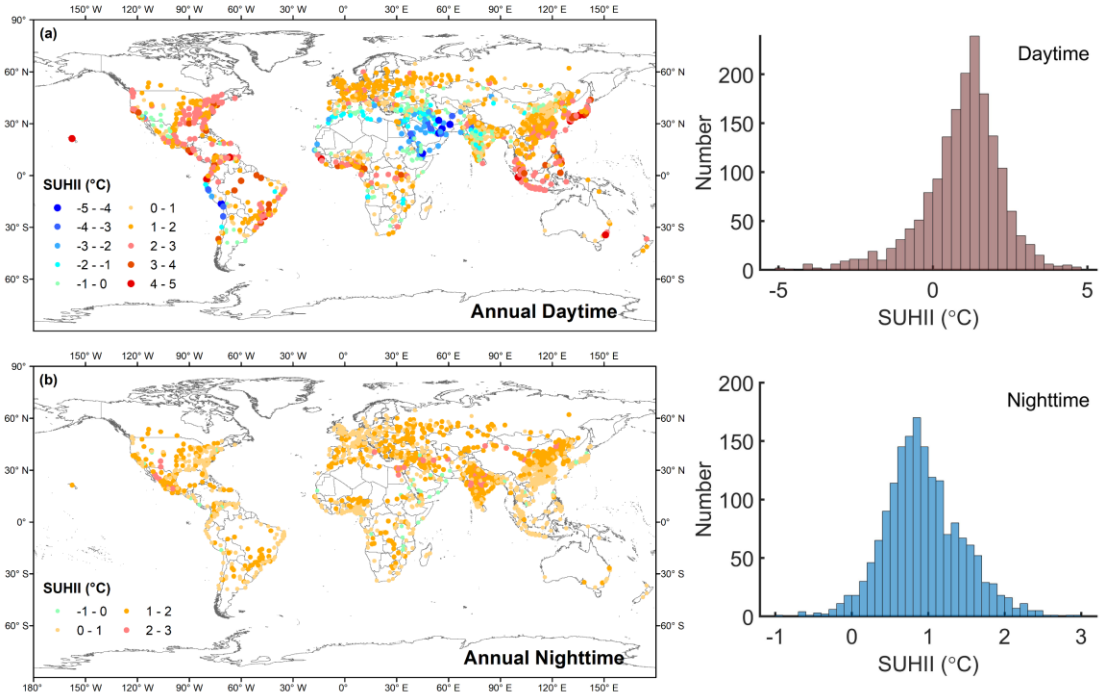

Figure 3.4 Spatial distribution of 1711 SUHIIs averaged over 2003–2019 for annual (a) daytime ($SUHII_{AD}$) and (b) nighttime ($SUHII_{AN}$).

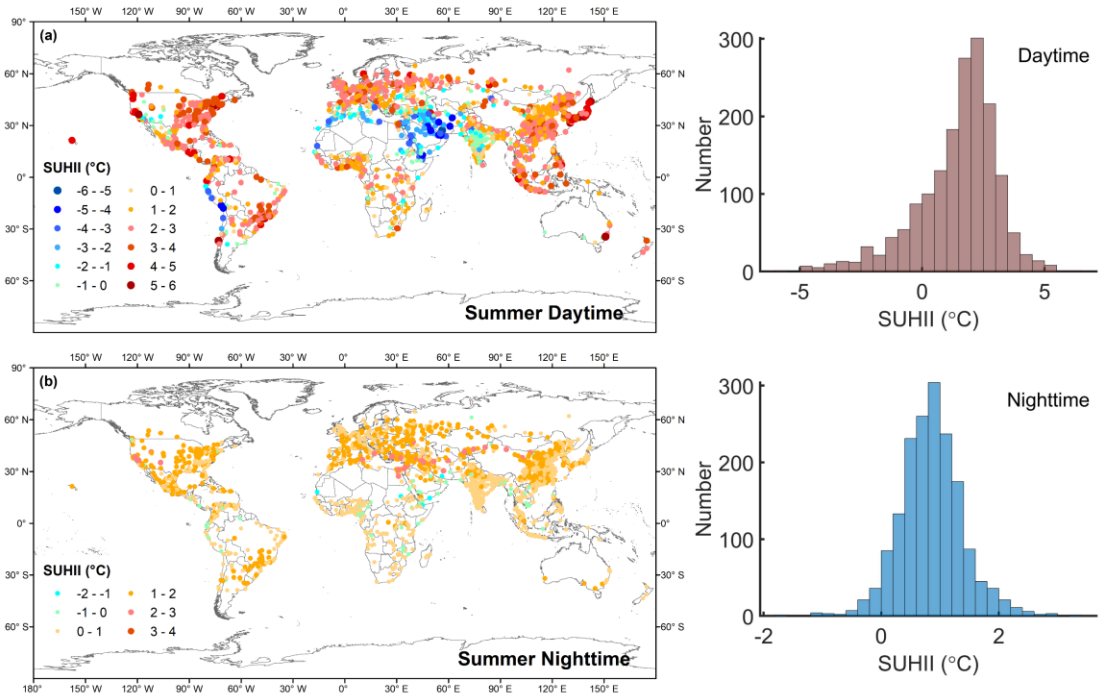

Figure 3.5 Same as Figure 3.4, but for summer (a) daytime ($SUHII_{SD}$) and (b) nighttime ($SUHII_{SN}$).

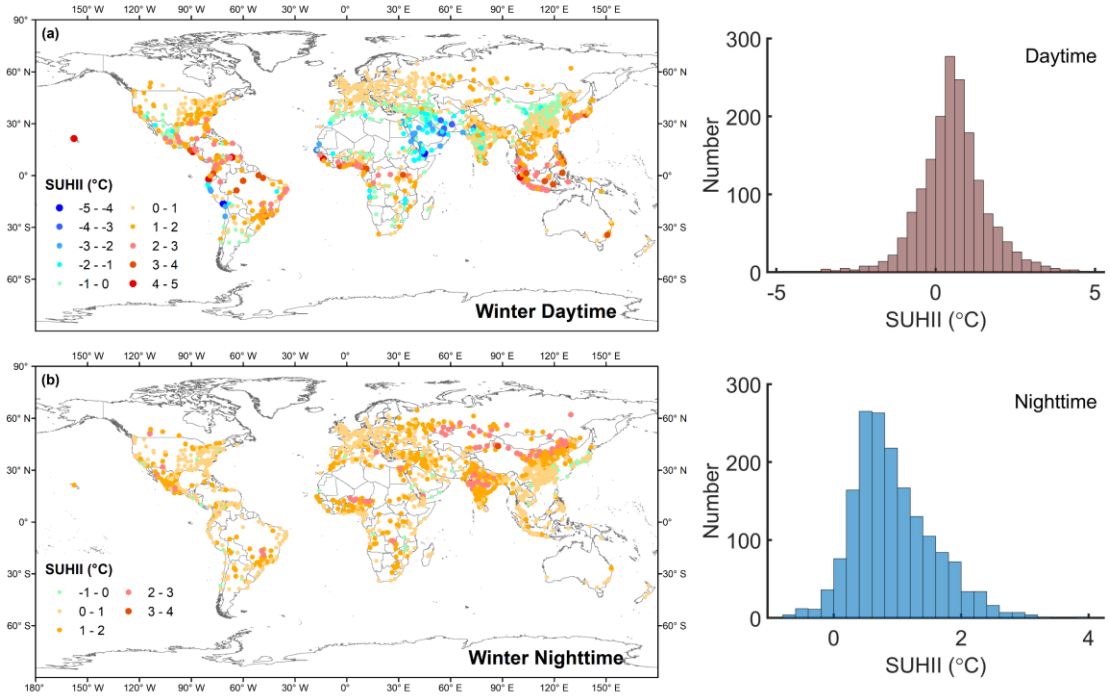

Figure 3.6 Same as Figure 3.4, but for winter (a) daytime ($SUHII_{WD}$) and (b) nighttime ($SUHII_{WN}$).

Table 3.1 and Figure 3.7 provide a summary of the global statistics of temporally averaged SUHIIs during 2003–2019 for each city at the annual, summer, and winter scales. The results from MODIS Aqua, which has been defined in Equations (3) and (4), indicated a higher SUHII at daytime than those from MODIS Terra defined in Equations (1) and (2); conversely, the opposite scenario was observed at nighttime. This was consistent with the fact that MYD LST products at two transit times correspond to the daily minimum and maximum values (Wan, 2008). According to the combined Terra and Aqua results defined in Equations (5) and (6), the global mean values of temporally averaged annual daytime SUHII ($SUHII_D$) and nighttime SUHII ($SUHII_N$) were 0.97 °C and 0.94 °C, respectively. However, $SUHII_{AD}$ for the global 1711 cities was more dispersed, with a standard deviation of 1.27 °C, than that of $SUHII_{AN}$ with a standard deviation of 0.50 °C. The global mean value of temporally averaged $SUHII_{SD}$ and $SUHII_{SN}$ were 1.47 °C and 0.86 °C, respectively, and 0.54 °C and 0.93 °C for $SUHII_{WD}$ and $SUHII_{WN}$, respectively, with a higher standard deviation at daytime for both winter and summer.

Table 3.1 Summary of global mean values and their standard deviations of temporally averaged SUHII over 2003–2019 from MODIS Terra and Aqua

SUHII (°C)	Terra		Aqua		Terra+Aqua	
	Daytime (1030)	Nighttime (2230)	Daytime (1330)	Nighttime (0130)	Daytime	Nighttime
Annual	0.88 ± 1.24	1.01 ± 0.52	1.11 ± 1.38	0.93 ± 0.52	0.97 ± 1.27	0.94 ± 0.50
Summer	1.35 ± 1.60	0.93 ± 0.55	1.62 ± 1.76	0.83 ± 0.55	1.47 ± 1.64	0.86 ± 0.53
Winter	0.47 ± 0.99	0.99 ± 0.64	0.65 ± 1.19	0.93 ± 0.65	0.54 ± 1.05	0.93 ± 0.63

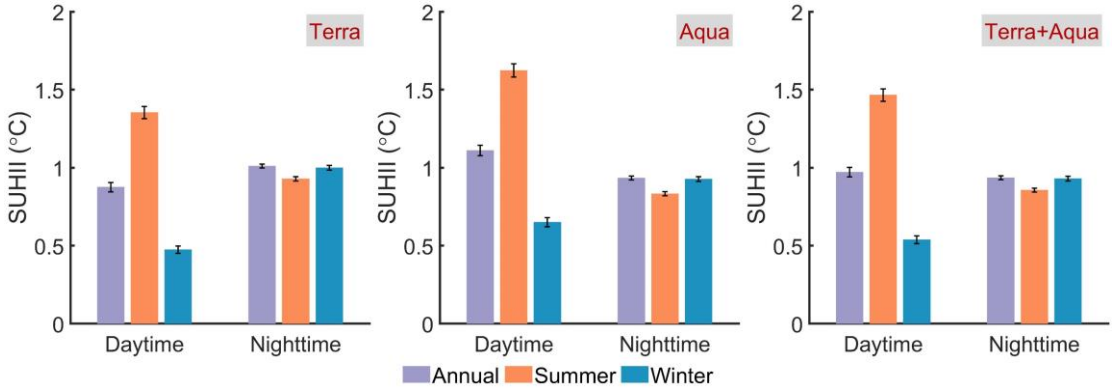

Figure 3.7 Summary of global mean values and standard errors of the temporally averaged SUHIIs for each city. The color bars represent mean values of 1711 temporally averaged SUHIIs. The error bars denote the standard errors of mean values.

Globally, high proportion of urban clusters exhibited a positive $SUHII_{AD}$ (82%, n=1410) than a negative $SUHII_{AD}$ (18%, n=301). At nighttime, the positive $SUHII_{AN}$ increased to 97% (n=1667), while the negative $SUHII_{AN}$ accounted for only 3% (n=44). Based on the SUHII dispersion and the sum of the positive and negative values, the global mean value of temporally averaged SUHII for each city reflected the day-night differences and seasonal variations only to some extent. Figure 3.8 displays the global distribution of the temporally averaged positive and negative SUHIIs at different temporal scales. At daytime, the global mean values of temporally averaged positive and negative SUHIIs were more evident in summer than in winter; conversely, these values did not evidently represent

seasonal fluctuations at nighttime. Comparatively, apart from the positive SUHII in winter, the global mean positive or negative SUHIIs at daytime were more distinct than that at nighttime. Generally, variation from daytime to nighttime was more evident in summer than in winter, while seasonality from summer to winter was more evident at daytime than at nighttime.

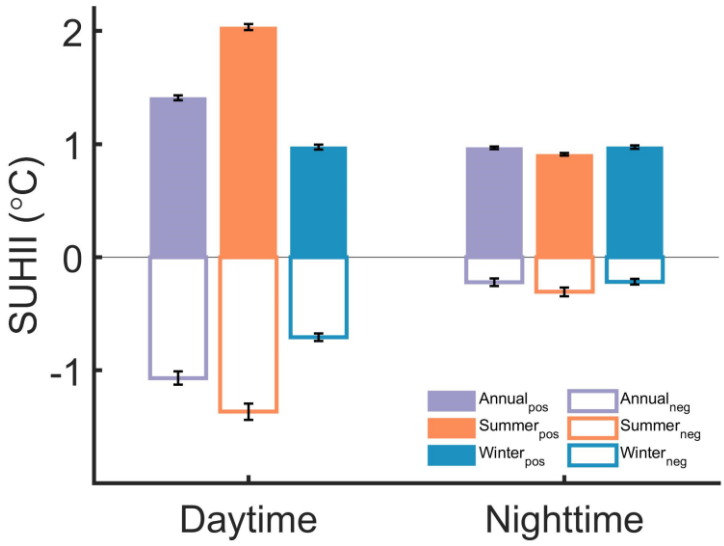

Figure 3.8 Global statistics of temporally averaged positive and negative SUHIIs for 1711 global urban clusters at different temporal scales. The color bars represent the global mean values of temporally averaged SUHIIs during 2003–2019 for each city. The error bars denote the standard errors of mean values. The solid and hollow bars represent positive and negative SUHIIs, respectively.

3.3.1.2. Climatic variation

Figure 3.9 displays the regional statistics of the global SUHIIs with respect to the four major climate zones (equatorial, arid, warm temperate and snow) accompanied with the global average. Annually, the equatorial zone demonstrated the most evident daytime SUHII, followed by the warm temperate and snow zones, and arid zones with negative values. At nighttime, higher SUHIIs were presented by the snow and arid zones, followed by the warm temperate and equatorial zones. In summer, both of the strongest daytime and nighttime SUHIIs occurred in the snow zone, which was in the equatorial and snow zones in winter.

Overall, the daytime SUHII was positive in all climate zones except the arid zone, which generally turned to positive at nighttime. Nevertheless, both the daytime and nighttime SUHII in arid zone demonstrated positive value in previous studies (Chakraborty and Lee, 2019). The daytime SUHII was higher than the nighttime SUHII except the arid zone in summer, while the winter daytime SUHII was lower than nighttime SUHII other than the equatorial zone. The seasonal variations from summer to winter were relatively higher in the snow and warm temperate zones at daytime, and in the equatorial zones at nighttime. The day-night variation of SUHII in the arid zone was evidently observed with a transition from negative (daytime) to positive SUHII (nighttime), especially in winter. However, this trend was more distinct in summer than in winter in the other zones.

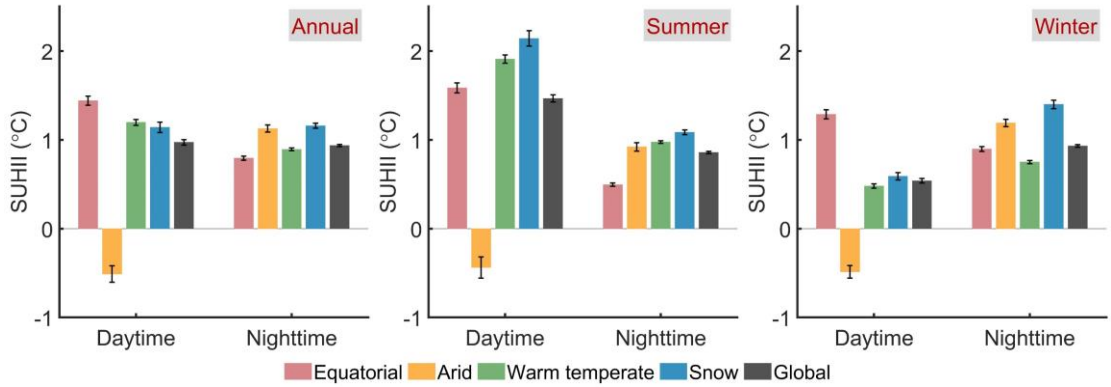

Figure 3.9 Global SUHII across different climate zones. The color columns denote the mean values, while the error bars denote its standard errors.

3.3.1.3. Latitudinal variation

The selected 1711 global urban clusters were distributed between 65 °N–45 °S and 160 °W–175 °E. These regions were further divided into latitudinal belts at an interval of 5 °. Figure 3.10 presents the variations of the global SUHII across each latitudinal belt. At the annual scale, the SUHI variations across the latitudinal belts were more evident at daytime. The daytime SUHII peaks were distributed at approximately 55 °N, 20 °S, 40 °S, and the equator, and they were higher than the nighttime SUHIIs between 15 °N–10 °S, north of 50 °N, and south of 20 °S. The day-night contrast was reversed (flip-flop) beyond these regions, which were mainly distributed in the arid and semi-arid cities. These results

are consistent with previous findings(Chakraborty and Lee, 2019) except for an extra flip-flop zone between 10 °S and 20 °S.

In summer, both the daytime and nighttime variations fluctuated more significantly than in winter, while no diurnal reversal was observed along the latitudinal belts. Moreover, the daytime SUHII increased sharply north of 35 °N. In winter, the flip-flop phenomenon was observed north of 10 °N and south of 10 °S, except for the relatively high daytime values between 20 °S and 25 °S. Overall, the daytime SUHII exhibited more evident latitudinal variations than the nighttime SUHII, and the seasonal contrast of latitudinal variations for SUHII from summer to winter were more prominent at daytime.

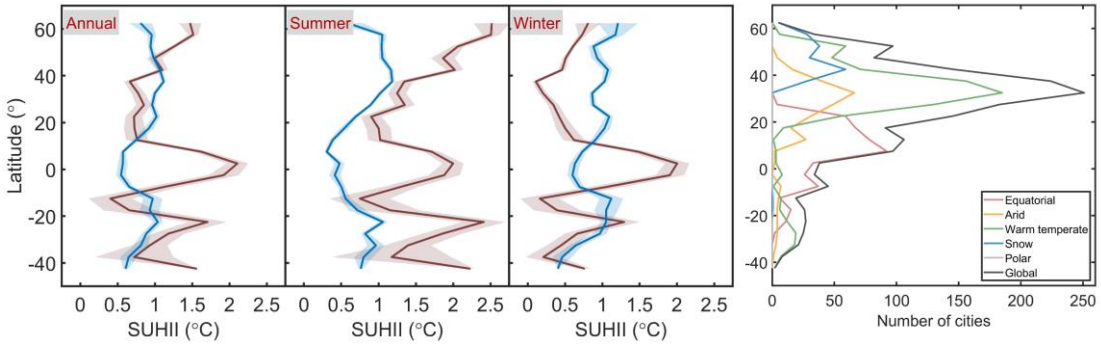

Figure 3.10 Latitudinal variations of global SUHII at a 5 ° interval. The mean values are denoted in solid lines, their standard errors are presented in shaded patches. The red and blue curves represent daytime and nighttime SUHIIs, respectively.

3.3.2. Comparison of SUHII quantified by different methods

3.3.2.1. Global pattern of long-term SUHIIs

The findings of the 419 largest global cities selected by Peng et al. (2012) were compared with the average annual, summer and winter SUHIIs of this study (Figure 3.11). The results by DUE in this study were compared to that by SUE in Chakraborty and Lee (2019) for Terra and Aqua, which are shown above and below zero axis, respectively. The daytime SUHIIs by DUE are slightly lower yet the nighttime SUHIIs are higher, than that by SUE. With respect to the findings of Peng (Peng et al., 2012), only results from Aqua are presented below the zero axis. The daytime SUHIIs by Peng are relatively higher, and

the nighttime SUHIIs are similar compared to that by DUE. Specifically, the SUHIIs from Terra by DUE are more dispersed with a larger standard deviation than that by SUE. The results from Aqua are relatively similarly distributed as that by SUE and Peng methods for daytime SUHIIs, whereas for the nighttime SUHIIs, the results are more dispersed by DUE, followed by Peng and SUE methods.

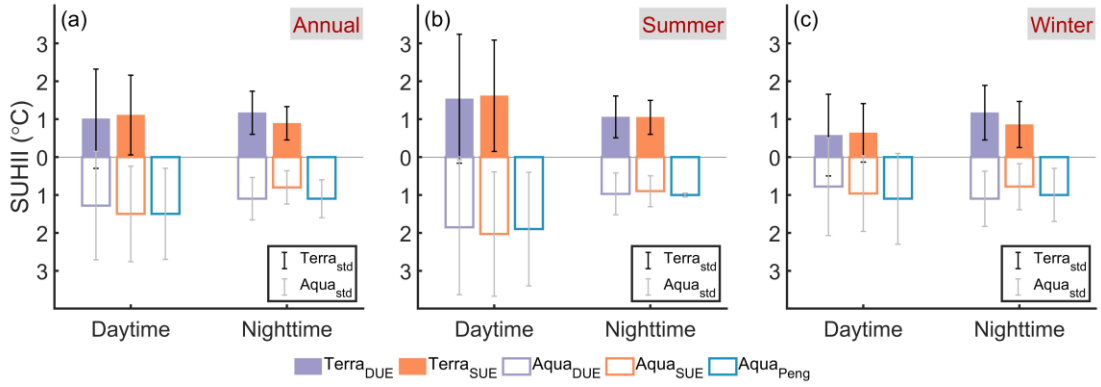

Figure 3.11 Comparison of global mean SUHII in the present study (DUE) with previous research (SUE (Chakraborty and Lee, 2019) and Peng (Peng et al., 2012)) at (a) annual, (b) summer, and (c) winter scales from Terra (above zero axis) and Aqua (below zero axis). The color bar and error bar represent the mean value and the standard deviations of SUHII, respectively.

It should be noted that to identify the urban range, some satellite towns were physically connected to a large urban cluster through the CCA algorithm; thus, the number of urban clusters in this study was lower than that of the 419 cities studied by Peng et al. (2012). Moreover, the different time spans in the three studies could cause a discrepancy in the magnitude of SUHII. Except for the aforementioned factors, the MODIS data in this study were filtered with LST errors below 2 K, which considerably altered the proportion of valid samples for the spatiotemporal integration during the SUHII analysis (Lai et al., 2018). Comparatively speaking, the DUE scheme in this study is better to depict the long-term SUHII variations with yearly dynamic urban-extent.

3.3.2.2. Global SUHIIs and their monthly variations in 2019

To further compare the DUE scheme with previous research, the global SUHII in 2019 was quantified by SUE by employing the consistent LST data source and data filtering

scheme as in 2.2.1. Figure 3.12 shows the comparison of global $SUHII_D$ and $SUHII_N$ calculated by DUE and SUE in 2019 at annual, summer and winter scales. The correlation coefficients between SUHII by DUE and SUE are above 0.8. The root-mean-square error (RMSE) of SUHII by DUE and SUE was between 0.41- 0.99 ℃. Generally, the DUE scheme produced relatively larger magnitude of SUHII with the highest mean bias error (MBE) at summer daytime (MBE = 0.28 ℃).

Afterwards, the comparison of regional averaged monthly variation of SUHII by DUE and SUE was conducted (Figure 3.13). The magnitude of monthly SUHII by DUE is relatively higher than that by SUE, except for the arid zone, which in fact is due to the larger absolute value of negative SUHII at daytime. Nevertheless, the patterns of the monthly curve were similar in these two methods. Therefore, it is rational to speculate that the interannual trends for different regions by DUE and SUE are consistent.

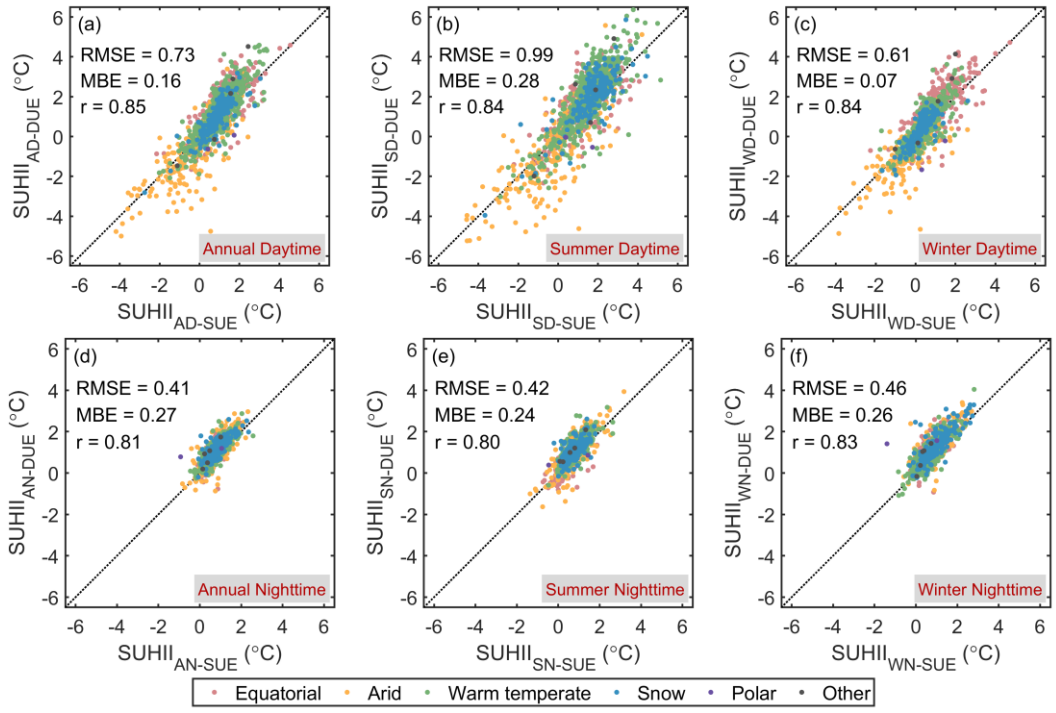

Figure 3.12 Comparison of global SUHIIs calculated by DUE and SUE in 2019 for (a) annual daytime, (b) summer daytime, (c) winter daytime, (d) annual nighttime, (e) summer nighttime, and (f) winter nighttime.

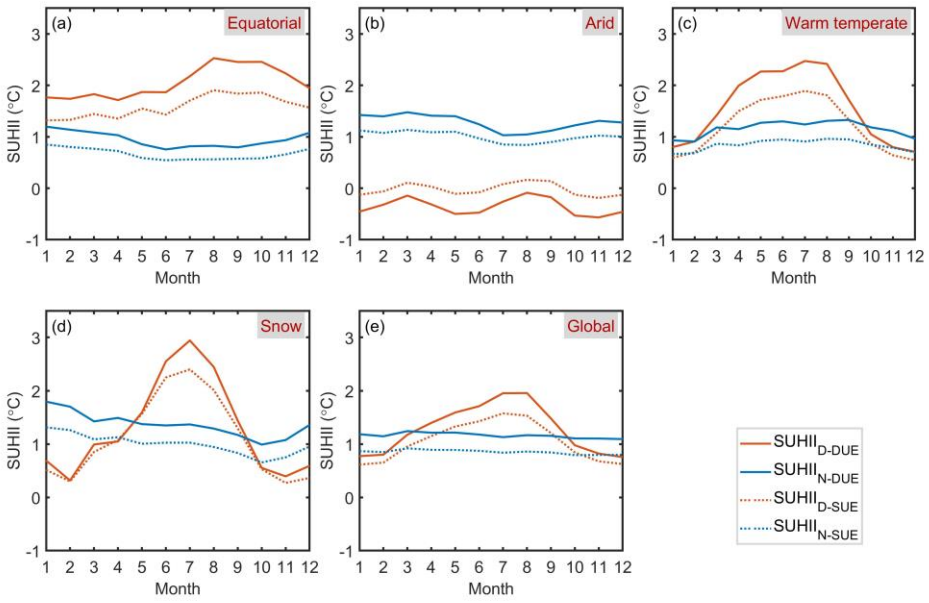

Figure 3.13 Monthly variation of regional averaged daytime SUHII ($SUHII_D$) and nighttime SUHII ($SUHII_N$) for (a) equatorial, (b) arid, (c) warm temperate, (d) snow, and (e) global zones by DUE (solid curve) and SUE (dashed curve).

3.3.3. Interannual trend of SUHII

3.3.3.1. Global pattern

Figure 3.14 presents the interannual trends of annual, summer and winter SUHIIs during 2003–2019 for each city. At the annual scale, the majority of the interannual changing rates for $SUHII_{AD}$ ranged between -1 and +1 °C/decade. The maximal variations were -2.6 °C/decade and 3.6 °C/decade for Ardabil (Iran) and Bur Sa'id (Egypt), respectively. The $SUHII_{AN}$ ranged between -1 and +0.7 °C/decade. The increasing trends were significantly observed in most global regions, especially in developing Asian countries (e.g., India, China), whereas the decreasing trends were observed in North Africa and the Middle East, indicating an increased magnitude of SUHII where negative $SUHII_{AN}$ was more frequent. In summer, the increasing and decreasing trends were similar as that in annual scale, whereas with a higher changing rate due to the higher magnitude of SHUII in

summer (Figure 4). In winter, the decreasing trends for $SUHII_{WD}$ was significant worldwide especially in North Africa and North of China with negative SUHII value (Figure 4), while the significant increasing trends for $SUHII_{WN}$ occurred in India and Northern China, which are presently experiencing rapid urbanization and population growth.

The statistics of the significant and insignificant interannual trends for global SUHII at multiple temporal scales are shown in Figure 3.15. Except for the winter daytime trends, the number of cities with an increasing interannual trend was greater than that of cities with a decreasing interannual trend. The percentage of significant increasing or decreasing trends was less than 50% at each temporal scale.

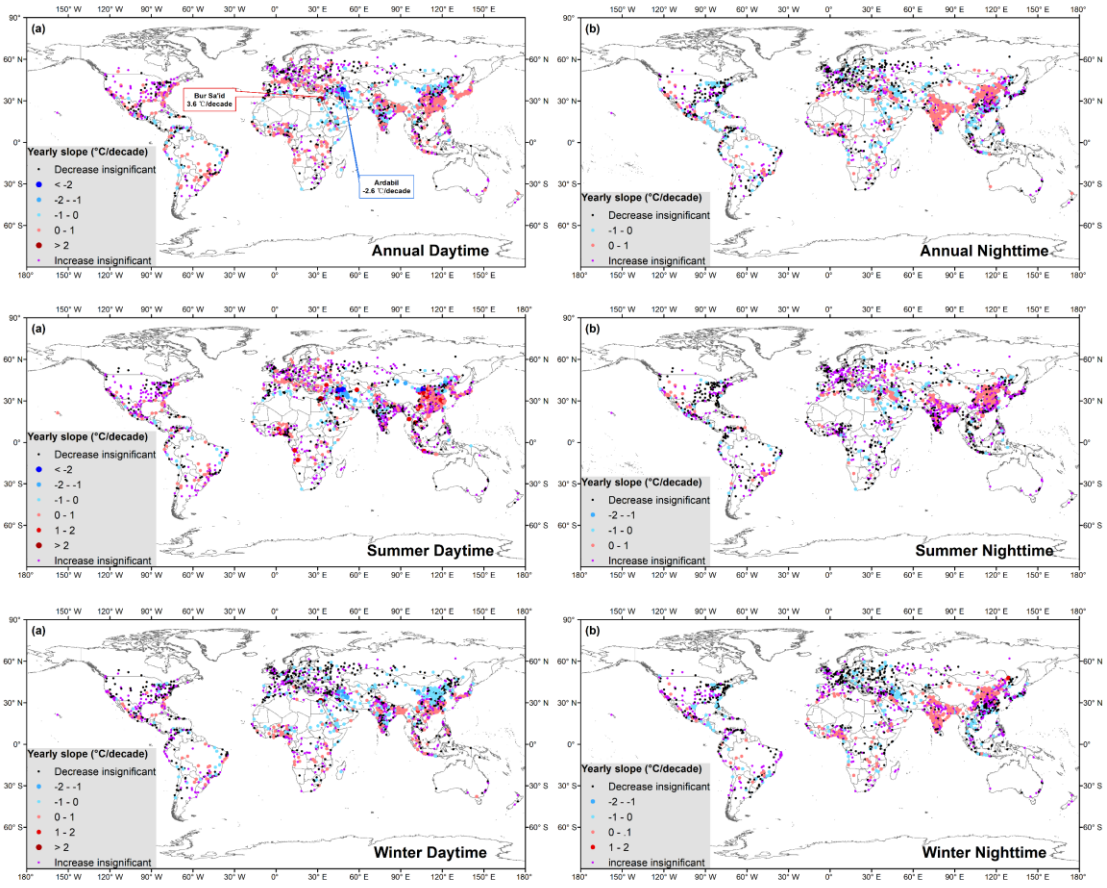

Figure 3.14 Spatial patterns of long-term trends (at 95% confidence interval) of SUHIIs for global 1711 cities during 2003–2019.

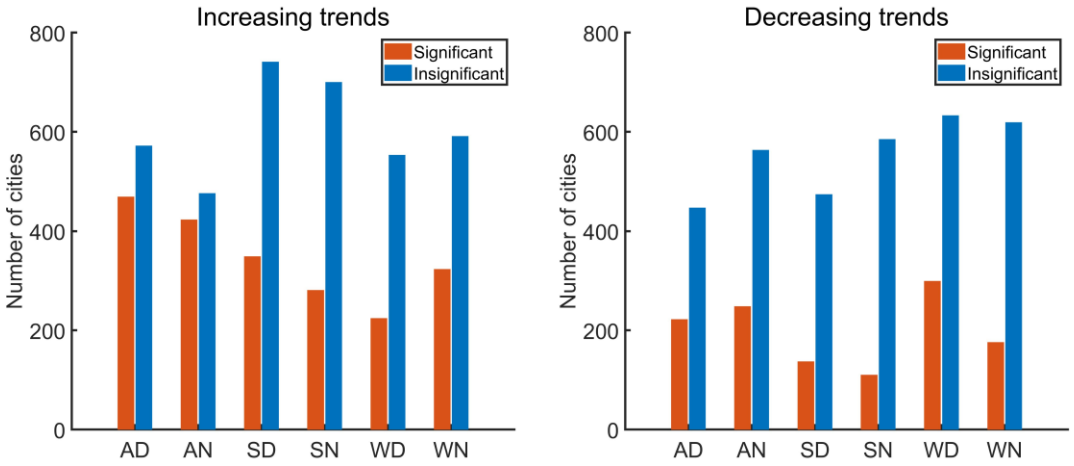

Figure 3.15 Statistics of the significant and insignificant interannual trends for the global SUHII at multiple temporal scales (at 95% confidence interval). AD: Annual daytime, AN: annual nighttime, SD: summer daytime, SN: summer nighttime, WD: winter daytime, and WN: winter nighttime.

3.3.3.2. Regional variation

Figure 3.16 depicts the interannual variations of the global mean SUHII by 1711 cities. At daytime, the annual and summer SUHIIs increased significantly at a changing rate of 0.05 °C/decade and 0.11 °C/decade, respectively, whereas the winter SUHII significantly decreased at a changing rate of - 0.03 °C/decade. At nighttime, only the summer SUHII increased significantly with a low changing rate of 0.02 °C/decade.

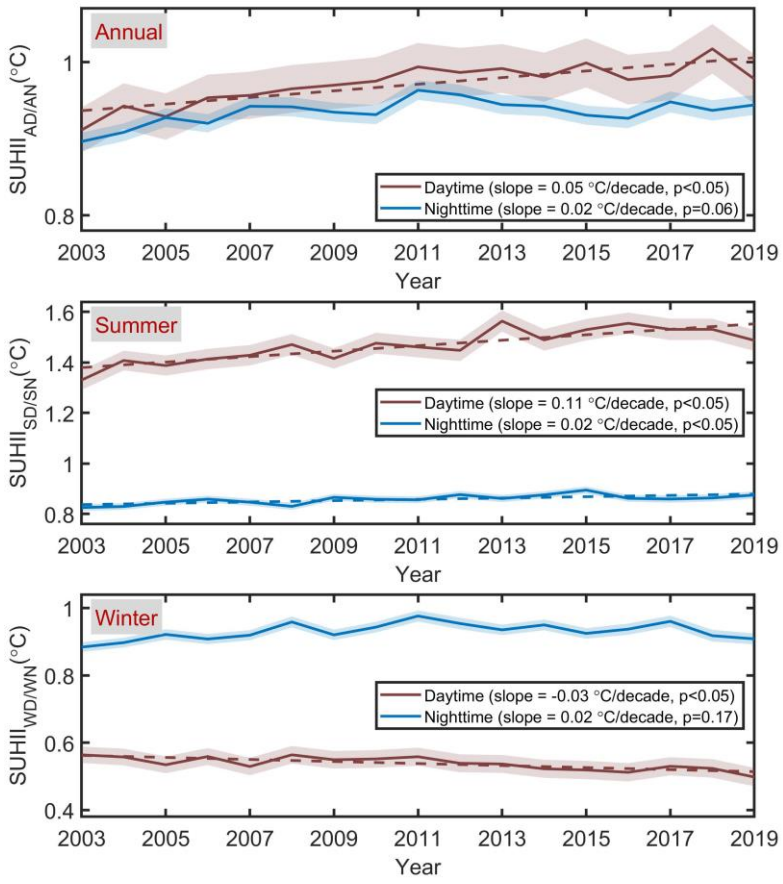

Figure 3.16 Interannual variations of the global mean SUHII for 1711 cities at the annual, summer and winter scales during 2003–2019. The solid line depicts the mean value of each year, while the shaded patch denotes the standard errors. Sen's slope was calculated at a 95% significance interval. The variations with significant trends are indicated by a dashed line.

The interannual trends of SUHII for different climate zones are presented in Figure 3.17. The warm temperate zone exhibited the most evident increasing trend for daytime SUHII (0.09 °C/decade) and nighttime SUHII (0.03 °C/decade). While the arid zone decreased (-0.08 ℃/decade) for daytime SUHII, which generally possess negative SUHII value on regional average. No significant trends of SUHII were shown at other temporal scales. Overall, the interannual variations in the warm temperate zone exhibited the most evident increasing trends in the daytime and nighttime SUHII, while the daytime SUHII in the arid zone decreased significantly.

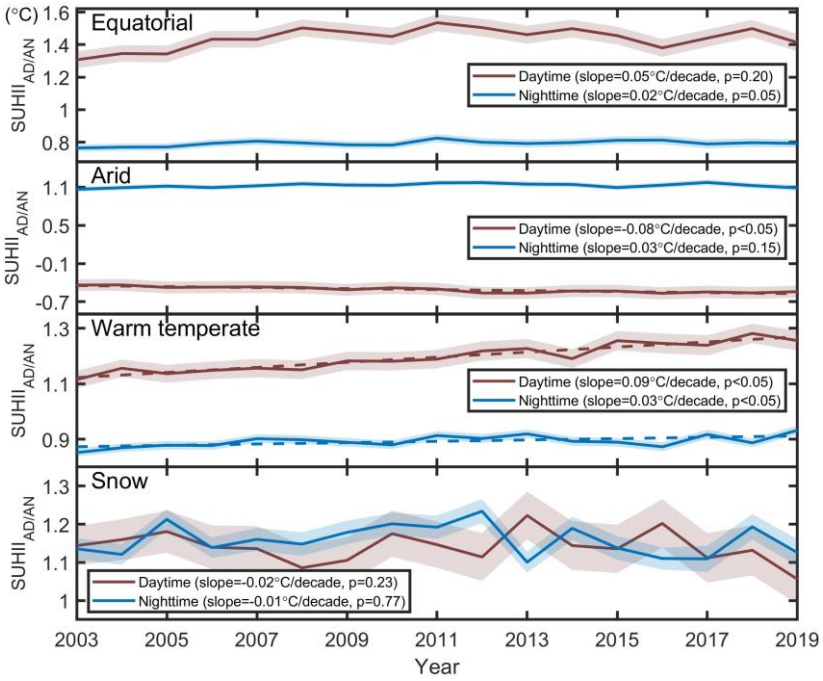

Figure 3.17 Interannual variations for the annual SUHII in different climate zones during 2003–2019. The solid lines indicate the annual mean value while standard errors are presented in shaded patches. Sen's slope is calculated at a 95% significance interval. The variations with significant trends are given in dashed lines.

3.3.4. Seasonal and day-night variation

3.3.4.1. Monthly variation

The monthly SUHII variations were averaged for 2003–2019 for each urban cluster and across different global regions. Figure 3.18 displays the monthly SUHII variations regionalized by the climate zone in the Northern and Southern Hemispheres, whereas Figure 3.19 presents the monthly variations in the global SUHII regionalized by the climate zones. The monthly SUHII variations in the Northern Hemisphere were similar to those at the global scale. However, seasonal variations were not evident in the Southern Hemisphere.

The SUHII in the Northern Hemisphere indicated more evident monthly variations at daytime than at nighttime, with the daytime SUHII peaking at 1.48 ± 1.68 °C (mean SUHII ± standard deviation) during boreal summer in July and August that decreased to 0.57 ± 1.12 °C in December within a year. The highest monthly SUHIIs for the snow (2.42 ±

1.24 ℃) and warm temperate (1.89 ± 1.34 ℃) zones were observed during boreal summer in July, while the lowest SUHIIs were observed in boreal winter in November for the snow zone (0.31 ± 0.48 ℃) and in December for the warm temperate (0.53 ± 0.86 ℃) zone. However, the monthly variations in the equatorial and arid zones were not evident. The monthly SUHII in the equatorial zone increased from June onwards and peaked in September (1.77 °C ± 1.11 °C). The monthly SUHII variations in the arid zone were evidently observed, with an annual negative SUHII and with peaks in March (-0.33 °C ± 1.75 °C) and August (-0.28 ± 2.16 °C).

The monthly SUHII in the Northern Hemisphere was more stable at nighttime than at daytime. Only the warm temperate zone showed a similar variation of nighttime SUHII to that at daytime, with the peak in August. In the snow zone, the highest nighttime SUHII was observed in February (1.56 ± 0.66 ℃) and in August (1.12 ± 0.39 ℃), while the lowest SUHII occurred in October (0.87 ± 0.46 ℃). However, an opposite trend was observed at nighttime in the equatorial and arid zones, with the lowest SUHIIs in the summer months of July (0.51 °C ± 0.50 °C) and August (0.87 °C ± 0.80 °C), while it was the highest in winter.

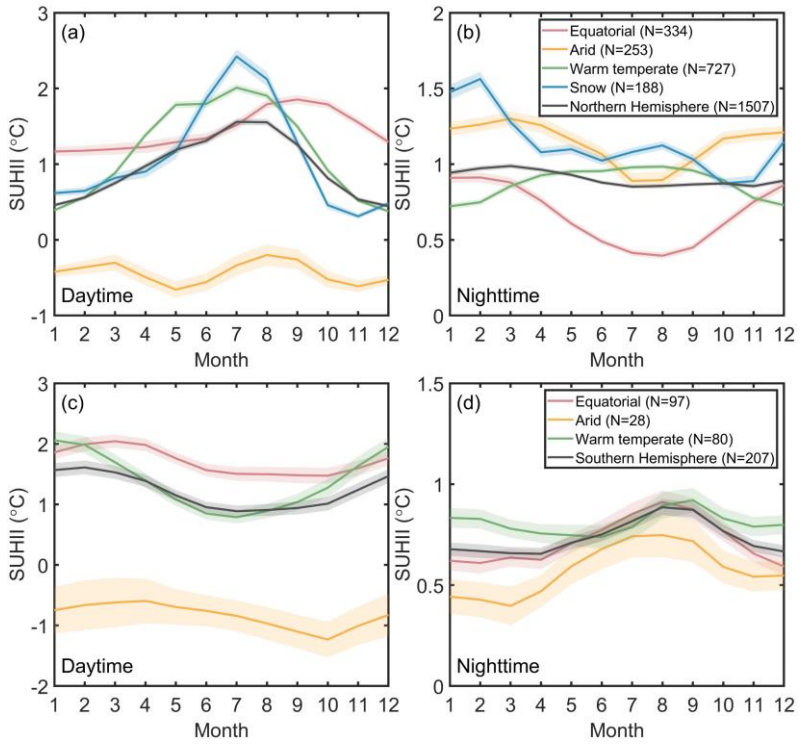

Figure 3.18 Monthly variations in the global SUHIIs for (a) daytime and (b) nighttime in the Northern Hemisphere, and for (c) daytime and (d) nighttime in the Southern Hemisphere. The mean values are denoted by solid lines, while their standard errors are presented in shaded patches.

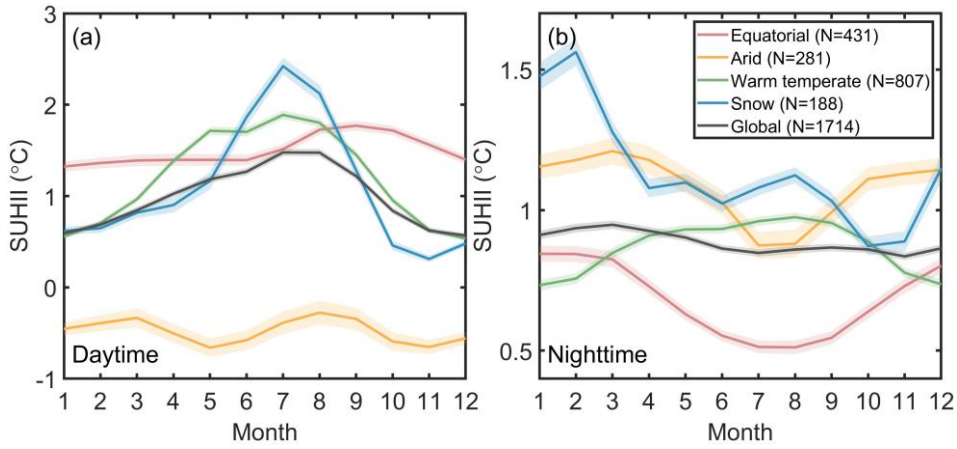

Figure 3.19 Monthly variations in the global SUHII for (a) daytime and (b) nighttime. The mean values are denoted by solid lines, while their standard errors are presented in shaded patches.

Figure 3.20 presents the differences in the highest and lowest monthly SUHIIs over a year (annual range). The annual range of daytime SUHII was 0.91 ℃ at the global scale. The most evident seasonal variation in daytime SUHII was 2.11 ℃ for the snow zone, and was followed by 1.36 ℃, 0.44 ℃, and 0.38 ℃ for the warm temperate, equatorial, and arid

zones, respectively, while the global annual range of SUHII at nighttime was 0.11 ℃. The highest seasonality at nighttime was observed at 0.69 ℃ for the snow zone, while the seasonality was insignificant in other regions (0.33 ℃, 0.33 ℃, and 0.24 ℃ for the arid, equatorial, and warm temperate zones, respectively).

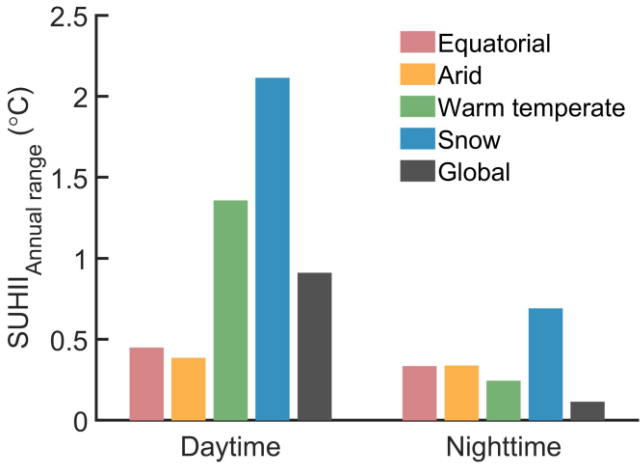

Figure 3.20 Annual SUHII range at the global scale and in different climate zones.

3.3.4.2. Day-night cycle

SUHII measurements at the four MODIS transit times were averaged from the Terra and Aqua data to curve the diurnal SUHII cycle at the global scale and for each climate zone. Figure 3.21 presents the day-night cycles of SUHII at the annual, summer, and winter averaged scales. In summer, the SUHII was the lowest at nighttime and was the highest at noon in all the zones except the arid zone. In winter, the magnitude of SUHII was lower than that in summer, and the day-night variation was reversed in all the zones except the equatorial and arid zones. The SUHII at daytime was lower than at nighttime and was the lowest at noon for the snow and warm temperate zones at the global scale. However, the magnitude of winter SUHII and its growth rate were highest at noon (10:30 a.m.–13:30 p.m.) in the equatorial region during a diurnal cycle. In the arid zone, both the summer and winter SUHIIs were higher at nighttime; this was consistent with the previous results (Figure 7) and studies (Chakraborty and Lee, 2019). The diurnal cycle at the annual scale was similar to that observed at the summer scale for each region, while the SUHII value and its increase rate from dawn to noon was low. Globally, the annual diurnal SUHII range

was 0.23 ℃ at the average scale. Furthermore, the climate conditions had the highest effect in the arid urban clusters (1.74 ℃) followed by the equatorial (0.83 ℃), warm temperate (0.46 ℃), and snow (0.22 ℃) zones.

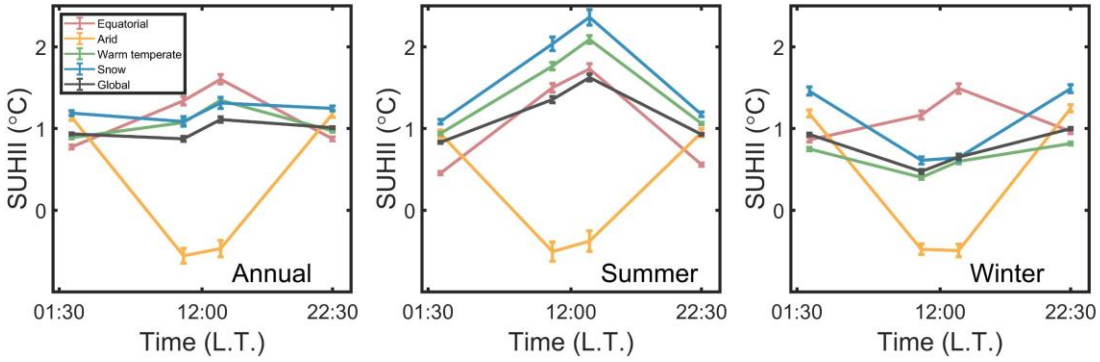

Figure 3.21 Day-night cycles of the annual averaged SUHIIs at the global scale and for the different climate zones. The solid lines denote the mean values, while the error bars represent standard errors.

3.4. Discussions

3.4.1. Spatial and temporal pattern of global SUHII

The spatiotemporal patterns global SUHII for the 1711 cities were investigated at annual, summer and winter scales. Compared with the existing global long-term studies, the SUHIIs quantified by DUE were generally higher than that by simplified urban extent (SUE). In DUE, the CCA algorithm was introduced to identify the annual dynamic urban clusters during 2003-2019, other than the fixed patterns derived from the landcover information in old years (Clinton and Gong, 2013; Chakraborty and Lee, 2019), to trace the urban sprawl more accurately. Moreover, urban fringes were excluded from the urban periphery in the rural definition. During practical applications, the influence of the SUHI footprint while refining the reference LST data in rural pixels can be avoided (Peng et al., 2012; Peng et al., 2018b), based on which our results showed a marginal disparity with the previous findings. By comparing the current findings with previous global SUHII studies in 3.2, the difference was probably due to the urban-rural extraction algorithm, data source and data filtering scheme, and varying time spans, thereby verifying the reliability of our

findings to some extent despite minor differences. By keeping these factors consistent, the further comparison between DUE and SUE in 2019 showed similar monthly variation trends. Given this, the improved DUE is assumed feasible for the long-term global SUHII study, especially for the Asian and African cities with tremendous urban sprawl in the recent years.

3.4.2. Regional contrast of climatical and latitudinal SUHII

To reveal the regional SUHII patterns, climatic and latitudinal variations in the global SUHII were further investigated. The global SUHII demonstrated an evident regional contrast. Regarding the climatic patterns, evident seasonal variations in daytime SUHII were observed in the warm temperate and snow zones. Vegetation activity significantly contributed to daytime SUHII in these regions; however, it did not contribute to strong seasonality in the arid and equatorial zones. Consequently, the summer and winter SUHIIs differed in these zones. In this study, negative SUHII was observed in the arid zone, which was contrary to the findings of Chakraborty and Lee (2019). These opposite observations may be due to the definition of urban regions; furthermore, a negative SUHII is acceptable since the cold island effect is frequently observed in the arid urban regions (Rasul et al., 2017; Haashemi et al., 2016).

The latitudinal variation for global SUHII is prominent especially in daytime, and the amplitude is more evident in summer, which can be explained by the fact that the daytime SUHII is generally regulated by solar radiation which become stronger during summers. Furthermore, the seasonal contrast of latitudinal patterns for global SUHII from summer to winter were more obvious at daytime, which were probably affected by the seasonal evolution of vegetation activity that were less prominent at nighttime. At the annual scale, the flip-flop phenomenon occurred in the arid and semi-arid zones. This was consistent with the findings of previous studies in these regions (Lazzarini et al., 2013; Chakraborty et al., 2017). However, the latitudinal variation in our study exhibited a second diurnal reversal between 10 °S and 20 °S, which was contrary to the findings of Chakraborty and

Lee (2019). The urban distribution shown in Figure 7 indicated that the number of arid and equatorial urban cities increased considerably between 10 °S and 20 °S. In our study, the daily SUHIIs in the arid and equatorial zones were 1.74 ℃ and 0.83 ℃, respectively, which were observed as 0.53 ℃ and 0.88 ℃, respectively, by Chakraborty and Lee (2019). Therefore, with high nighttime SUHII in the arid zone and low nighttime SUHII in the equatorial zone, the negative day-night differences in the arid cities observed in our study may have contributed to the flip-flop phenomenon. However, Chakraborty and Lee (2019) observed a day-night gap above zero.

3.5. Conclusions

In this chapter, GEE was used to assess the spatiotemporal patterns and investigate the driving factors of global long-term SUHII from 2003 to 2019. Specifically, an improved DUE method by incorporating the CCA algorithm was implemented to better quantify the SUHI dynamics over years. The DUE scheme generally produced higher SUHII values compared with previous SUE algorithm. Further, the DUE was validated with previous global studies and proved to be feasible to capture the long-term variation of global SUHI with the urban sprawl.

The main findings in this chapter can be summarized as:

(1) The global mean daytime and nighttime SUHII are 0.97 °C and 0.94 °C, respectively. The global SUHII exhibited evident regional contrast, with significant seasonal variations in daytime SUHII in the warm temperate and snow zones, while these variations were not observed in the arid and equatorial zones. Negative daytime SUHII values for the arid zone were detected.

(2) The latitudinal variation for global SUHII is evident especially in daytime, and an additional flip-flop region with weaker daytime SUHII than nighttime SUHII was found between 10 °S and 20 °S.

(3) At daytime, the SUHII increased significantly in annual (0.15 °C/decade) and summer (0.11 °C/decade) average, while decrease (-0.03 °C/decade) in winter. No

significant interannual trends were observed for nighttime SUHII except in summer (0.02 °C/decade).

(4) At a global scale, the annual range of SUHII during the daytime and is 0.91 ℃ (2.11 ℃, most evident for snow zone), which is relatively stable at nighttime. The daily variation of global annual SUHII is 0.24 ℃, which is disparate across different climate zones (1.74 °C, most evident for arid zone).

4 Driving factors for global surface urban heat islands

This chapter mainly explore driving factors for SUHI at different spatial scales. Based on the global surface vegetation index and surface albedo data sets, global monthly scale meteorological factor data set, population and other socio-economic factors data set, several factors are constructed concerning the surface properties, climate conditions and urbanization process. Specifically, the potential driving factors for SUHII from the global to regional scales are explored from a spatial perspective, meanwhile, of which the contribution of each factor is further revealed. Moreover, the drivers for the interannual trends of SUHIIs are from a temporal perspective. Subsequently, the spatial non-stationarity of each factor is fully explored by advanced spatial statistical models.

4.1. Introduction

Urbanization has become a worldwide historical process with the rapid development of global economic integration and population growth (United-Nations, 2019). Urban growth gradually transform the original natural surfaces of vegetation, water, soil, and so forth into impervious urban areas that are mainly composed of built-up areas and infrastructure accompanied by a large number of human activities (Vitousek et al., 1997). This changes the local meteorology, regional climate condition, and the energy exchanging mode at the interface of the surface and the atmosphere between the urban area and the surrounding suburban or rural areas (Grimm et al., 2008b). Consequently, the urban area or metropolitan area becomes hotter than the surrounding rural area, leading to the SUHI phenomenon (Oke, 1982). It is widely known that SUHIs negatively impact energy use, urban population health, and air quality, and has attracted considerable attention from scientific research teams, urban planners, and government departments (Zhao et al., 2016a; Santamouris et al., 2015). It is necessary to enhance the theoretical research on drivers for global SUHI to support effective mitigation strategies in urban management (Mohajerani et al., 2017).

As a vital phenomenon to reflect the urban thermal environment (Oke, 1982), the SUHI is the result of the combined effects of surface properties, human activities, and the metrological and climate conditions(Li et al., 2020c). The urbanization process is the primary cause of surface attribute alteration. Modifications in the LULC and surface structure constantly alter the surface properties and lead to the difference of the surface energy redistribution modes between urban and rural, which further determines the spatiotemporal pattern of SUHI (Mika et al., 2018; Feranec et al., 2019; Lee et al., 2011; Zhao et al., 2014). Human activities have dramatically increased energy consumption and generated a large amount of waste heat, leading to additional surface heat flux, which affects the urban climate and the near-surface temperature (Jin et al., 2019; Meng and Dou, 2016; Yan et al., 2016). The background meteorology and climate condition, such as the difference in surface turbulence, precipitation, wind, cloud condition, over the urban and

suburban areas often vary across different background climate zones (Zhao et al., 2014; Zhao, 2018; Manoli et al., 2019; Sun et al., 2019), also have a strong impact on the SUHI. Although the driving factors for the characteristics of SUHIs has been thoroughly explored for several decades (He, 2018; Deilami et al., 2018; Zhou et al., 2019), many inconsistencies exist in the current findings due to different time ranges, regional scopes, and analysis methods (Clinton and Gong, 2013; Zhou et al., 2017; Zhou et al., 2014a). Globally, the disparity of response mechanisms for SUHI over different regions are less investigated. Therefore, to reveal the spatial heterogeneity of the driving factors at global scale is necessary and beneficial to propose targeted mitigation guidance for SUHI.

To investigate the causality of SUHI, the model-based and statistical methods are universal in the analytical aspect of driving factors. Based on the surface energy balance (SEB) model, the underlying mechanisms can be scientifically and physically disclosed (Li et al., 2019; Manoli et al., 2019; Zhao et al., 2014). However, either the model simulation or numerical deduction process is time consuming and difficult to be conducted at a global scale. The statistical regression models are more commonly used analytical methods (Li et al., 2020c). A series of analysis tools have been adopted, such as correlation analysis (Zhou et al., 2016b; Weng, 2001; Tran et al., 2006), linear regression models (Dissanayake et al., 2019), spatial association analysis (Chen et al., 2016), and geographically weighted regressions (Buyantuyev and Wu, 2010; Deilami and Kamruzzaman, 2017). However, the SUHI is typically quantified with the LST, which is a spatial variable. Spatial heterogeneities might exist among global SUHIs and their associated driving factors, which is hardly detected by traditional statistical models (Chakraborty and Lee, 2019; Chakraborty et al., 2020; Peng et al., 2012). The driving mechanisms of global SUHI from global to local scales still needs to be further explored. Therefore, the advanced spatial statistical models are encouraged to be employed to better explore the driving factors of the spatiotemporal pattern of global SUHI (Li et al., 2020a).

Furthermore, the relationship between spatially distributed SUHI and associated drivers may not necessarily be consistent with the relationships between interannual

variations in SUHI and its associated factors for certain cities across years (Yao et al., 2018b). In recent years, the long-term trends of SUHI and the driving factors across time have gradually raised attention in several literatures (Yao et al., 2021; Li et al., 2020b). Specifically, few studies have concerned on the driving factors for SUHI dynamics at global scale. It is necessary to explore the driving factors for interannual trends of SUHII, meanwhile figure out the main driving factor and its contribution to SUHII during the urbanization process from a new perspective.

To this end, this chapter aims to explore the potential driving factors concerning the dynamic surface properties (surface vegetation condition and albedo), climate condition (precipitation and wind) and urbanization process (population and urban size), for the spatiotemporal pattern and interannual variation of global SUHI. The two analytical perspectives out of the spatial and the temporal aspects were considered simultaneously as a primitive attempt. Meanwhile, the spatial non-stationarity of the driving factors for global SUHIs on the annual, summer and winter average scales were also disclosed by advanced spatial statistical model.

4.2. Methodology

4.2.1. Urban surface energy balance

Compared with the natural surface in rural areas, the surface energy sources in urban areas have an extra radiation from anthropogenic heat in addition to solar radiation and atmospheric downward radiation. The energy received by the earth's surface is used for the heat exchange between the earth and atmosphere in the form of turbulent flow, as well as the soil heat exchange. Specifically, the urban surface energy balance equation is shown in formula (4.1):

$$R_n + Q_{AH} = H + LE + G \quad (4.1)$$

where the R_n is the net surface radiation, Q_{AH} representing man-made heat emission, H is the sensible heat flux, LE is the latent heat flux, and G represents the surface heat

storage.

The net surface radiation (R_n) includes the net surface short-wave radiation (R_{ns}) after the surface reflection of solar radiation ($SW_{\downarrow}$), and the net surface long-wave radiation (R_{nl}) obtained by subtracting surface emission radiation (δT_s^4) from the downward atmospheric long-wave radiation ($LW_{\downarrow}$). The formula is shown in formula (4.2) as follows:

$$R_n = R_{\mathrm{ns}} + R_{nl} = (1-\alpha) SW_{\downarrow} + \varepsilon \left(LW_{\downarrow} - \delta T_s^4 \right) \quad (4.2)$$

where the α is the surface albedo, the T_s is the surface temperature, and the δ is the Stephen-Boltzmann constant.

As an important energy source on the surface, changes in the R_{ns} will cause changes in the emission of surface long-wave radiation, which in turn will cause the redistribution of surface energy (Lee et al., 2011). Taking rural LST as a reference, the change in urban areas for R_{ns} , $LW_{\downarrow}$, Q_{AH} , H , and G is ΔR_{ns} , $\Delta LW_{\downarrow}$, Q_{AH} , ΔH , and ΔG , respectively. Correspondingly, the amount of urban T_s change is ΔT_s and can be deduced by formula (4.3) as follows:

$$\begin{aligned} (R_{\mathrm{ns}} + \Delta R_{\mathrm{ns}}) + \varepsilon \left(LW_{\downarrow} + \Delta LW_{\downarrow} \right) - \varepsilon\delta (T_s + \Delta T_s)^4 + \left(Q_{AH} + \Delta Q_{AH} \right) \\ = \left(H + \Delta H \right) + \left(LE + \Delta LE \right) + \left(G + \Delta G \right) \end{aligned} \quad (4.3)$$

Subsequently, combining formula (4.3) with formula (4.2) and assuming that the urban and rural surface emissivity is constant, the partial derivative of each component with respect to T_s is calculated as follows:

$$\Delta T_s = \lambda_0 \left(\frac{\partial R_{\mathrm{ns}}}{\partial T_s} \Delta R_{\mathrm{ns}} + \varepsilon \cdot \frac{\partial LW_{\downarrow}}{\partial T_s} \Delta LW_{\downarrow} + \frac{\partial Q_{AH}}{\partial T_s} \Delta Q_{AH} + \frac{-\partial H}{\partial T_s} \Delta H + \frac{-\partial LE}{\partial T_s} \Delta LE + \frac{-\partial G}{\partial T_s} \Delta G \right) \quad (4.4)$$

$$\lambda_0 = \frac{1}{4\varepsilon\delta T_s^3} \quad (4.5)$$

It can be seen that the changes in urban atmospheric conditions, surface properties,

and climate factors will cause the differences of net surface short-wave net radiation and surface downward long-wave radiation between urban and rural region. With the increase in urban anthropogenic heat emissions, the surface energy inputs in urban and rural regions are different. In addition, the distribution modes of surface latent heat flux, sensible heat flux and soil heat flux in urban will also differ from rural region. Therefore, the difference in surface radiation input and energy distribution directly lead to difference in T_s between urban and rural, that is, the SUHI phenomenon.

4.2.2. Driving factor indices

According to the findings of previous studies (Li et al., 2020c; Sun et al., 2016; Yang et al., 2019; Sun et al., 2019; Manoli et al., 2019), several potential factors associated with the surface properties, background climate conditions and urbanization were picked out to analyze the driving mechanisms of global SUHII at multiple time scales. The surface EVI and WSA differences between urban and rural regions (ΔEVI, ΔWSA) were calculated by the same method as that in Equation (3.1). The monthly accumulated precipitation (MAP) and windspeed (WS) were averaged in urban region to represent the climate condition. As for the factors related to urbanization, the mean urban population density (PD) was assumed invariant within a year, and PD for the years lacking the GPWv411 data was derived from the nearest year, while the urban area (UA) was calculated according to the previously recognized urban clusters. Thereafter, ΔEVI, ΔWSA, MAP, and WS were averaged into annual, summer, and winter scales.

4.2.3. Analytical method

Pearson's correlation analysis and multiple regression analysis were used to analyze the driving factors of SUHI across cities on the annual, summer and winter averaged scales. Pearson's correlation analysis is used to explore the impact of potential driving factors on the SUHI. The correlation coefficient (r) indicates the degree of correlation between them, which is defined as the quotient of the covariance and standard deviation between the two

variables (X,Y), as shown in formula (4.6):

$$r=\frac{\sum_{i=1}^{n}\left(X_i-\overline{X}\right)\left(Y_i-\overline{Y}\right)}{\sqrt{\sum_{i=1}^{n}\left(X_i-\overline{X}\right)^2}\sqrt{\sum_{i=1}^{n}\left(Y_i-\overline{Y}\right)^2}} \tag{4.6}$$

in which the range of r is $[-1,1]$. If $r=\pm1$, it indicates that the linear relationship between X and Y is well satisfied. A positive value of r indicates the Y increases with X, and a negative value indicates Y decrease with X. If $r=0$, it means that there is no linear relationship between the two variables.

Furthermore, the Pearson's correlation analysis between SUHII and the six indices (ΔEVI, ΔWSA, MAP, WS, PD, and UA) were also conducted to identify these driving factors for each city across the years (2003-2019), which is different from the analytical perspective across the space (cities) concerned in previous global SUHI studies (Clinton and Gong, 2013; Peng et al., 2012). To further analysis the drivers for SUHII variation, the multiple stepwise regression was conducted to figure out the main driving factors and its contribution to the slope of SUHIIs at annual, summer and winter scales.

4.2.4. Spatial regression model

In the traditional global regression model, the Ordinary Least Squares (OLS) methods is usually used, and the expression is as follows:

$$y=\beta_0+\sum_{i=1}^{k}\beta_i x_i+\varepsilon,\ \ \varepsilon\sim N\left(0,\delta^2\right) \tag{4.7}$$

where x_i and y represent the explanatory variable and the dependent variable respectively, k is the number of explanatory variables, β_0 is the intercept, β_i is the coefficient of the explanatory variable, and ε is the residual term, which must conform to a normal distribution with a zero-mean.

Considering the spatial variability of SUHI, the relationship between SUHI and the related driving factors in different regions will also vary with geographic location, which

is called the non-stationarity. The spatial statistical model can fully consider the first law of geography and detect the non-stationarity of the spatial relationship between variables. Therefore, the geographically weighted regression model (GWR) was introduced to further explore the driving factors of global SUHI at multiple temporal scales.

The GWR is a modeling method for local relationship that helps explain the spatial relationships under spatial heterogeneity or spatial non-stationary conditions (Fotheringham et al., 2003). In contrast to OLS, which can only estimate coefficients in the global sense, GWR uses the local weighted least squares method to estimate point-by-point parameters by incorporating the spatial position of the observation points into the equation. The weight is a function of the distance between the geographic location of the regression point and the geographic location of other observation points, and the result will be a continuous and smooth parameter estimation surface (Brunsdon et al., 1996). The GWR model extends the traditional global regression model and adds geographic location parameters as follows:

$$y_j = \beta_0\left(u_j, v_j\right) + \sum_{i=1}^{p} \beta_i\left(u_j, v_j\right) x_{ij} + \varepsilon_j \tag{4.8}$$

among them, $\left(u_j, v_j\right)$ is the coordinates representing the position, $\beta_0\left(u_j, v_j\right)$ is the intercept at position j, $\beta_i\left(u_j, v_j\right)$ is the local estimation parameter of the independent variable x_{ij}, p is the number of variables, ε_j is the residual at position j. Considering distance attenuation, the GWR model executes the modification by weighting the observations around all sample points. Commonly used weight matrix models include distance threshold matrix, k-neighbor matrix, quadratic kernel function matrix, and Gaussian kernel function matrix. Generally, the most commonly used Gaussian kernel function was chosen as weight:

$$W_{ij} = \frac{1}{2\pi} \exp\left(\frac{-d_{ij}^2}{2h^2}\right) \tag{4.9}$$

W_{ij} indicates the weight of the points j around the target point i in the observation

area, d_{ij} represents the distance between the observations, h represents the bandwidth to control the local regression.

Previous studies have proved that GWR is not sensitive to the choice of weight function, but it is very sensitive to the bandwidth of the weight function. In view of the heterogeneous distribution of global SUHII, the adaptive variable bandwidth was employed in this study, and the corrected Akaike Information Criterion (AIC_c) was introduced to determine the optimal model (Fotheringham et al., 2003):

$$AIC_c = 2n\log(\hat{\sigma}) + n\log(2\pi) + \frac{n(n+v_1)}{n-2-v_1} \tag{4.10}$$

where $\hat{\sigma}$ is the standard deviation of parameter estimation, n is the number of observation samples, and v_1 is the number of estimated parameters in the model. In order to evaluate the credibility of the model, it is necessary to further calculate the spatial autocorrelation coefficient of the residual. The global Moran's I index with a value range of [-1,1] is selected. A negative value indicates a negative spatial correlation, that is, high and low values will accumulate into a cluster; a positive value indicates a positive spatial correlation, that is, a cluster of high and high values, or low and low values, will accumulated into a cluster. The hither absolute value of the spatial autocorrelation coefficient indicates a stronger spatial autocorrelation (Moran, 1950).

In addition, the traditional GWR model has a scale effect, that is, the effects of certain variables may vary on different scales, while others may be spatially stable. Accordingly, Fotheringham et al. (2017) proposed a multi-scale geographically weighted regression (MGWR) model. In this study, the GWR and MGWR models were exploited within the MGWR software (Oshan et al., 2019) to analyze the spatial non-stationarity of driving factors for SUHII, and the results were compared with the findings from traditional multivariate regression models.

4.3. Global driving factors

4.3.1. Driving factors for spatial patterns of SUHII

Pearson's correlation analysis between SUHII and the relevant indexes was conducted to identify these driving factors. The Pearson's coefficients between each entity and the annual daytime and nighttime SUHIIs are shown in Figure 4.1. Furthermore, the correlation results for summer and winter are shown in Figure 4.2 and Figure 4.3, respectively.

SUHIIs exhibited a strong negative relationship with the ΔEVI at daytime (r=-0.68, p<0.001), especially during summer daytime (r=-0.75, p<0.001). High vegetation cover causes high evaporative cooling (Zhou et al., 2016c), and thus, a higher ΔEVI could lower the SUHII. The weakened vegetation activity at nighttime had a low influence on the nighttime SUHII. Global annual daytime SUHIIs were positively correlated with the WSA difference (ΔWSA) between the urban and rural regions (r=0.37, p<0.001); however, the relationship was negative at nighttime (r=-0.22, p<0.001). This was consistent with the findings of the previous global SUHII studies (Peng et al., 2012). WSA is highly related to the surface physical properties, which are determined by the surface specific heat capacity, heat conduction, and heat diffusion. The latter is a key factor in controlling the surface heat flux affecting the daytime SUHII. Moreover, since a higher WSA is accompanied by a lower EVI, ΔWSA positively affected the daytime SUHII. Generally, surfaces with lower WSAs reflect less solar radiation and increase the heat storage at daytime, which modulates the nighttime LST, and lower $_{\Delta WSA}$ also causes an increased SUHII at nighttime (Oke, 1982; Arnfield, 2003; Stewart and Oke, 2012).

Similar to the ΔWSA, the mean precipitation (MAP) exhibited a positive correlation with the annual SUHII at daytime (r=0.45, p<0.001) and a negative correlation at nighttime (r=-0.35, p<0.001). The land surface in natural rural regions generally exhibits a higher water retention ability than other urban manmade structures, such as pavements, buildings, asphalt, etc. Thus, the rural soil moisture increases significantly with increased precipitation. Further, with a large surface resistance, the rural surface evaporation increases along with

the gradual increase in LST, thereby increasing the SUHII. Additionally, the surface heat capacity increases in natural rural surfaces, and the LST gradually decreases at night, contributing to a lower SUHII with increased precipitation (Yao et al., 2018b; Du et al., 2016).

Wind can weaken the aerodynamic resistance in urban regions, which in turn increases the sensible heat flux and decreases SUHII. At the global scale, both the daytime and nighttime results exhibited a marginal effect of mean WS, despite the capacity of wind to weaken SUHII at the local climate scale (Sun et al., 2019).

The mean PD and urban area (UA) had a positive effect on the annual SUHII. The effect of PD was evidently observed at nighttime (r=0.17, p<0.001). Urban clusters with high PD and large urban size released more anthropogenic heat, and the stored heat mainly increased the nighttime LST, which in turn affected SUHII.

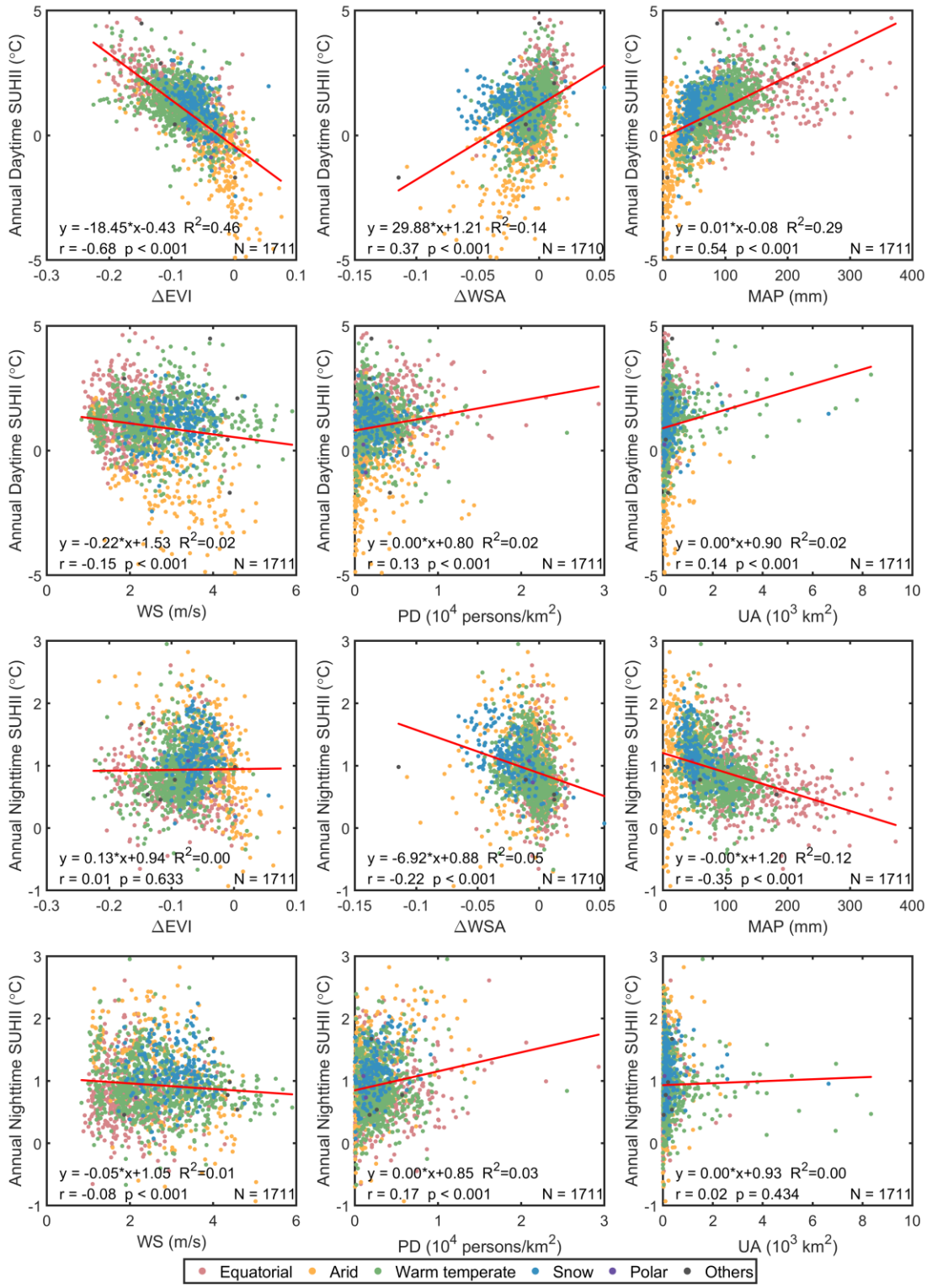

Figure 4.1 Pearson's correlation between the global annual daytime and nighttime SUHIIs and the associated driving factors. The formula represents the linear regression equation (*r*: Pearson's correlation coefficient, *p:* Significance). EVI: enhanced vegetation index, WSA: white-sky albedo, MAP: mean average precipitation, WS: Wind speed, PD: population density, UA: urban area.

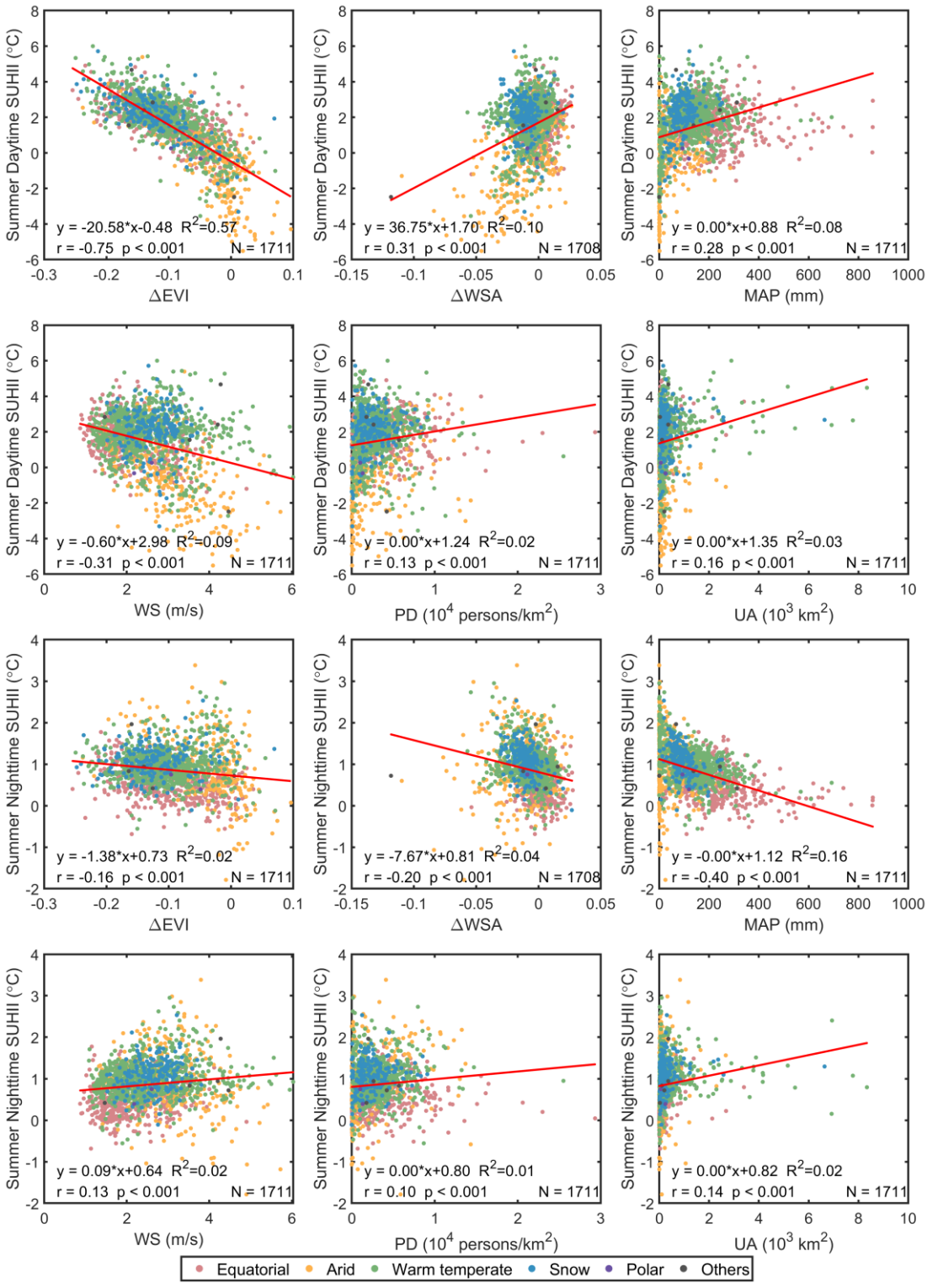

Figure 4.2 Same as Figure 4.1, but for summer.

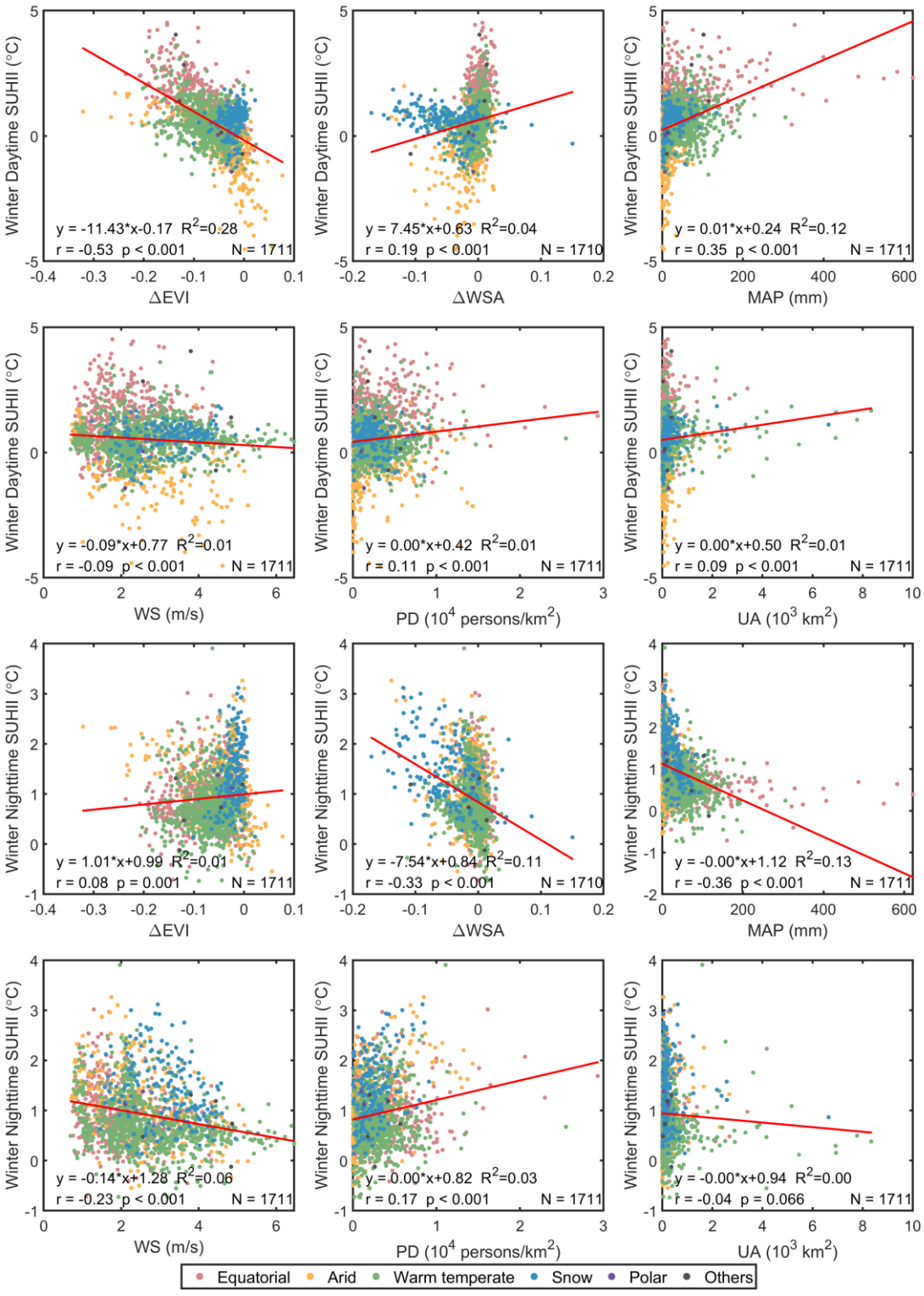

Figure 4.3 Same as Figure 4.1, but for winter.

4.3.2. Driving factors for interannual trends of SUHI

For each city, the Pearson's correlation between the SUHIIs and each of the associated factors was conducted separately across time, and the proportion of cities with positive, negative, as well as the insignificant correlations ($p>0.05$) are shown in Figure 4.4.

In Figure 4.4 (a), the annual daytime SUHII is significantly and negatively related to the ΔEVI in approximately 44% of the cities, whereas over half of them demonstrates insignificant correlation. The correlations between SUHII and ΔWSA, MAP, WS, and PD are weak and generally insignificant in over 60% of cities. The proportions of cities indicating negative correlations between SUHII and ΔWSA and WS are about 13% and 8%, respectively. While the PD, UA, and MAP are positively related with SUHII in about 22%, 21%, and 17% of cities, respectively. At nighttime (Figure 4.4 (d)), the SUHII is negatively correlated with ΔEVI in only 22% of cities. The correlations between SUHII with ΔWSA, MAP, and WS are negative in 21%, 23%, and 7% of cities, respectively. The PD and UA show positive correlation with SUHII in 22% and 19% of cities, respectively, which is similar as that in annual daytime.

In Figure 4.4 (b) and Figure 4.4 (e), the summer daytime SUHII and nighttime SUHII indicate similar proportions of each driving factors as that in annual scales. In winter (Figure 4.4 (c) and Figure 4.4 (f)), the negative correlation between daytime SUHII with ΔEVI is found in 26% of cities, which is due to the weaken vegetation activity in winter compared to summer; whereas the proportion of cities for daytime and nighttime SUHIIs with negative correlation with ΔWSA are over 17%.

Generally, the positive and negative correlations of each driving factor for the SUHIIs at each temporal scales demonstrate the similar pattern with the previous findings (Peng et al., 2012). Nevertheless, the correlation analysis for each city from a temporal perspective in this study is capable of figuring out the proportion of SUHIIs exhibiting significant correlations in terms of each factor.

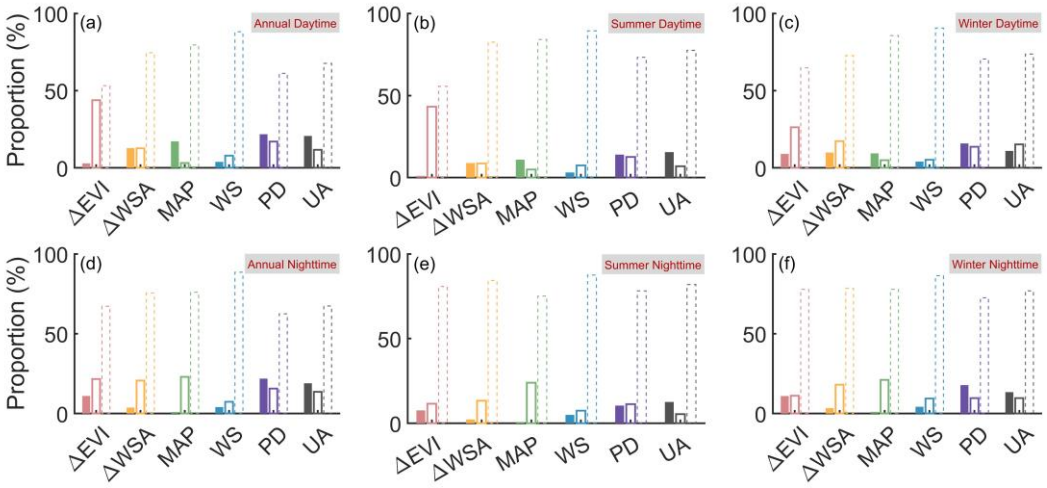

Figure 4.4 Proportion of cities with positive (filled rectangular) and negative (hollow rectangular) correlations (at 95% confidence interval) between the (a)-(c) daytime and (d)-(f) nighttime SUHIIs and each of the associated driving factors. The hollow dashed rectangular represent the insignificant correlations ($p>0.5$).

For each city, the maximum absolute correlation coefficients were figured out and was specified the dominant driver, each of which the proportion of cities are displayed in Figure 4.5. The ΔEVI is most frequently significantly correlated with SUHII with over 70% of city proportions, followed by the UA at annual scale and winter nighttime, or the PD for summer average and winter daytime. Among all available factors, the changing ΔEVI exhibited the most obvious impact on the interannual variation of SUHII over 2003-2019, followed by the urbanization terms concerning PD or UA. While the interannual trends of ΔWSA, MAP, and WS are either insignificant in itself, or not the dominants for the SUHII dynamic.

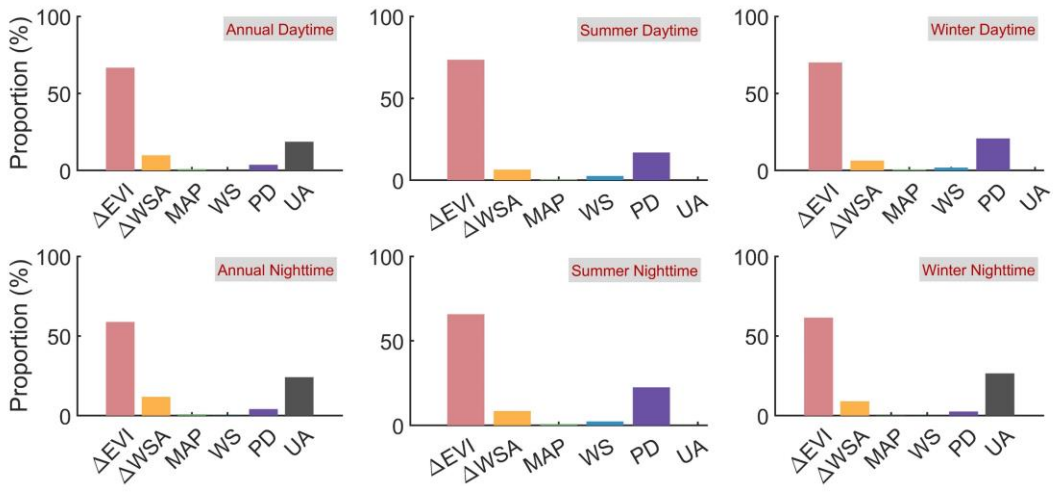

Figure 4.5 Proportion of cities with the maximum absolute correlation coefficients for each associated factor.

The multiple stepwise linear regression between the slope of SUHII and the slope of associated factors are conducted and the coefficients and contribution of main driving factors are listed in Table 4.1. Generally, the slope of ΔEVI and the slope of ΔWSA prove to be the main driving factors for daytime and nighttime SUHII trends, respectively. The city with greater increasing rate of ΔEVI is associated with smaller increasing rate of SUHII and vice versa. It contributes around 34%, 54%, and 38% to the trends of annual, summer and winter daytime SUHIIs, respectively. With respect to the ΔWSA, the interannual variation of ΔWSA mainly contributes negatively to the slope of nighttime SUHII, whose contributions are near 17%, 33%, and 22% to the annual, summer and winter scales, respectively. Specifically, the coefficients of the slope of ΔEVI at nighttime and the slope of ΔWSA at daytime for SUHIIs are estimated at the significant interval of 95% ($p<0.05$) yet with minor contribution (<6%) and thus should be ignored.

It is worth noting that the slopes of climate conditions (MAP, WS) were not investigated, which exhibit unobvious interannual variations due to the insufficient samples during 2003 and 2019. The increasing rate of PD and UA are positively correlated with the increasing of SUHII in a minority of cases, whereas the correlation is unobvious, thus excluded during the multiple linear stepwise regression.

Table 4.1 The coefficients and contribution (R^2, %) of each driving factor for the slope of global SUHII during 2003 and 2019

	Coefficients and R^2 (%)					
	Annual		Summer		Winter	
	daytime	nighttime	daytime	nighttime	daytime	nighttime
Intercept	-0.01	0.00	-0.02	-0.01	-0.02	0.01
ΔEVI_{slope}	-18.45**	-2.54*	-27.43**	-4.25*	-14.82**	-
(R^2)	**(33.69)**	(2.14)	**(54.07)**	(5.86)	**(37.78)**	(-)
ΔWSA_{slope}	11.55**	-14.05**	14.23*	-18.06**	-	-14.72**
(R^2)	(3.01)	**(17.43)**	(2.06)	**(32.79)**	(-)	**(21.79)**

(**: p<0.01, *: p<0.05)

4.4. Multiple factors analysis

4.4.1. Model diagnosis

4.4.1.1. Collinearity analysis

In statistical models, the linear correlation between two or more predictors is called multicollinearity (Alin, 2010). Due to the non-independence of predictor variables, multiple variables may explain a certain underlying mechanism at the same time, resulting in larger deviations in model parameter estimates. In order to avoid the influence of multicollinearity, Variance Inflation Factor (VIF) is usually used to judge whether there is multicollinearity between the selected predictor variables before the regression analysis. Generally, the closer the VIF is to 1, the smaller the collinearity (Dormann et al., 2013). The VIF of each of the aforementioned six factors is shown in Table 4.2. Since there is no day-night variation in the selected variable, the day-night VIF is equal. The VIF value of each variable is close to 1 and far below the threshold value of 10. Therefore, it can be considered that there is no multicollinearity between the selected factors, which can be used for the subsequent analysis of the multiple regression model.

Table 4.2 Variance inflation factor (VIF) of explanatory variables

	ΔEVI	ΔWSA	MAP	WS	PD	UA
Annual day	1.38	1.25	1.47	1.24	1.10	1.04
Annual night	1.38	1.25	1.47	1.24	1.10	1.04
Summer day	1.11	1.22	1.30	1.29	1.06	1.03
Summer night	1.11	1.22	1.30	1.29	1.06	1.03
Winter day	1.39	1.21	1.22	1.16	1.12	1.05
Winter night	1.39	1.21	1.22	1.16	1.12	1.05

4.4.1.2. Diagnostic Information

The model fitting and diagnosis information for the multivariate regression, GWR, and MGWRs model on the annual average, summer, and winter scales are shown in Table 4.3. It can be seen that the diagnosis results of OLS, GWR and MGWR models change with day-night and seasonal variations. For each temporal scale, the AICs values of the OLS, GWR and MGWR models gradually decrease, indicating that the GWR and MGWR models can ensure the accuracy while avoiding the occurrence of model overfitting as much as possible. The coefficients of determination (R^2) of the OLS regression models are 0.57, 0.24, 0.67, 0.24, 0.34, and 0.31, which are worse compared with GWR and MGWR model, respectively, for the different temporal scales. The R^2 of the MGWR model are 0.87, 0.73, 0.90, 0.74, 0.85 and 0.76, respectively. Moreover, compared with the OLS model, the absolute value of Moran's I for the GWR and MGWR models are closer to 0, indicating that the two can well capture the spatial non-stationarity of the driving factors, and MGWR performs better than GWR. In general, it can be seen that the explanatory factors of SUHII have spatial non-stationarity, and the MGWR model has the optimal performance for the interpretation of SUHII.

Table 4.3 Diagnostic Information of OLS, GWR and MGWR models

	Annual daytime	Annual nighttime	Summer daytime	Summer nighttime	Winter daytime	Winter nighttime
OLS diagnostics						
AICs	3407.272	4398.981	2975.548	4401.896	4170.915	4235.052
R^2	0.575	0.240	0.670	0.237	0.335	0.310
R^2 adjusted	0.573	0.238	0.669	0.234	0.333	0.307
Moran's Index	0.521	0.440	0.668	0.451	0.572	0.489
GWR diagnostics						
AICs	2029.597	3415.593	1697.603	3264.442	2404.918	3147.025
R^2	0.867	0.731	0.889	0.760	0.856	0.757
R^2 adjusted	0.843	0.668	0.869	0.700	0.820	0.707
Moran's Index	0.033	0.074	0.045	0.038	0.033	0.059
MGWR diagnostics						
AICs	1926.200	3258.350	1613.605	3237.352	2276.312	3057.863
R^2	0.871	0.733	0.897	0.743	0.846	0.759
R^2 adjusted	0.850	0.682	0.878	0.689	0.818	0.714
Moran's Index	-0.032	-0.001	0.006	0.004	-0.012	-0.003

4.4.2. Regression coefficient

Table 4.4 shows the comparison of regression coefficients of OLS, GWR and MGWR models. The regression coefficients of the OLS model are unique. While for the GWR and MGWR models, the global average and variance of the coefficients are given. The OLS model has insignificant parameter fitting at 95% confidence interval on several scales. Given the results of the three regression models, it can be seen that the regression coefficients of ΔEVI are all negative; the regression coefficients of ΔWSA and MAP are positive during the day and negative at night; the regression coefficients of WS are all negative, while the regression coefficients of PD and UA are positive in most cases. This is consistent with the results in section 4.3.1, and the direction of the influence of each factor on SUHII can be supported by formula (4.2), indicating that the reliability of the regression models to characterize the SEB.

Table 4.4 Regression coefficients of OLS, GWR and MGWR models

	Annual daytime	Annual nighttime	Summer daytime	Summer nighttime	Winter daytime	Winter nighttime
OLS global regression						
Intercept	-0.000	-0.000	0.000	0.000	0.000	0.000
ΔEVI	-0.544	-0.182	-0.719	-0.216	-0.469	-0.111
ΔWSA	0.152	-0.184	0.241	-0.068	-0.024*	-0.392
MAP	0.243	-0.452	0.047	-0.427	0.211	-0.297
WS	-0.037	-0.264	-0.076	-0.012*	-0.141	-0.259
PD	-0.065	0.147	-0.058	0.106	-0.028*	0.125
UA	0.152	0.026*	0.143	0.085	0.107	0.001*
GWR local regression (mean ± std)						
Intercept	0.032 ± 0.548	0.000 ± 0.781	0.104 ± 0.533	-0.877 ± 4.485	-0.071 ± 0.711	-0.264 ± 1.042
ΔEVI	-0.500 ± 0.256	-0.302 ± 0.372	-0.584 ± 0.241	-0.335 ± 0.314	-0.356 ± 0.432	-0.130 ± 0.380
ΔWSA	0.305 ± 0.218	-0.300 ± 0.316	0.313 ± 0.166	-0.127 ± 0.251	0.391 ± 0.459	-0.412 ± 0.434
MAP	0.201 ± 0.240	-0.429 ± 0.611	0.132 ± 0.397	-1.140 ± 4.118	0.199 ± 0.842	-0.860 ± 1.597
WS	-0.106 ± 0.190	-0.079 ± 0.346	-0.077 ± 0.167	-0.090 ± 0.315	-0.074 ± 0.274	-0.058 ± 0.377
PD	0.030 ± 0.339	0.151 ± 0.383	0.021 ± 0.214	0.108 ± 0.255	0.053 ± 0.279	0.204 ± 0.332
UA	-0.009 ± 0.235	0.237 ± 0.559	0.008 ± 0.218	0.193 ± 0.405	-0.057 ± 0.348	0.211 ± 0.514
MGWR local regression (mean ± std)						
Intercept	-0.081 ± 0.363	-0.037 ± 0.589	0.127 ± 0.399	-0.725 ± 1.078	-0.189 ± 0.408	-0.130 ± 0.302
ΔEVI	-0.497 ± 0.232	-0.380 ± 0.290	-0.589 ± 0.248	-0.341 ± 0.197	-0.362 ± 0.359	-0.160 ± 0.245
ΔWSA	0.302 ± 0.186	-0.331 ± 0.314	0.286 ± 0.147	-0.146 ± 0.204	0.419 ± 0.429	-0.425 ± 0.291
MAP	0.156 ± 0.025	-0.394 ± 0.440	0.147 ± 0.247	-1.086 ± 1.493	0.177 ± 0.218	-0.632 ± 0.647
WS	-0.131 ± 0.195	-0.100 ± 0.116	-0.075 ± 0.110	-0.165 ± 0.174	-0.095 ± 0.030	-0.056 ± 0.275
PD	-0.030 ± 0.124	0.177 ± 0.163	-0.003 ± 0.132	0.122 ± 0.062	-0.036 ± 0.136	0.216 ± 0.204
UA	0.031 ± 0.017	0.080 ± 0.137	0.019 ± 0.114	0.136 ± 0.345	-0.020 ± 0.236	0.067 ± 0.150

(*Insignificant, p>0.05)

4.4.3. Spatial non-stationarity

Figure 4.6-Figure 4.11 show the spatial distribution of the regression coefficients of each driving factor obtained from the MGWR model corresponding to the annual daytime, annual nighttime, summer daytime, summer nighttime, winter daytime and winter nighttime averaged scales. The color symbols represent different intervals of coefficients, while the gray circles are points where the regression is insignificant ($p>0.05$). It can be seen that the regression coefficients for each factor show large spatial variations.

For the annual daytime SUHII in Figure 4.6, ΔEVI has a significant negative contribution in most cities around the world, indicating that the increase in vegetation activity means a greater daytime LE that leads to a decrease in SUHII. In arid regions such as North Africa and the Middle East, the negative contribution of ΔEVI is more evident, where cities with cold island are distributed (Figure 3.4). Larger difference in vegetation activity between urban and rural areas generally produce stronger intensity of cold islands in these regions. There is a positive correlation between ΔWSA and the annual daytime SUHII, and the coefficients vary along with different latitude zones. The MAP is positively correlated with the annual daytime SUHII for most cities, and there is a trend of decreasing correlations from low latitudes to high latitudes in the northern hemisphere. The WS shows a significant negative contribution in some cities. The PD has the largest positive correlations in cities on the east coast of Australia, followed by cities in Southeast Asia and northeastern China. While significant negative correlations appear in some cities in North America, Western Europe and Africa. The UA has significant positive correlations mainly in North America, South America, Africa and Western Europe in the Western Hemisphere.

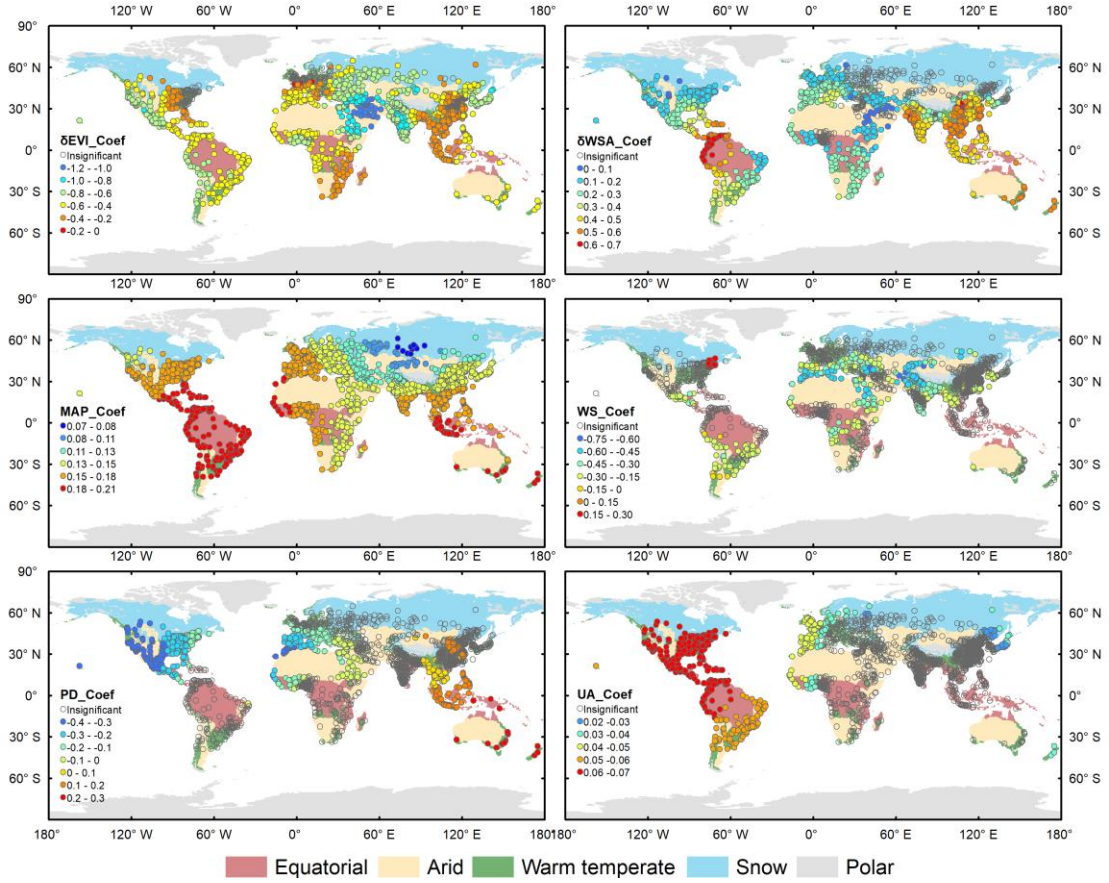

Figure 4.6 The spatial variation of coefficients of multi-independents for annual daytime SUHII.

According to Figure 4.7, it can be seen that for the annual nighttime SUHII, the correlation of ΔEVI in most cities is significantly reduced. While the ΔWSA has a negative correlation with the annual nighttime SUHII, which gradually decreases from the equatorial region to high latitudes, and a few positive contributions arise in the southern hemisphere. According to the formula (4.4) and the previous analysis, ΔWSA and solar radiation regulate the nighttime SUHII by influencing the net surface shortwave radiation at daytime. Normally, the intensity of solar radiation in the equatorial region is higher than that in high latitudes, thus the equatorial SUHII is more sensitive to changes in ΔWSA. The MAP is negatively correlated with annual nighttime SUHII, while the number of cities with significance correlation has decreased compared with daytime cases. The WS shows negative correlations, while the absolute value of the coefficients is lower than that at the daytime. It is inferred that the WS has a smaller impact on the impedance at nighttime, which leads to a weaker regulation effect on the sensible heat flux than at the daytime. For

PD in developed countries such as the United States, Europe and other regions, the positive correlation at nighttime is greater, while it is relatively minimal in India. The positive effect of UA in North America and South America is weaker at nighttime than daytime, while the impact on the SUHII in the Middle East and India has increased significantly, which may be related to the emission of more heat fluxes from human activities in these areas.

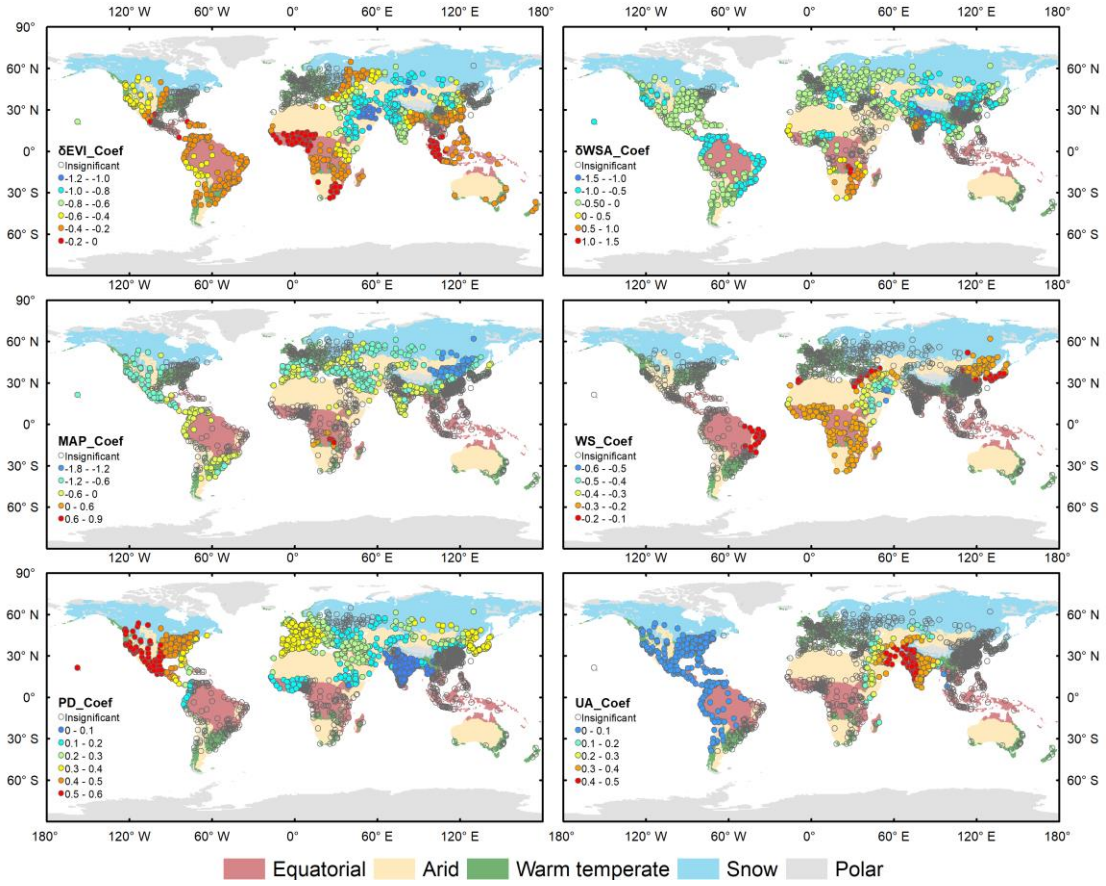

Figure 4.7 The spatial variation of coefficients of multi-independents for annual nighttime SUHII.

Figure 4.8 and Figure 4.9 show the spatial distribution of regression coefficients of summer daytime and nighttime SUHII, respectively. The negative correlation of ΔEVI with summer daytime SUHII is more obvious compared with the annual cases. The latitudinal variations of correlation with ΔWSA are not that obvious at daytime, and the negative correlation at nighttime is also lower than the annual average cases. The daytime positive correlation and nighttime negative correlation with MAP in the northern hemisphere is significantly higher than that in the southern hemisphere. It may be related to the stronger vegetation activities in the northern hemisphere in summer. Precipitation not only regulates

the evaporation ratio by affecting the surface soil moisture, but also promotes the growth of vegetation, making the summer SUHII in northern hemisphere more sensitive to changes in MAP. The negative influence of WS on summer SUHII at nighttime is stronger than that at daytime. The PD has a significantly higher impact on SUHII at nighttime than during the daytime. The UA is significant positively correlated with summer daytime SUHII in North America and Western Europe in the Western Hemisphere, while in India, the impact of UA is stronger on nighttime SUHII.

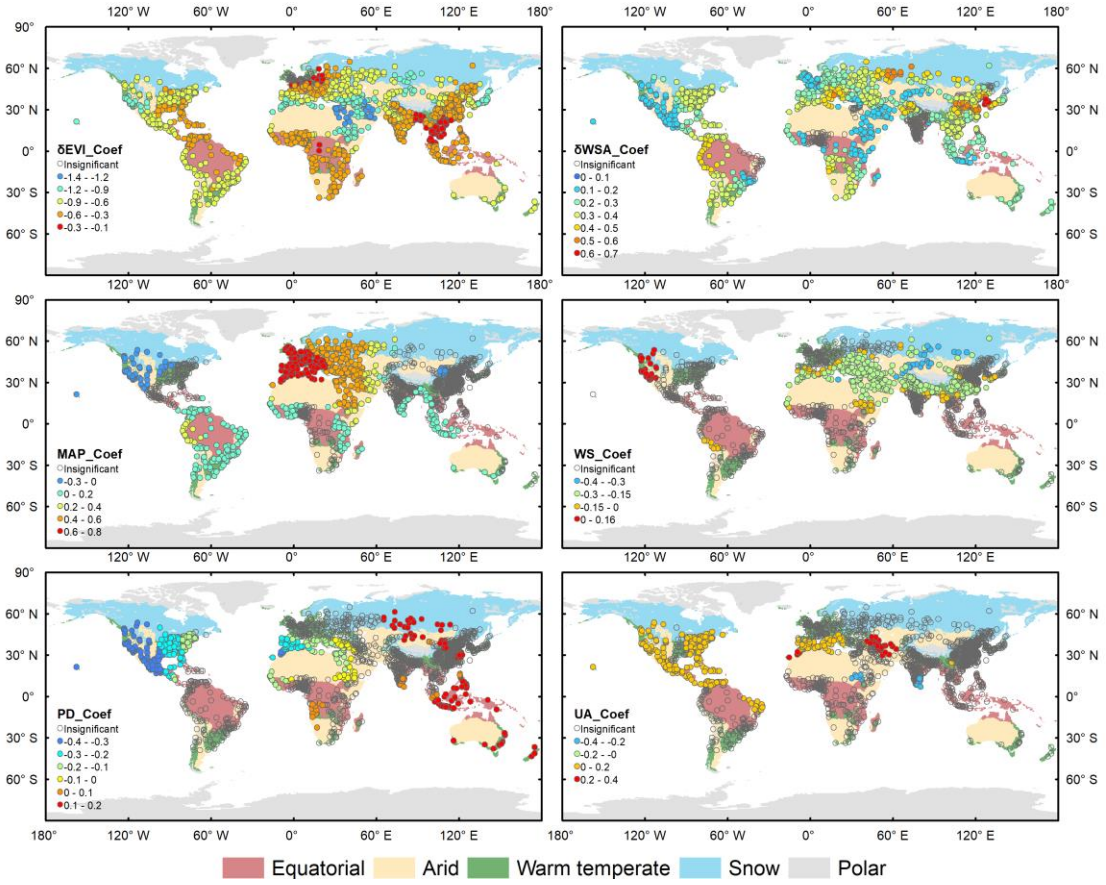

Figure 4.8 The spatial variation of coefficients of multi-independents for summer daytime SUHII.

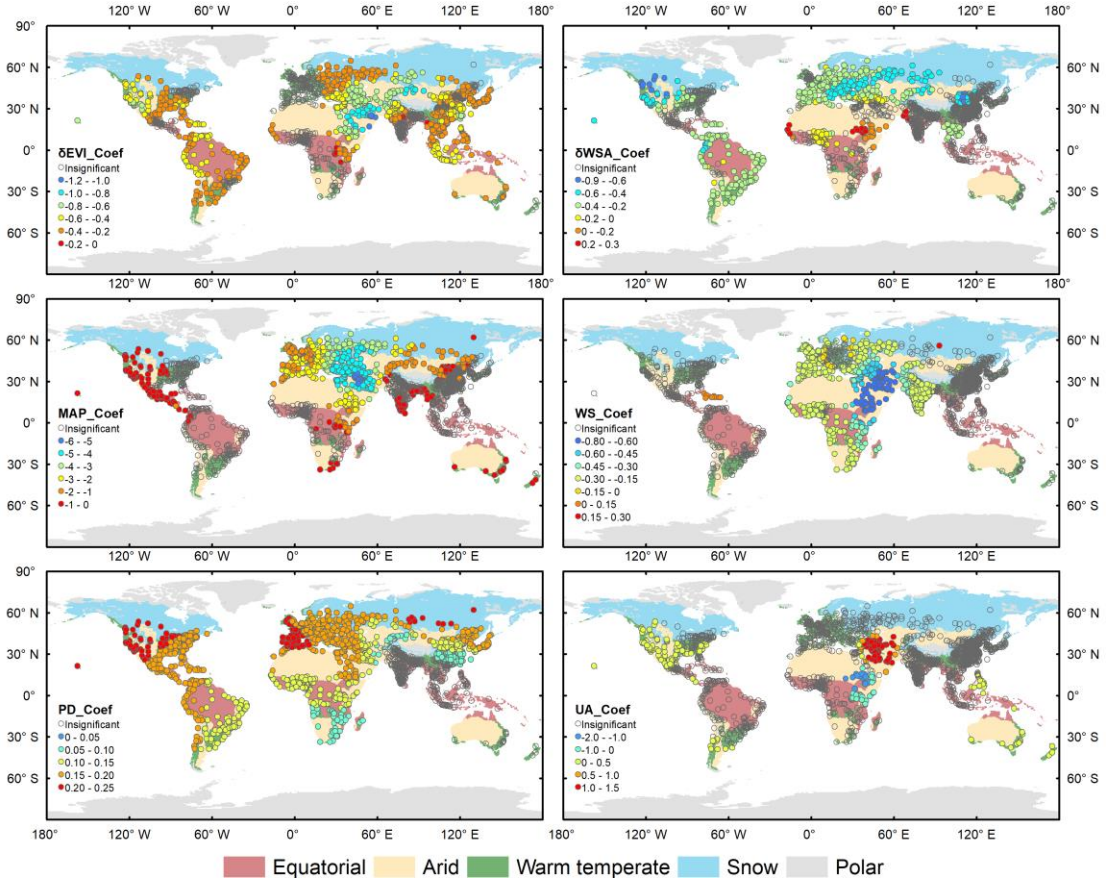

Figure 4.9 The spatial variation of coefficients of multi-independents for summer nighttime SUHII.

Figure 4.10 and Figure 4.11 show the spatial distribution of regression coefficients of winter daytime and nighttime SUHII, respectively. Compared with the results in summer, the negative contribution of ΔEVI in the daytime is relatively weaker, which may be related to the weakening vegetation activities in winter. The positive correlation of ΔWSA with winter SUHII shows a decreasing trend from the equator to higher latitudes during the daytime, while the negative correlation at nighttime decreases. In winter, the positive correlation between MAP and daytime SUHII is more obvious in the equator and arid zone, while the negative correlation between MAP and nighttime SUHII decreases from the equator to the poles. The WS shows negative correlation, which is more evident during the daytime than that at nighttime. The PD and UA have significant positive contributions especially at nighttime. In most cities in the northern hemisphere, the PD is more positively correlation with nighttime SUHII. While the positive contribution of UA at nighttime is greater in areas such as East Africa and India.

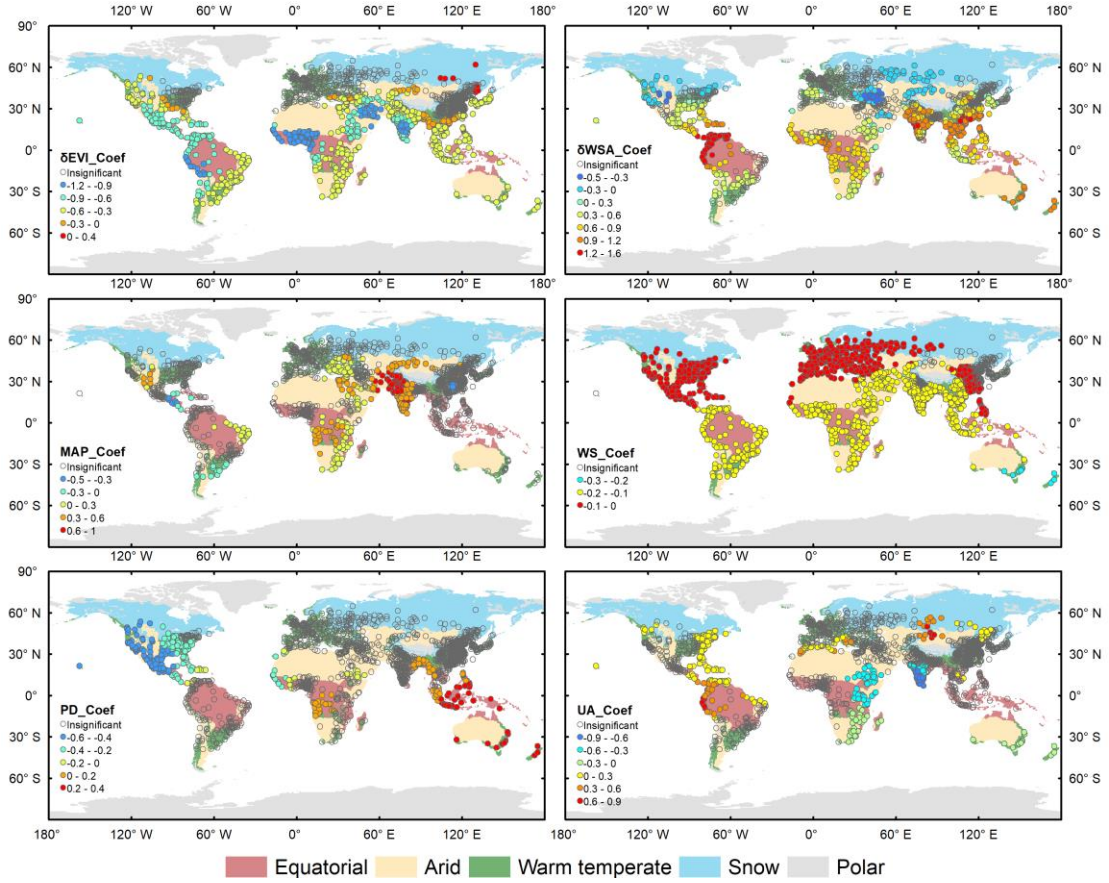

Figure 4.10 The spatial variation of coefficients of multi-independents for winter daytime SUHII.

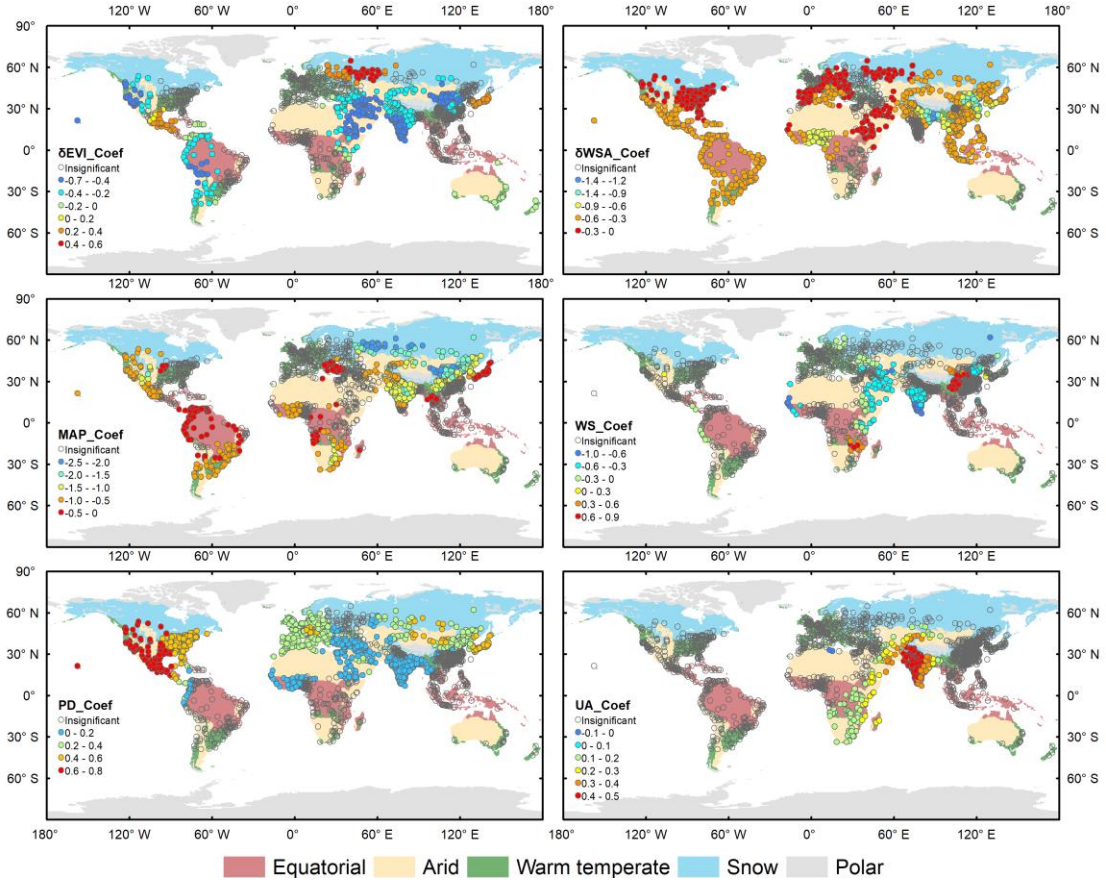

Figure 4.11 The spatial variation of coefficients of multi-independents for winter nighttime SUHII.

4.5. Conclusions

In this chapter, the potential driving factors affecting the global SUHII concerning surface properties, meteorological and climate conditions, and urbanization process were constructed based on the SEB. By employing the correlation analysis, the contributions of each driving factor and SUHIIs are explored across global cities. From a temporal perspective, the driving factors for interannual trends of SUHIIs from 2003 to 2019 are further investigate for each city across time. In order to explore the contribution of multiple factors, we compared the findings of the multiple linear regression model, GWR model and MGWR model on multi-factor contributions. The results show that GWR models and MGWR models captured the spatial non-stationarity of driving factors with better model fitting result. Among them, the MGWR model performs best. Finally, the global pattern of the coefficients is revealed from MGWR model at different temporal scales.

This chapter mainly draws the following conclusions:

(1) The ΔEVI is positively correlated with daytime SUHII, which mainly due to the negative contribution of surface latent heat flux to SUHII.

(2) The ΔWSA has positive and negative correlations with daytime and nighttime SUHIIs, respectively. The decrease in ΔWSA increase in the heat storage during the day, which will release at nighttime and increase the nighttime SUHII.

(3) The MAP is positively correlated with daytime SUHII and negatively correlated with nighttime SUHII. With higher soil moisture content caused by more precipitation, the specific heat capacity of the rural surface changed, and thus the sensible heat flux decreased at daytime and increase at nighttime, thus lead to opposite mechanism.

(4) The WS is mainly a negative contribution to SUHII, which usually reduces the aerodynamic impedance and causes an increase in sensible heat flux, thereby reducing the strength of the heat island.

(5) The positive correlation between PD and UA with SUHII is more significant at nighttime, which mainly affect SUHII through the increase of long-wave radiation caused by anthropogenic heat emissions and air pollution.

(6) The interannual vegetation condition (ΔEVI) exhibited the most obvious negative correlations with the long-term daytime SUHII with the contributions rate of 34%, 54%, and 38% at the annual, summer and winter scales, respectively. The slope of surface albedo (ΔWSA) referring the surface properties mainly contributes negatively to the slope of nighttime SUHII, with the contributions of 17%, 33%, and 22% to the annual, summer and winter scales, respectively. It implies the surface properties vulnerable to land use and landcover change, the greenness in urban area, and human activities should be concerned specifically in SUHI mitigation.

(7) The contribution of multiple factors is spatially non-stationary on a global scale. The results from MGWR model with variable bandwidth local regression method performs optimal estimation of the contribution coefficient than GWR model.

5 Quantification of surface urban heat islands under multiple rural land use types

At present, the urban-rural temperature difference method is mostly used to quantify the intensity of SUHII. The accurate determination of LST in the rural background is very important to the quantification result. In order to verify the credibility of the quantification method and exclude the impact of the diversity of rural land use types on SUHII, this chapter will select 34 major cities in China as the study area. Firstly, based on the rural areas identified by the dynamic urban-extent scheme, the composition and main component of the various rural land use types for each city are explored. Secondly, new calculations of SUHII are proposed based on single or multiple land use types in rural areas. Subsequently, to verify the feasibility and credibility of urban-rural difference method in depicting the regional pattern and temporal variation of regional SUHII, the spatial integration and temporal variation of SUHII from different quantitative methods are compared within each geographical division. Finally, a multi-scale comparative analysis of the SUHII in different geographical regions of China is carried out on day-night cycle, monthly average, and interannual variation.

5.1. Introduction

In recent years, the UHI phenomenon has been observed in thousands of cities around the world (Clinton and Gong, 2013; Peng et al., 2012; Stewart and Oke, 2012). A large number of studies have shown that UHI can cause a series of environmental alterations, such as changes in regional climate (Shepherd, 2005; Arnfield, 2003), impaired vegetation growth (Zhao et al., 2016a; Zhou et al., 2016a), and water and air quality deterioration (Grimm et al., 2008a). Considering that urban areas account for approximately 55% of the world's population, these changes will probably threatens human survival and development (Bai et al., 2018), leading to increasing morbidity and mortality (Patz et al., 2005), and even causing potential threats of violence (O'loughlin et al., 2012). As the process of urbanization have profoundly affected the living conditions of human beings (Kalnay and Cai, 2003), it is essential to accurately monitor the UHI pattern to support effective mitigation strategies in urban thermal environment management (Mohajerani et al., 2017).

With the development of remote sensing technology, a growing number of researches have revealed the spatiotemporal patterns of global SUHI, and its associated driving factors on a local, regional, and global scale with the remotely sensed LST products (Zhou et al., 2019). At present, the urban-rural difference method is one of the most commonly used scheme in the quantification of SUHI intensity, while the identification of urban region and rural background is inconsistent (Zhou et al., 2014a; Peng et al., 2018a; Zhang et al., 2010; Yu et al., 2019), which is decisive for the result of SUHI study (Deilami et al., 2018; Clinton and Gong, 2013). Therefore, the sensitive of SUHI intensity to its quantification need to be explored in-depth.

During the calculation of SUHII, the most important aspect referring to the "rural" reference was stressed out that not only the threshold of altitudinal difference in urban and non-urban points should be lower than 30m, the proximity to water bodies in urban and non-urban points was supposed to be similar (Martin-Vide et al., 2015). Additionally, the seasonal change characteristics of SUHII in a semi-arid city were analyzed based on the LST of the entire rural land surface and woodland, respectively, as the background and

demonstrated completely opposite results (Haashemi et al., 2016). Currently, the elevation control and water body exclusion are widely concerned (Peng et al., 2012; Chakraborty and Lee, 2019). Nevertheless, the influence of the diversity of rural land use type has received less attention in regional SUHI studies involving multiple cities. For the rural surface composed of multiple types of land use, whether SUHII quantified in the context of the entire background has an impact on its multi-scale spatiotemporal patterns has not yet been fully explained. Therefore, in order to accurately revealing the spatiotemporal pattern of SUHII and its driving factors, it is of great significance to explore the quantification of SUHII under multiple rural land use types (Zhao et al., 2016b).

With the urbanization process, China has become one of the most populous developing countries with vast terrain, complex climate and topography conditions, and diverse rural land use types corresponding to cities in different regions (Song and Deng, 2017; Liu, 2018). A large number of studies have shown that the SUHI phenomenon exist in most large cities across China which have been fully revealed at multiple scales (Zhou et al., 2014a; Yao et al., 2021; Yang et al., 2019; Chen et al., 2006). Recently, the magnitude of SUHII in China's major cities was proved definition-independent in terms of Peng et al. (2012) and Zhou et al. (2014a), while their diurnal and seasonal patterns were similar across these definitions (Zhou et al., 2016c). With respect to the sensitivity of SUHII to rural background with compound LULC types, different quantifications of SUHII by filtering multiple rural land use for a single city need to be fully considered while investigating its regional patterns.

Given this, this chapter first investigate the rural land use types and urban form expansion of 34 China's major cities during 2003 and 2019. Subsequently, new quantifications of SUHII are constructed based on the first and second principal rural land use components. Thereafter, the primitive SUHII quantified by the whole rural LST was validated with the new indices regarding the monthly averaged SUHII and its long-term variations. Finally, the spatiotemporal pattern of SUHII in China in terms of the day-night cycle, monthly variation and interannual trend was further investigated by the geographical zones.

5.2. Methodology

5.2.1. Study area

A total of 34 China's provincial capitals, municipalities and special administrative regions are selected as the research targets. According to the rural region identified in chapter 3.2.1, the principal and/or second composition, which occupy around 40%-50% of the whole rural land use types for each city are determined with the land use data from MCD12Q1during 2003 and 2019. As shown in Figure 5.1, the center point is identified with the abbreviation of the city name (BJ: Beijing, CC: Changchun, CD: Chengdu, CQ: Chongqing, CS: Changsha, FZ: Fuzhou, GY: Guiyang, GZ: Guangzhou, HAK: Haikou, HB: Harbin, HF: Hefei, HK: Hong Kong, HT: Hohhot, HZ: Hangzhou, JN: Jinan, KM: Kunming, LS: Lhasa, LZ: Lanzhou, NC: Nanchang, NJ: Nanjing, NN: Nanning, SH: Shanghai, SJZ: Shijiazhuang, SY: Shenyang, TJ: Tianjin, TY: Taiyuan, UQ: Urumqi, WH: Wuhan, XA: Xi'an, XN: Xining, YC: Yinchuan, ZH: Zhuhai , ZZ: Zhengzhou), the principal and/or second land use types in rural areas are marked with corresponding numbers. It should be noted that the urban area of Macau was connected with Zhuhai after executing the CCA algorithm. The 34 cities are distributed with diverse rural land use types, which were geographically divided into the Northwest, the Northeast and the Southeast regions.

In general, most cities in the Northwest region are in arid climate zone, whose principal rural land use types are grasslands. Among them, the second rural land use types of Yinchuan and Lhasa are cropland and barren, respectively. Cities in the Southeast region are mostly in the warm temperate zone, and the principal rural land use types are savanna and evergreen broadleaf forests. Mixed type of savanna and cropland for Nanjing, Shanghai and Chongqing, evergreen broadleaf forests and woody savannas for Hong Kong, evergreen broadleaf forests and savannas for Taipei are found among them. With respect to the Northeast region, the principal rural land type for each city is cropland. Overall, there is a diversity of rural land use types across 34 major cities in China, which is suitable for analyzing the urban-rural LST difference method under complex rural background.

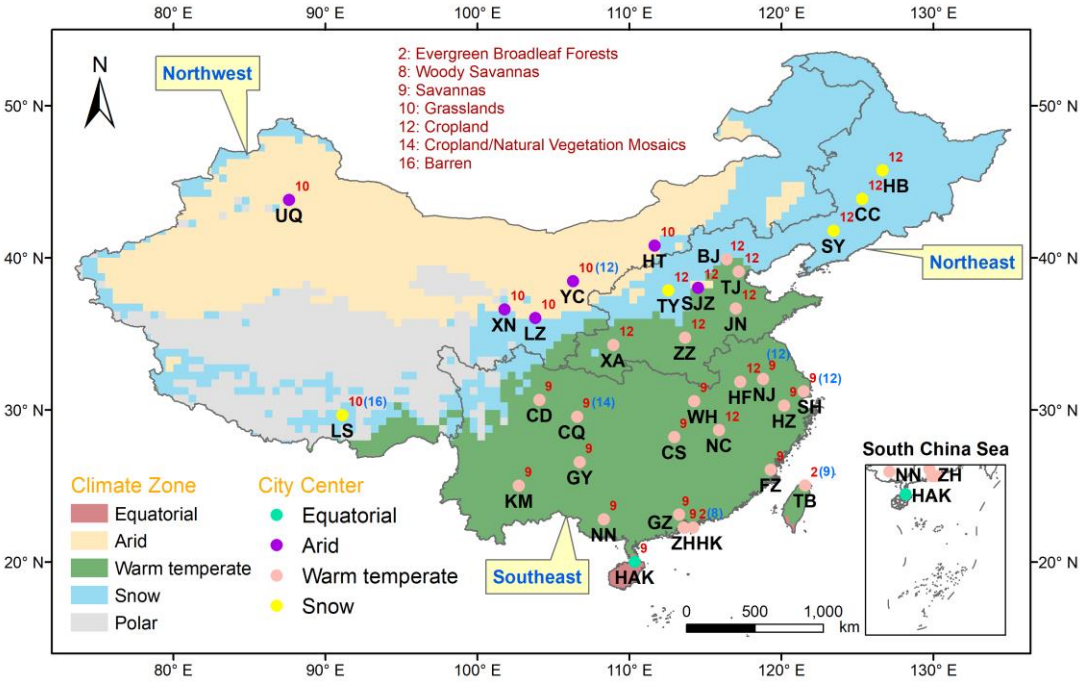

Figure 5.1 The spatial pattern of 34 China's cities with its principal and/or second rural land types.

5.2.2. Urban form expansion

The urban form expansion of the 34 cities identified by the CCA algorithm are shown in Figure 5.2, where the red and blue areas are the urban boundaries in 2003 and 2019, respectively. Due to the possibility of connecting large cities with surrounding satellite cities, the urban area identified by the CCA algorithm will exceed the actual administrative boundary. Among them, Shanghai and Guangzhou are the urban agglomerations that connect the central large city and the surrounding cities.

Correspondingly, the urban area and change rate of each city (urban agglomeration) from 2003 to 2019 are shown in Figure 5.3. It can be seen that the urban areas of Shanghai, Guangzhou, Beijing and Tianjin all exceed 2000 km^2. With the exception of Lanzhou, Lhasa and Hong Kong, the urban area has a significant increasing trend for all cities, and larger cities generally present a higher changing rate. For example, the urban area of Shanghai, Guangzhou, Beijing and Chengdu increase at the rate of more than 50 km^2/a. The expansion of urban form and urban size is usually accompanied by changes in the surrounding rural land use types, which further support the necessity of using the dynamic

urban-extent to accurately quantify the intensity of SUHI.

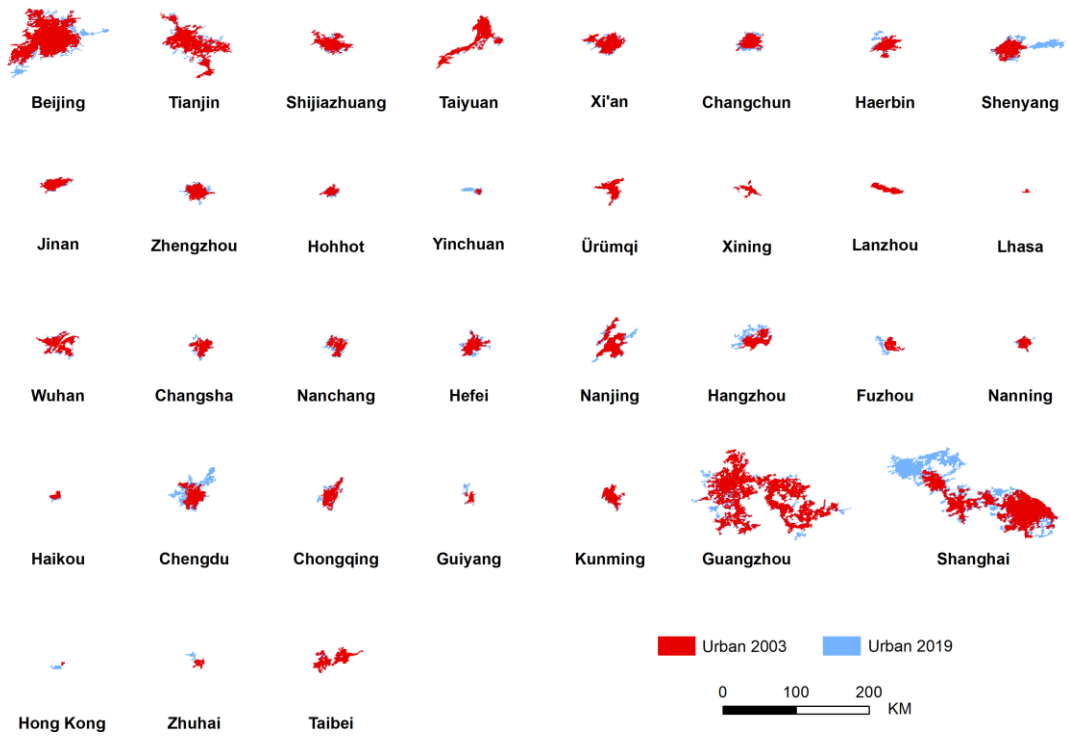

Figure 5.2 The spatial variations of urban morphology of 34 China's urban agglomerations from the year 2003 to 2019.

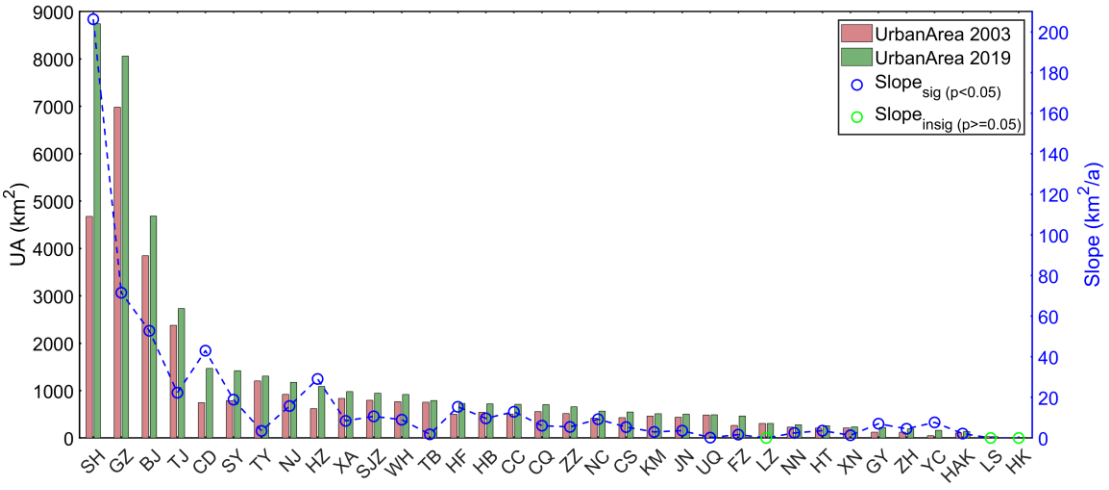

Figure 5.3 The urban area and expanding rate for 34 China's urban agglomerations during the year 2003 and 2019.

5.2.3. New quantification of SUHII

Different from the method in 3.2.2 to determine the average LST in the whole rural surface, the valid rural LST pixel for the principal and second rural land use type are picked out to calculate the corresponding reference LST, respectively, and the new quantifications of SUHII are shown in equation (5.1) and (5.2) as follows:

$$SUHII_1 = T_u - T_{r1} \tag{5.1}$$

$$SUHII_2 = T_u - T_{r2} \tag{5.2}$$

where the T_u is the average urban LST, the T_{r1} and T_{r2} are the average LST of the principal and second major rural land use types, respectively, and $SUHII_1$ and $SUHII_2$ are the corresponding intensity of SUHI. Hereafter, the SUHII indicates the original quantification of SUHI intensity by the whole rural LST.

5.3. Comparison of SUHIIs under multiple rural land use types

5.3.1. Comparison of monthly SUHIIs

Pearson's correlation coefficient is used to quantify the correlation between the daytime and nighttime SUHII and $SUHII_1$ and $SUHII_2$. The scatter plots of SUHII and $SUHII_1$ and $SUHII_2$ are shown in Figure 5.4 and Figure 5.5 for daytime and nighttime conditions, respectively. At daytime, except for Xining in the northwest region and Hong Kong in the southeast region, the correlation coefficients of SUHII and $SUHII_1$ or $SUHII_2$ in all cities are above 0.9. At nighttime, except for $SUHII_2$ calculated by cropland in Lhasa, and $SUHII_1$ and $SUHII_2$ calculated by evergreen broadleaf forests and savannas, respectively, in Hong Kong's, the correlation coefficients of SUHII and $SUHII_1$ or $SUHII_2$ in each city are all above 0.9. In general, except for some cities with mixed rural land use types, the difference between SUHII and $SUHII_1$ or $SUHII_2$ in 34 major cities in China is slight.

At daytime, the LST is mainly affected by vegetation activities and others. In the northwest region, the first land use type in rural areas is grassland. It can be seen from Figure 5.4 that for Yinchuan, $SUHII_2$ is underestimated in low-value regions and over-estimated in high-value regions. As the high and low value regions correspond to different growth seasons of vegetation, the rural LST is lower in the season of lush vegetation activity, which results in a greater $SUHII_2$, and vice versa. Lhasa locates at a high altitude, and the surrounding farming and pastoral areas are dominated by grassland and barren, where the proportion of grassland has increased in recent years (Gao et al., 2018). Under normal circumstances, the LST of barren land is higher than that of urban surface and green space (Haashemi et al., 2016), while the LST of the bare rock may be lower in Lhasa, which is located on the Tibetan Plateau, due to factors such as topography and altitude (Wen et al., 2017), thus the daytime $SUHII_2$ is overestimated. In the Northeast region, the rural land use types are all dominated by cropland and there is little difference between $SUHII_1$ and SUHII during the day. In Hong Kong and Taipei, the difference in vegetation activity led to an overestimation of daytime $SUHII_1$ quantified by evergreen broadleaf forests, while daytime $SUHII_2$ calculated with savanna was underestimated.

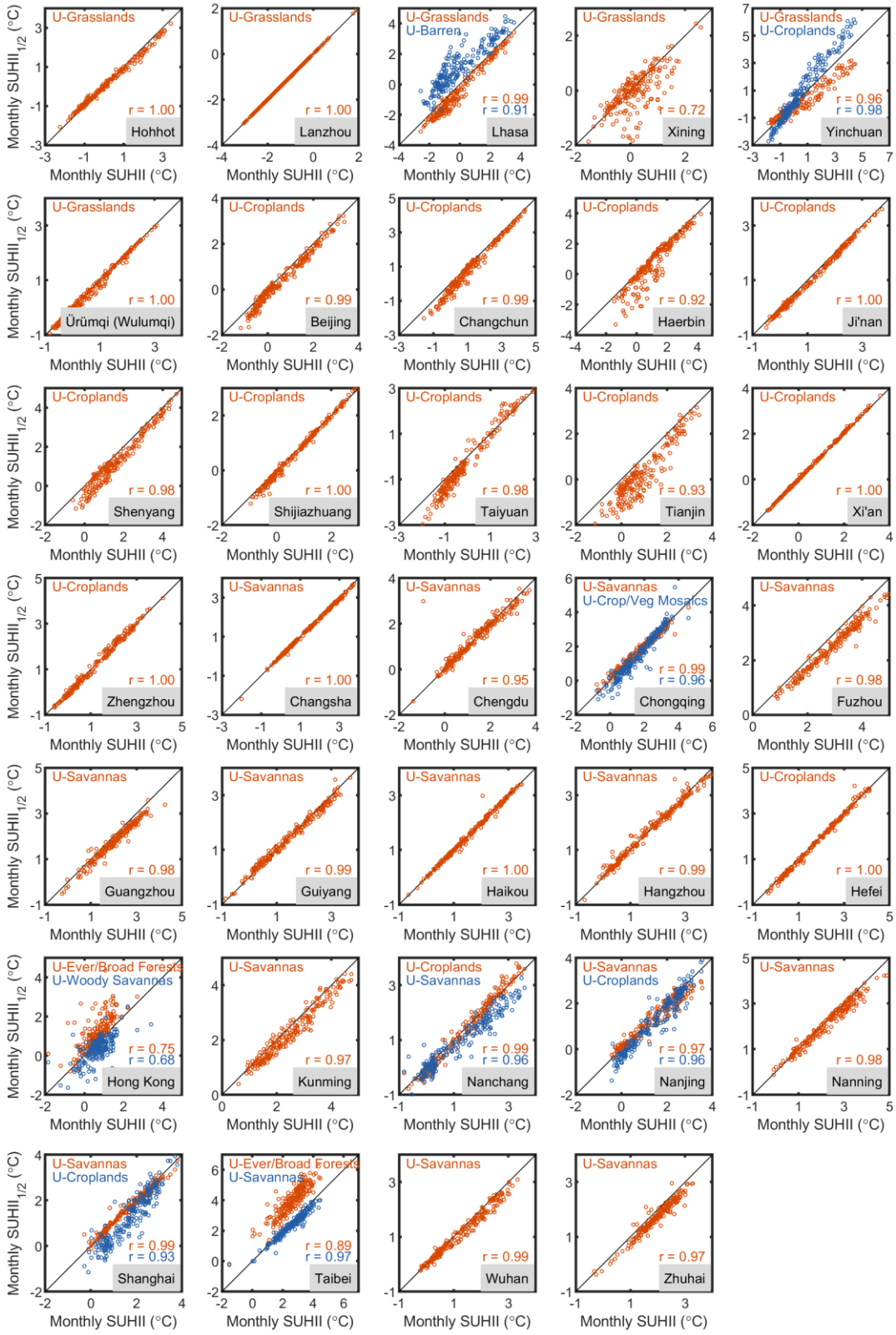

Figure 5.4 Comparison of monthly daytime SUHIIs quantified by multiple references.

At night, the influence of vegetation weakens, and factors such as precipitation and surface roughness affect the surface sensible heat flux and surface heat storage to regulate the LST. It can be seen from Figure 5.5 that the difference between $SUHII_1$ estimated by

grassland and SUHII in Lhasa is not obvious, while the $SUHII_2$ by barren land is obviously underestimated, mainly because the rough terrain of the bare rock surface in mountainous areas is more conducive to energy storage, so the lower higher nighttime LST leads to the lower $SUHII_2$. Ningxia is located in the arid area of the Northwest China, where the roughness of grassland is greater with higher aerodynamic resistance. Therefore, the LST of grassland at night is higher than that of cropland, which leads to overestimated $SUHII_2$ (Xie et al., 2011; Wen et al., 2017). In the Northeast region, the difference between nighttime $SUHII_1$ and SUHII is not evident. In the southeast region, the difference between $SUHII_1$ and $SUHII_2$ at nighttime in Hong Kong and Taipei is lower compared with that at daytime, which mainly due to the weakening of vegetation activities at night, and the reduced impact of evapotranspiration on rural LST. In Shanghai, the nighttime $SUHII_2$ quantified by cropland is obviously overestimated. Compared with savannas, it may be due to the higher roughness of the cropland and the larger aerodynamic impedance which reduces the sensible heat flux, thus the LST of the cropland at night is higher.

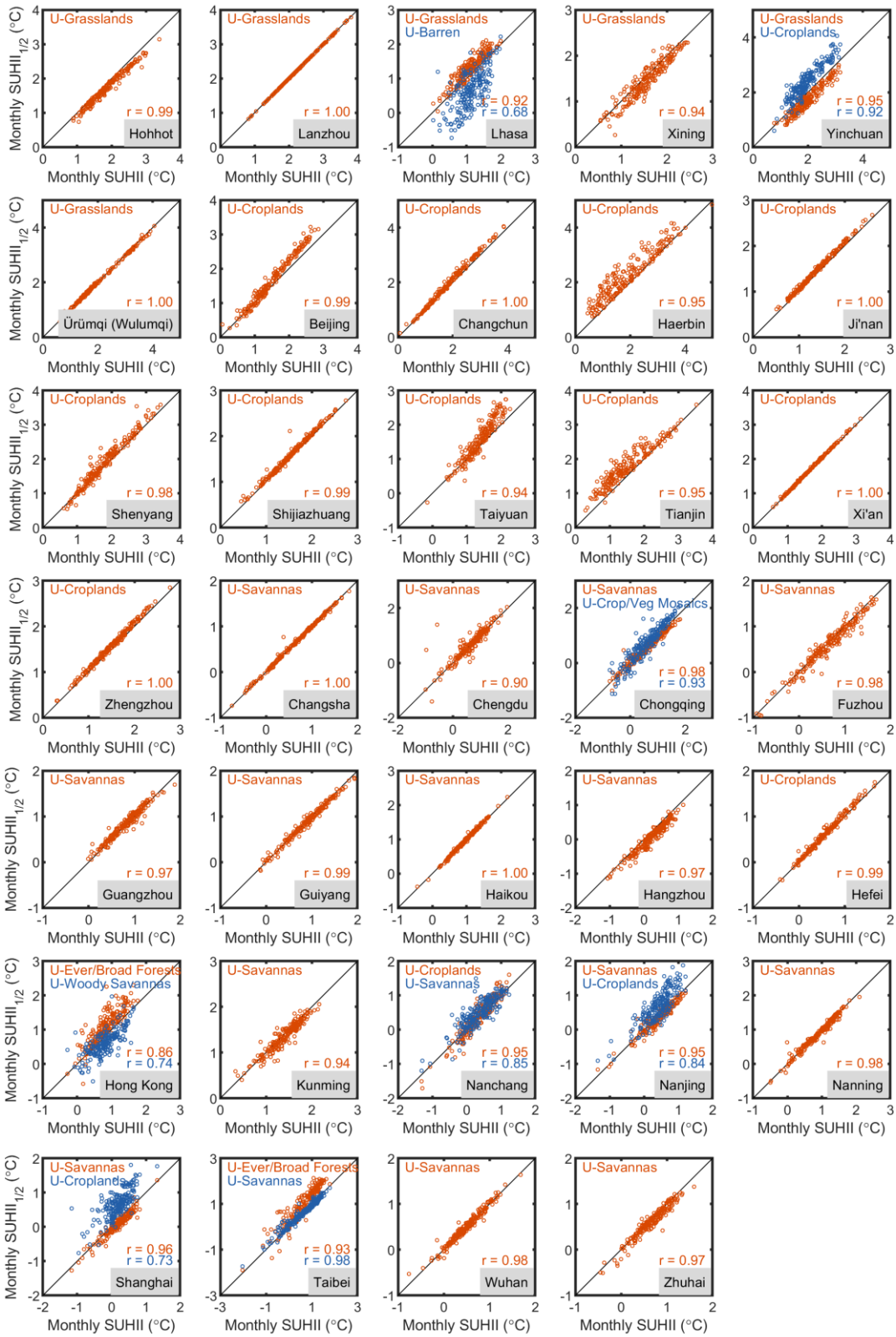

Figure 5.5 Comparison of monthly nighttime SUHIIs quantified by different references.

5.3.2. Comparison of interannual variation of monthly SUHIIs

From 2003 to 2019, the monthly average daytime and nighttime SUHII of each city was calculated separately, and cities with two components of principal rural land use types were picked out for comparison. The variation for different quantifications of daytime and nighttime SUHIIs are shown in Figure 5.6-Figure 5.9. Among them, the blue curve is the SUHII quantified by the whole rural LST, and the orange-red and yellow curves are the $SUHII_1$ and $SUHII_2$, respectively.

In the Northwest region, as shown in Figure 5.6, the $SUHII_1$ is underestimated and $SUHII_2$ is overestimated compared to SUHII, both at daytime and nighttime in Yinchuan; while the $SUHII_1$ is underestimated and $SUHII_2$ is overestimated at daytime for Lhasa, and the opposite occurs at night.

In the Southeast region in Figure 5.7, the daytime $SUHII_1$ calculated with the savanna and SUHII shows little difference, while the daytime $SUHII_2$ calculated with the cropland is underestimated for Nanjing, Nanchang and Shanghai in summer. As shown in Figure 5.8, the nighttime $SUHII_1$ is not obviously underestimated in Nanjing and Shanghai, while nighttime $SUHII_2$ is obviously overestimated in Nanjing, Shanghai and Chongqing.

In the southeastern region, as shown in Figure 5.9, Hong Kong and Taipei, with evergreen broadleaf forests as the first principal rural background and savanna as the second rural background, exhibit obvious overestimation of daytime $SUHII_1$, while there is an underestimation of daytime $SUHII_2$ that is more pronounced in summer. At nighttime, the $SUHII_1$ and $SUHII_2$ are not much different from SUHII in Hong Kong, while the $SUHII_1$ in Taipei is overestimated.

In addition, in the northwest, southeast, and northeast regions, the difference between $SUHII_1$ and $SUHII_2$ is slight in some cities with grassland, savanna, and cropland as the single rural land use type, which are not investigated in detail here.

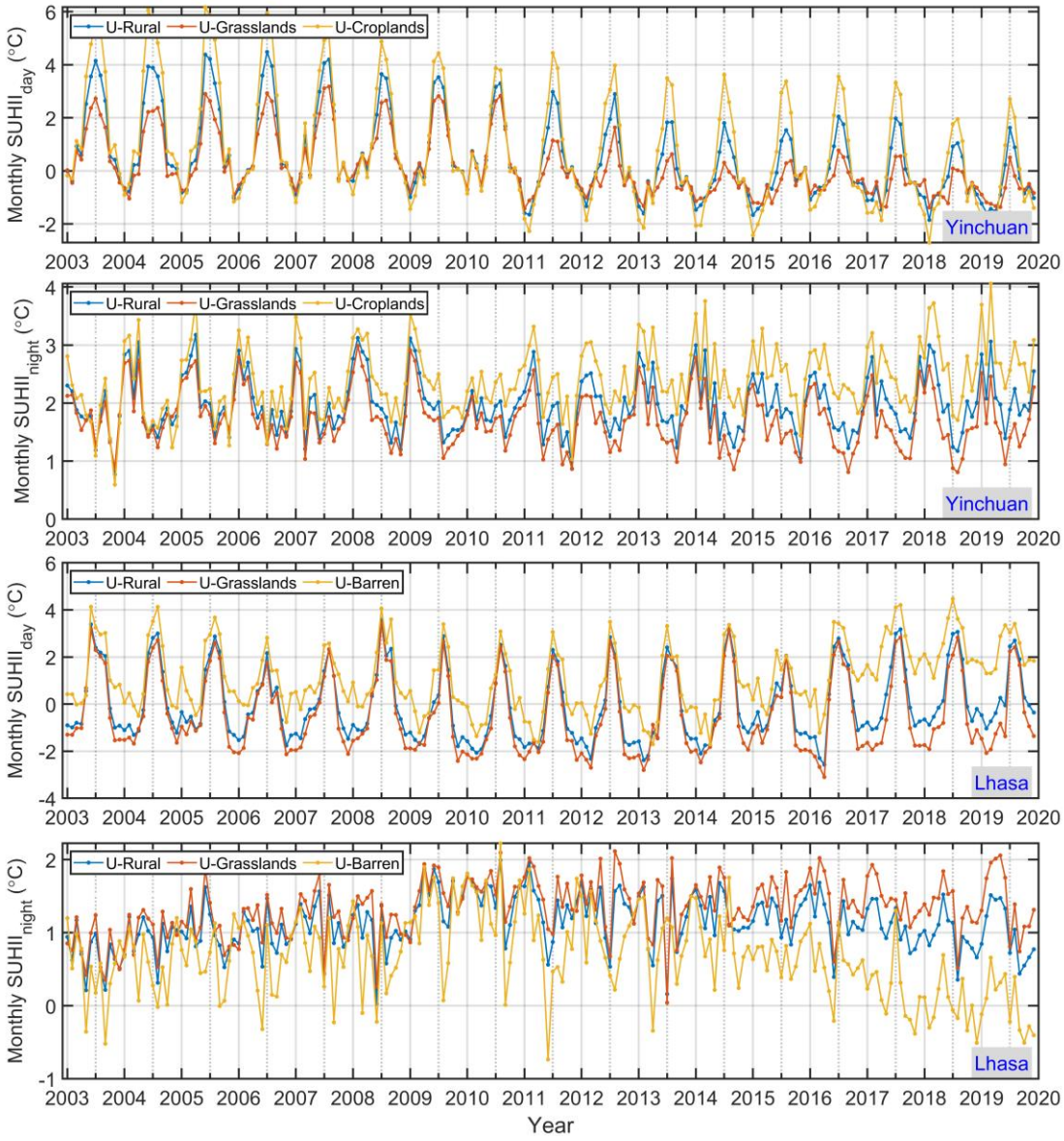

Figure 5.6 The long-term trend of monthly daytime and nighttime SUHIIs during 2003 and 2019 in several Northwest China cities (mainly grasslands, croplands and barren in rural).

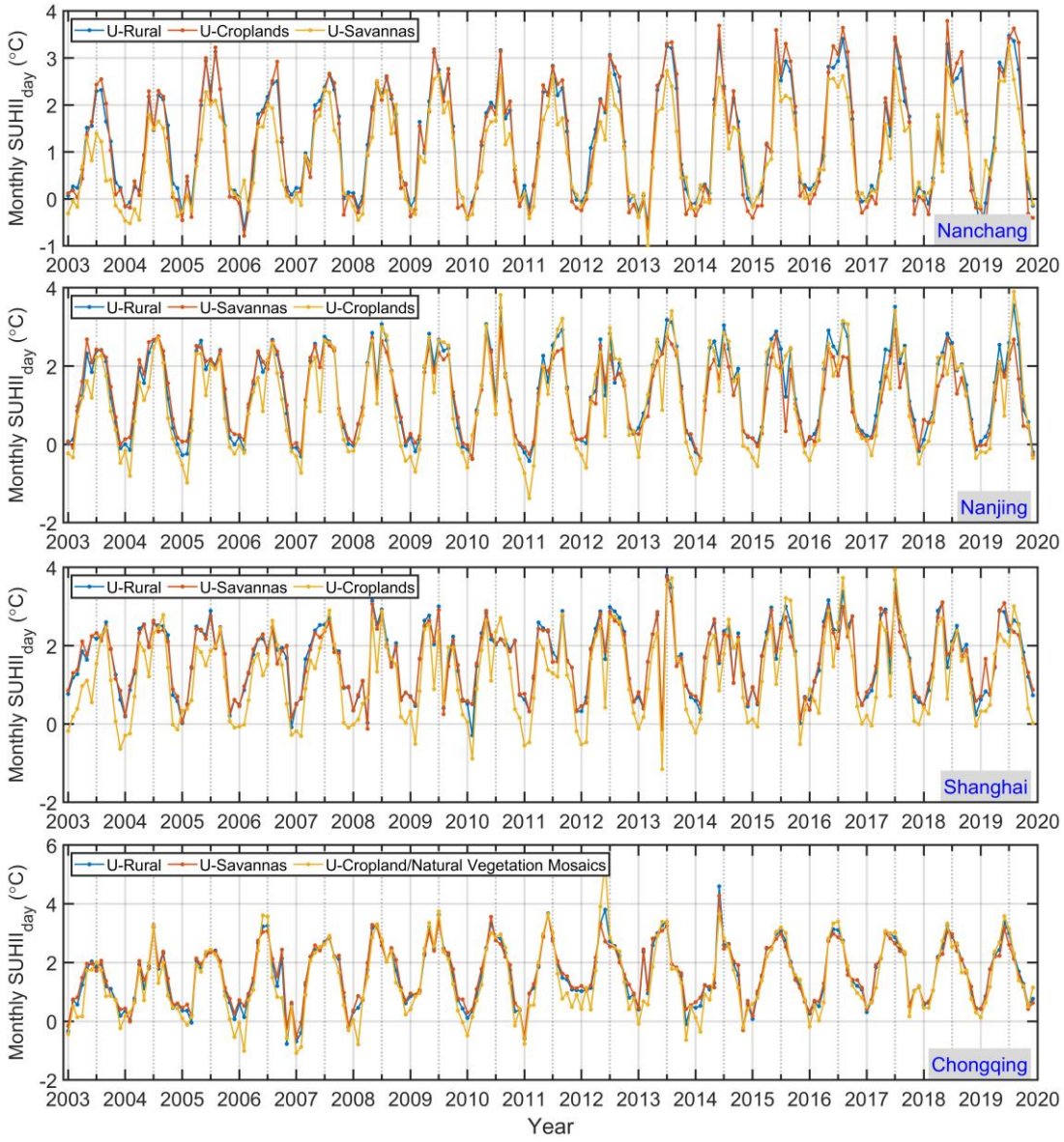

Figure 5.7 The long-term trend of monthly daytime SUHIIs during 2003 and 2019 in several Southeast China cities (mainly croplands and savannas in rural).

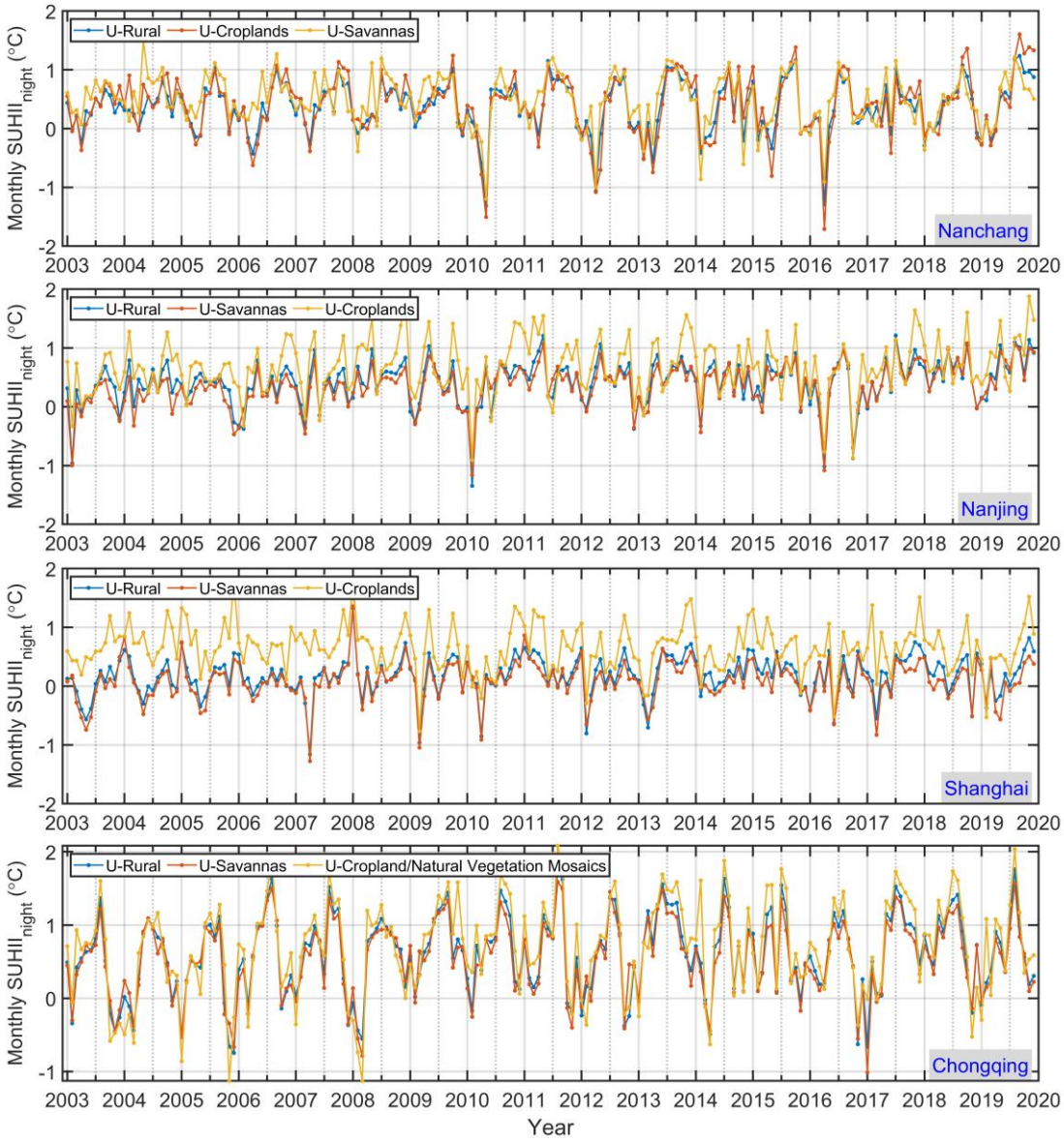

Figure 5.8 The long-term trend of monthly nighttime SUHIIs during 2003 and 2019 in several Southeast China cities (mainly croplands and savannas in rural).

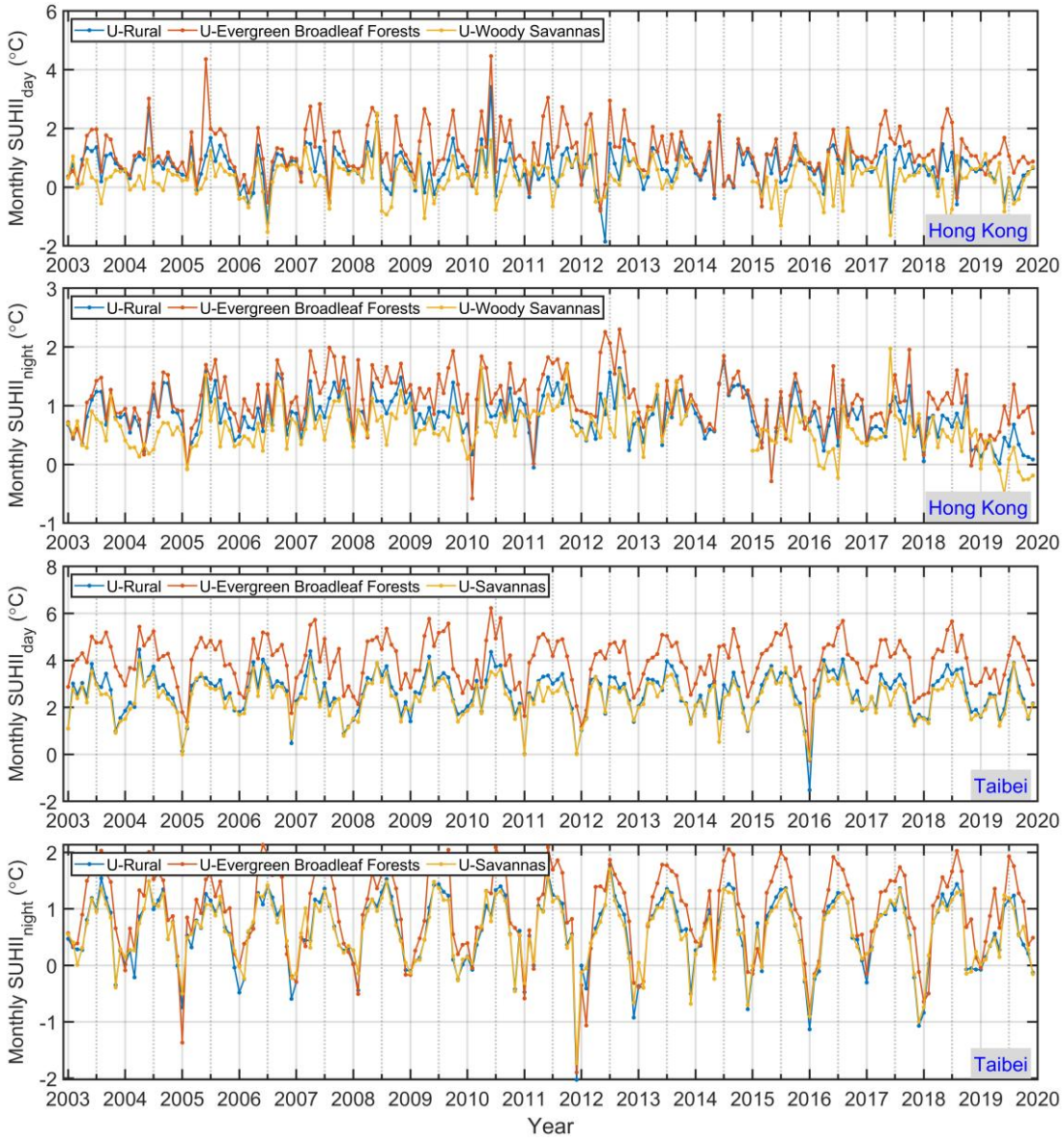

Figure 5.9 The long-term trend of monthly daytime and nighttime SUHIIs during 2003 and 2019 in several Southeast China cities (mainly evergreen broadleaf forests and savannas in rural).

5.4. Spatiotemporal patterns of SUHII in China

5.4.1. Day-night cycle

In order to explore the day-night cycle of SUHII in China's sub-regions, the SUHIIs obtained by Terra and Aqua at four times in a day were counted, and the SUHII of 34 cities were averaged from 2003 to 2019. Figure 5.10 shows the day-night cycle of annual, summer and winter averaged SUHII.

In summer, the day-night variations of SUHII in the Northeast, Southeast regions and the whole country are similar, reaching the maximum at 13:30, and the minimum at nighttime (01:30 or 22:30). The day-night variation of SUHII in the Northwest region is opposite to the former, which usually reaches its lowest value at 10:30, and increase gradually at nighttime, while the magnitude is lower than other regions. Since the cities in Northwest region is mostly located in arid zone, the pattern of day-night variation is similar to that in the global arid zone (Figure 3.21).

In winter, the day-night variation pattern of SUHII in the Southeast region is similar to that in summer, reaching a maximum at 13:30 and a minimum at night (01:30 or 22:30), while the absolute value of SUHII is lower than that in summer. The day-night cycle in the Northwest region also presents a similar pattern as in summer. It reaches the lowest value at 10:30 in the morning and gradually increases at night. In general, the daytime SUHII in the Northwest region is lower than that in summer, and negative value of cold islands appear. The day-night cycles of SUHII in the Northeast region are similar as the whole country, and are opposite to the variations in summer, reaching the minimum at noon (10:30 or 13:30), and gradually increasing at night (01:30 or 22:30). In Northeast region, the urban long-wave radiation at night is stronger due to serious pollution in winter, thus the nighttime SUHII is higher than during the day (Zhou et al., 2014a).

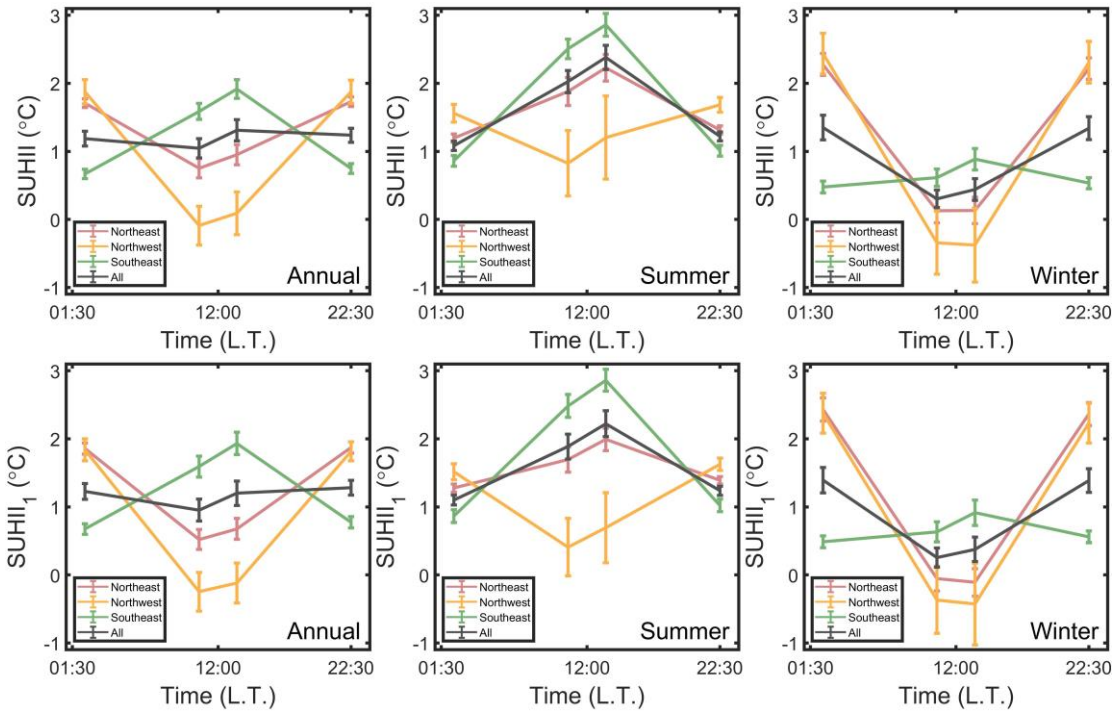

Figure 5.10 The day-night cycles of annual, summer and winter averaged SUHII and $SUHII_1$ for 34 China cities in different regions. The solid lines denote the mean values, the error bars represent its standard errors.

5.4.2. Monthly variation

Figure 5.11 shows the variation of monthly average SUHII in China. It can be seen that the seasonal variation of the daytime SUHII is more evident than that at night. During the daytime, the SUHII reaches its highest value in July (or August) and drops to its lowest value in December (or January) for the whole country.

At nighttime, the monthly variations of SUHII are not obvious in each area. In the autumn and winter, the nighttime SUHII in the Northeast and Northwest regions is higher than in the daytime, reaching the lowest value of the year in July and September, while the nighttime SUHII in the Southeast region is lower than that in the daytime during the year.

Comparing the upper and lower rows of and Figure 5.11, it can be seen that the pattern of monthly variations by $SUHII_1$ and SUHII are similar, indicating that in the regional-scale spatiotemporal analysis, the regional average SUHII quantified by the original "urban-rural temperature difference method" with whole rural reference is not affected by the

diversification of rural land use types, and can accurately reveal the spatiotemporal patterns of regional SUHII.

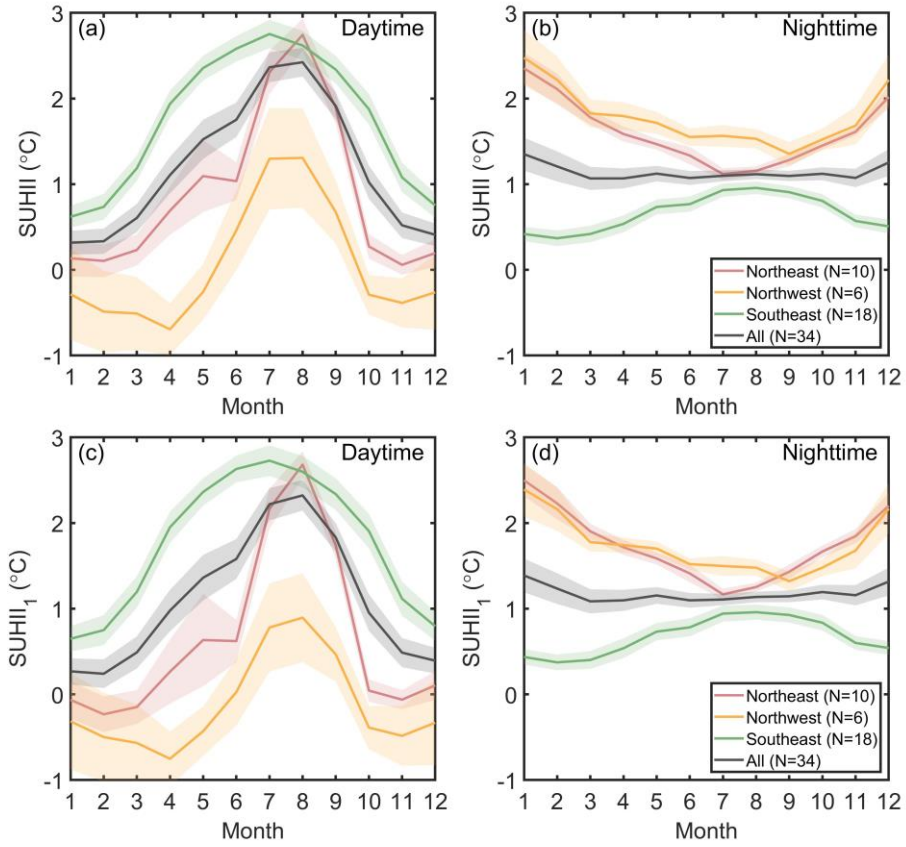

Figure 5.11 The variations of daytime and nighttime monthly SUHII (SUHII and SUHII1) for 34 China cities in different regions. The mean value is denoted in solid lines, and its standard errors are in shaded patch.

5.4.3. Interannual trend

From the foregoing analysis, the SUHII is not affected by the diversity of rural land use when reflecting the regional spatiotemporal laws. On the annual average, summer and winter average scales, the SUHII of 34 major cities in China were averaged to obtain the inter-annual variation of SUHII across the country and for each geographic region. The interannual trends for each geographical zones and the whole country are presented on the annual, summer and winter average scales, respectively, from Figure 5.12 to Figure 5.14. The MK test was used to determine whether there is a significant interannual trend, and then the Sen's slope was calculated.

As shown in Figure 5.12, on a national scale, the annual daytime SUHII presents no significant trend, while the annual nighttime SUHII shows a significant increasing trend (0.07 ℃/decade). In the Northeast and Northwest regions, the nighttime SUHII increased significantly with slopes of 0.14 ℃/decade and 0.10 ℃/decade, respectively, while the daytime SUHII decreased significantly during the day (-0.31 ℃/decade) in the Northwest region and increased significantly (0.24 ℃/decade) in the Southeast region.

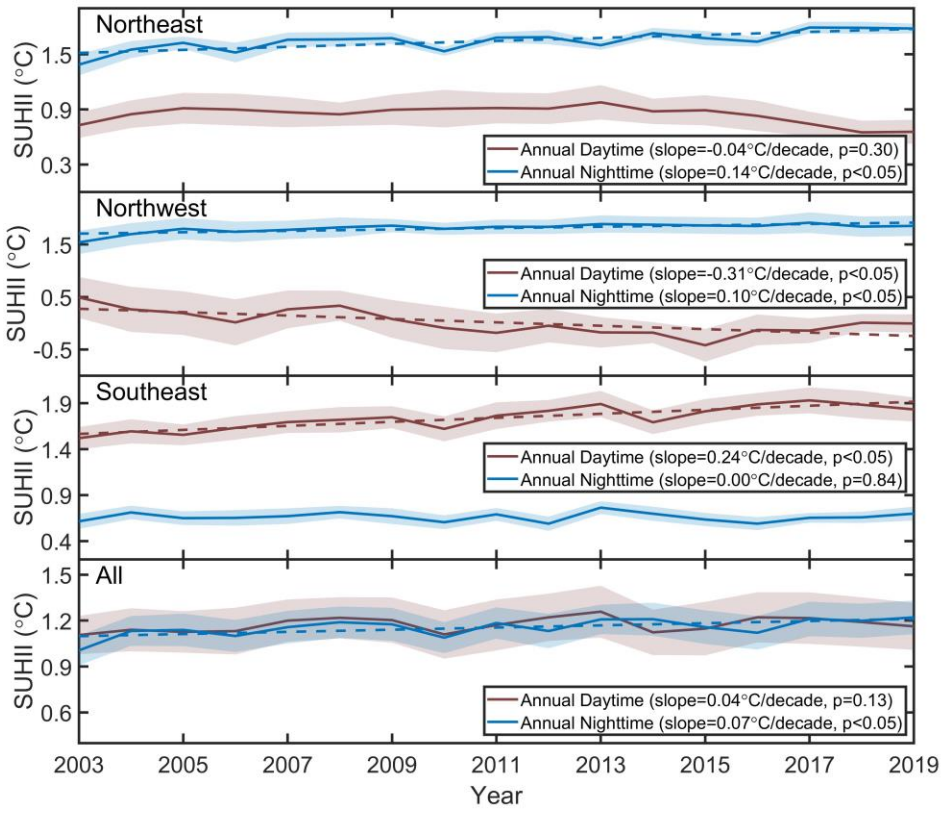

Figure 5.12 Inter-annual variations of annual daytime and nighttime SUHII for 34 China cities in different regions over the period 2003-2019. The solid line depicts the mean value of each year, and its standard errors are in shaded patch. The Sen's slope is calculated at 95% significant interval. The variations with significant trends are delineated in dashed line.

It can be seen from Figure 5.13 that on the summer scale, there is a significant increasing trend in daytime and nighttime SUHIIs with slopes of 0.11 ℃/decade and 0.10 ℃/decade, respectively, on a national scale. With respect to the inter-annual trends of daytime SUHI in each region, it decreased significantly in the Northwest region (-0.32 ℃/decade) and increased significantly in the Southeast region (0.29 ℃/decade). For

nighttime SUHII, it increases significantly for the Northeast and Southeast regions with slopes of 0.14 ℃/decade and 0.09 ℃/decade, respectively.

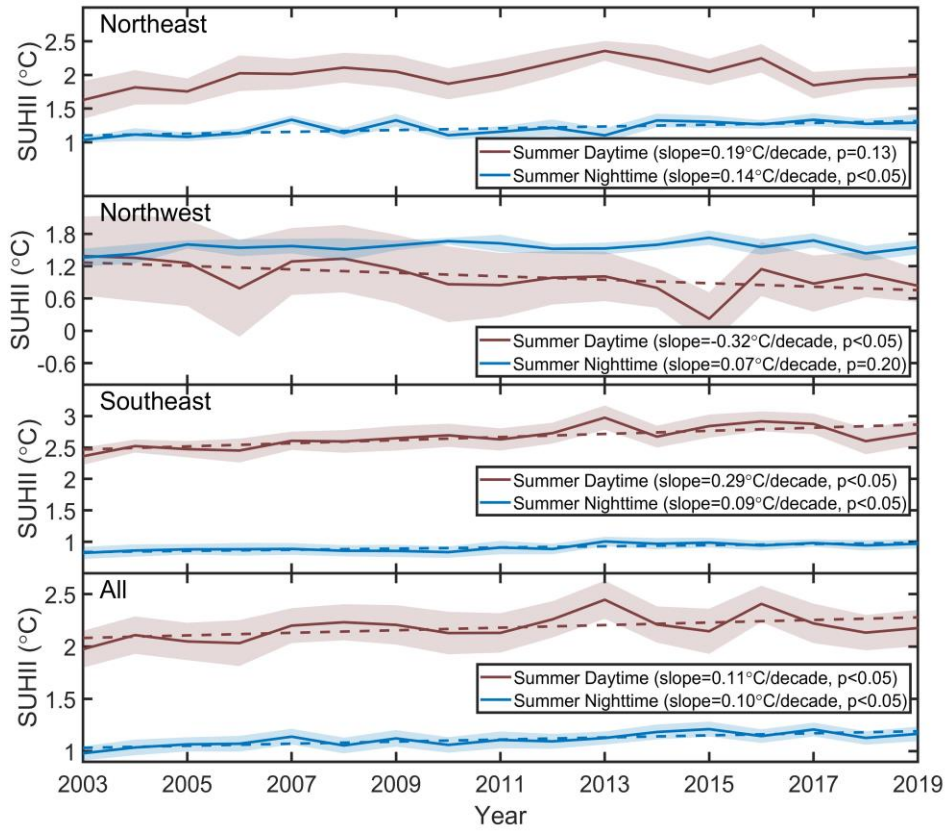

Figure 5.13 Inter-annual variations of summer daytime and nighttime SUHII for 34 China cities in different regions over the period 2003-2019. The solid line depicts the mean value of each year, and its standard errors are in shaded patch. The Sen's slope is calculated at 95% significant interval. The variations with significant trends are delineated in dashed line.

It can be seen from Figure 5.14 that for winter scale, there is no obvious change at daytime, while the nighttime SUHII increases significantly (0.08 ℃/decade) on the national scale. In the Northeast and Northwest regions, the daytime SUHII decrease significantly with slopes of -0.28 ℃/decade and -0.34 ℃/decade, respectively, while it increases significantly in the Southeast region (0.15 ℃/decade). For nighttime SUHII, it increases significantly for the Northeast and Northwest regions with slopes of 0.25 ℃/decade and 0.17 ℃/decade, respectively. There was no obvious trend for nighttime SUHII in the Southeast region.

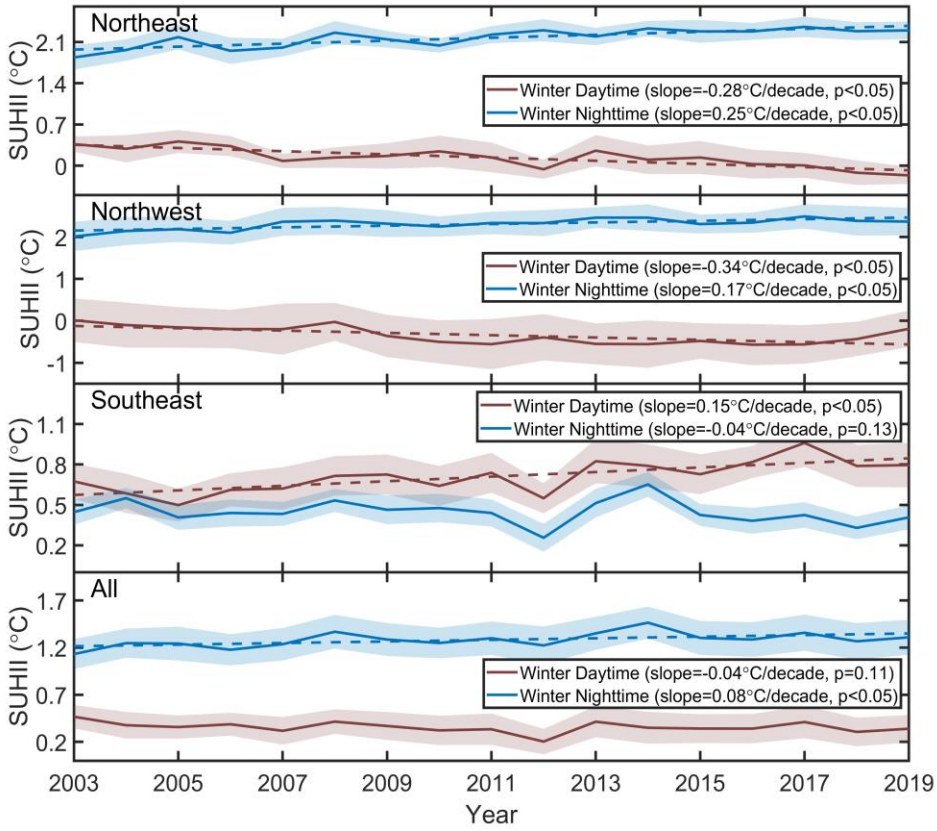

Figure 5.14 Inter-annual variations of winter daytime and nighttime SUHII for 34 China cities in different regions over the period 2003-2019. The solid line depicts the mean value of each year, and its standard errors are in shaded patch. The Sen's slope is calculated at 95% significant interval. The variations with significant trends are delineated in dashed line.

5.5. Conclusions

In this chapter, the urban form expansion and city size variation from 2003 to 2019 were analyzed for 34 major cities in China. Subsequently, the quantification of SUHII ($SUHII_1$ and $SUHII_2$) were constructed by differentiating the principal and second rural land use types. Afterwards, the new quantification methods were compared with original SUHII based on the entire rural background with respect to its monthly average value and interannual variation. Finally, the SUHII and $SUHII_1$ were further compared in terms of the day-night cycle, monthly variation and inter-annual trends across the country and in various geographic regions. Moreover, the spatiotemporal patterns of SUHII in China was investigated.

This chapter mainly draws the following conclusions:

(1) Among the 34 cities in China's provincial administrative units, with the exception of Lanzhou and Lhasa, significant urban expansion during 2003-2019 explained the necessity of defining the dynamic urban-rural extent in the quantification of SUHI.

(2) In the regional analysis of SUHI, the results quantified by the entire rural area are not affected by the diversity of rural land use when reflecting the regional spatiotemporal patterns which to a certain extent verified the credibility of the classical urban-rural LST difference method in the large-scale research for the spatiotemporal dynamic of SUHI.

(3) There are obvious seasonal and regional variations for the day-night cycle of SUHII in in China. In summer, SUHII reaches the highest value at noon and decreases at night, which is the opposite for the Northeast region; in winter, SUHII is lowest at noon and rises at night for most regions, while the Southeast region shows the opposite law.

(4) The monthly SUHII shows disparity with the day-night variation and regional contrast in China. The monthly variation of daytime SUHII is stronger than that at night. At daytime, the national average SUHII reaches its highest value in July (or August) and drops to its lowest value in December (or January)., which does not change significantly at nighttime for each geographical region.

(5) On a national scale, there is no significant trend for the annual daytime SUHII from 2003 to 2019, while the nighttime SUHII increase at the rate of 0.07 ℃/decade. Both the summer daytime and nighttime SUHII show a significant increase trend at the rate of 0.11 ℃/decade and 0.10 ℃/decade, respectively. There was a significant increasing trend (0.08 ℃/decade) for the winter nighttime SUHII. The seasonal and regional patterns of the inter-annual trends of SUHII vary across different regions.

6 Conclusions and perspectives

6.1. Conclusions

As one of the most severe urban thermal environmental problems, the UHI phenomenon in the field of academic research has been focused for decades. As an important branch of UHI study, the SUHI phenomenon based on remote sensing technology act as a bridge between the research of satellite product algorithm and urban remote sensing application. Firstly, in view of the deficiency of the global multi-scale and long-term SUHI research and the inconsistency of SUHI quantification methods, this study put forward the necessity of investigation on the spatiotemporal pattern of global SUHI and its driving factors. In this study, the global SUHII data set over 2003-2019 was generated to conduct comprehensive research. Secondly, the driving mechanism for the SUHI in different geographic regions and background climate regions are less concerned, which will provide target indication for the mitigation policies in urban management. Based on the surface energy balance model, the driving factor for global SUHI from the spatial and temporal perspectives, and the spatial non-stationarity were revealed. Finally, by constructing new quantitative indicators for the intensity of SUHI, the feasibility of the classic urban-rural temperature difference method concerning the whole rural reference in the regional study of SUHI was verified.

The main research work and conclusions of this paper are as follows:

(1) The spatiotemporal pattern of global SUHI in 1,711 major cities from 2003 to 2019

Based on the improved dynamic urban-extent scheme, the spatial and temporal characteristics of global SUHII in the past 17 years have been investigated with the existing global remote sensing data set and the GEE cloud computing platform. On the annual average, summer average, and winter average scales, the spatial patterns of global SUHII

are disclosed separately. According to the division of Köppen climate zone and latitude belts, the regional variation of global SUHI on different temporal scales is revealed. Moreover, the inter-annual trends of global SUHI are described.

The results have shown that the spatially averaged daytime and nighttime global SUHIIs are 0.97 °C and 0.94 °C, respectively. The SUHII quantified by DUE was generally higher than that by previous simplified urban-extent scheme. The global SUHI shows evident climatical and latitudinal zonal variations. The global summer day-night cycle was more evidently observed than that in winter, while daytime seasonality was more distinct than at nighttime. The regional patterns for annual trends, seasonality, and day-night cycle of SUHII were significantly different among climate zones. Further, warm temperate and snow zones showed distinct seasonal variations from summer to winter for daytime SUHII. Specifically, the SUHII in the arid zone with a negative daytime SUHII did not exhibit strong seasonality, but exhibited the highest day-night variability. Additionally, daytime SUHII indicated distinct latitudinal variations, and the flip-flop phenomenon generally originated from the arid and semi-arid zones. During 2003 and 2019, the daytime SUHII for annual (0.05 °C/decade) and summer (0.11 °C/decade) scales increased, whereas decreased (-0.03 °C/decade) in winter. At nighttime, only the summer SUHII increased obviously (0.02 °C/decade).

(2) The driving factors for global SUHI at multiple scales and the spatial non-stationarity

Based on the surface energy balance, the surface vegetation index, surface albedo, precipitation, wind speed, population density, and city size that affect the intensity of day and night heat islands were picked out to explore the impact on spatiotemporal pattern of global SUHI across cities in terms of the annual, summer, winter, monthly, and day-night scales. Furthermore, the drivers for the interannual trend of global SUHI was further analyzed across time from a temporal perspective. The fitting effects of multiple linear regression model, geographically weighted regression model and multi-scale geographically weighted regression model was compared to explored the contribution of

each factor to the SUHI from global to regional scale, meanwhile to investigate the spatial non-stationarity of multiple driving factors.

The results show that the ΔEVI is negatively correlated with daytime SUHII, which is mainly caused by the effect of vegetation activity on latent heat flux. The ΔWSA mainly regulates nighttime SUHII by affecting the net surface shortwave radiation during the day and the surface heat storage. The MAP is positively correlated with daytime SUHII, and negatively correlated with nighttime SUHII, which mainly affects the specific heat capacity, surface impedance and other parameters related to the surface heat flux in rural natural land surface, resulting in different rates of LST increase during the day and LST decrease at night to regulate the daytime and nighttime SUHII, The WS mainly presents a negative contribution to SUHII by disturbing the surface impedance and regulates the sensible heat flux. The positive correlation between the PD and UA with SUHII is more significant at nighttime, mainly due to the anthropogenic heat emissions to SUHII. The increasing long-term SUHII exhibits the most obvious correlations with the interannual decreasing of enhanced vegetation index difference between urban and rural at daytime, while the nighttime SUHIIs are dominated by the slope of surface property difference between urban and rural at nighttime. Under the combined effect of multiple factors, the driving mechanism of global SUHII are spatially non-stationary.

(3) Verification of the feasibility of the urban-rural LST difference method in the quantification of SUHII under diverse rural backgrounds

The 34 major cities in China were picked out as the research objects to analyze the dynamic of urban morphology and urban scale from 2003 to 2019, and the results show that cities other than Lanzhou and Lhasa have significant urban expansion, which explains the necessity of defining the dynamic urban-rural extent in the quantification of SUHII. Subsequently, new indices $SUHII_1$ and $SUHII_2$ for SUHII were proposed by differentiating the first principal and second components of rural land use types, respectively. Afterwards, the result from the new quantification was validated with the classical SUHII concerning the whole rural reference. Finally, the spatiotemporal patterns of SUHII in China was

investigated.

The results show that in most cities, the SUHIIs quantified by the entire rural area are differs slightly with the results of $SUHII_1$ and $SUHII_2$ except for certain cities with mixed rural land use types. With respect to different quantification results, the monthly variations of SUHII demonstrates slight disparity, indicating that the spatiotemporal pattern revealed by SUHII is not affected by the diversity of rural land use types, which verifies the feasibility of the urban-rural LST difference method in the classical quantification of SUHII for large-scale regional SUHI study. Finally, the obvious spatial and temporal contrast of SUHII concerning the day-night cycle, monthly variation, and interannual trends were discovered in 34 major cities in China.

6.2. Perspectives

Assessing the global SUHI dynamics and its driving factors through remote sensing technology have been topical issues since several decades. However, most studies used either fixed urban extent or limited land cover data of urban and rural regions that could cause imprecise SUHII calculations for long-term assessments. In this study, we identified the yearly dynamic urban and rural regions by an improved DUE scheme to maintain the consistency and reliability of long-term SUHII. To the best knowledge of the authors, this has not been implemented in previous large-scale SUHII studies. Comparison of our findings with those of previous studies indicated that different quantifications of urban and rural regions may affect the spatiotemporal SUHI patterns. This is an important consideration for global SUHI studies.

Our findings indicated that the magnitude and variations of SUHII exhibited regional contrasts and showed disparities from previous global studies. Apart from the key factors discussed in chapter 3.3.2, the percentage and weight of cities with positive and negative SUHII values can also lead to the offset between “heat island” and “cold island”. For better interpretation of the local phenomena, the positive and negative SUHIIs could be separately

investigated considering the potential differences in their spatiotemporal patterns in diverse contexts.

In this study, a preliminary attempt for the driving factors for the global long-term variation of SUHII across years was conducted. The analytical method from the temporal perspective was different from the previous studies, which executed the correlation analysis across space (cities) at global scale. The findings of global SUHI variation and associated factors were assumed to made some implications in urban planning. Furthermore, assessing the additional potential driving factors regarding anthropogenic activities (e.g., air pollution and human heat flux) and urban landscapes is necessary (Cao et al., 2016; Li et al., 2018; Liu and Weng, 2009; Lu and Weng, 2006; Weng and Lu, 2008; Huang and Wang, 2019).

Based on SEB, it can be found that differences in net surface radiation, surface latent heat and sensible heat flux between urban and rural areas are the direct causes of the SUHI phenomenon. Among them, the surface albedo indirectly affects SUHII by regulating the net surface shortwave radiation, while the surface vegetation, precipitation, wind speed and other hydrothermal factors contribute to SUHII by affecting the surface energy redistribution process. Due to the lack of global remote sensing products for the surface energy budget components with high precision, such as net surface short-wave radiation, surface latent heat and sensible heat flux, etc., the potential substitution factors are currently used to indirectly analyze the driving mechanism of SUHII. However, previous findings show that the influencing factors, such as surface albedo, cannot fully explain the mechanism on daytime SUHII from the perspective of energy balance. Therefore, in-depth analysis of the driving mechanism of global SUHII needs to be further investigated with sufficient and effective data source.

It should be noted that the SUHII was a clear-sky product, which inevitably caused errors in overlooking the cloudy sky LST pixels while interpreting SUHII. The SUHII derived from full LST coverage were to be further investigated with the development of global long-term all-sky LST products.

Related publications

Journal papers:

M. Si, Z.-L. Li, F. Nerry, Tang, B.-H. Tang, P. Leng, H., Wu, X. Zhang, and G. Shang. Spatiotemporal pattern and long-term trend of global surface urban heat islands characterized by dynamic urban-extent method and MODIS data. ISPRS Journal of Photogrammetry and Remote Sensing, 2022, 183: 321-335.

M. Si, B.-H. Tang, Z.-L. Li, F. Nerry, X. Zhang, and G. Shang. “An artificial neuron network with parameterization scheme for estimating net surface shortwave radiation from satellite data under clear sky--Application to simulated GF-5 data set,” IEEE Transactions on Geoscience and Remote Sensing, 2021, 59(5): 4262-4272.

Z.-L. Li, M. Si, P. Leng. “A review of remotely sensed surface urban heat islands from the fresh perspective of comparisons among different regions (Invited Review),” Progress In Electromagnetics Research C, 2020, 102: 31-46.

Conference proceedings:

M. Si, B.-H. Tang, R. Tang, H. Wu, Z.-L. Li, and G. Shang. “Estimation of net surface shortwave radiation from simulated Chinese Gaofen-5 satellite data,” 2019 IEEE International Geoscience and Remote Sensing Symposium, 2019: 1978-1981.

M. Si, B.-H. Tang, Z.-L. Li. “Estimation of land surface temperature from unmanned aerial vehicle loaded thermal imager data,” 2018 IEEE International Geoscience and Remote Sensing Symposium, 2018: 1210-1213.

References

Abatzoglou, J. T., Dobrowski, S. Z., Parks, S. A., and Hegewisch, K. C., 2018. TerraClimate, a high-resolution global dataset of monthly climate and climatic water balance from 1958–2015. Scientific data. 5, 170191.

Alin, A., 2010. Multicollinearity. Wiley Interdisciplinary Reviews: Computational Statistics. 2, 370-374.

Anniballe, R. and Bonafoni, S., 2015. A stable gaussian fitting procedure for the parameterization of remote sensed thermal images. Algorithms. 8, 82-91.

Arnfield, A. J., 2003. Two decades of urban climate research: a review of turbulence, exchanges of energy and water, and the urban heat island. Int J Climatol. 23, 1-26.

Bai, X., Dawson, R. J., Ürge-Vorsatz, D., Delgado, G. C., Salisu Barau, A., Dhakal, S., Dodman, D., Leonardsen, L., Masson-Delmotte, V., Roberts, D. C., and Schultz, S., 2018. Six research priorities for cities and climate change. Nature. 555, 23-25.

Brunsdon, C., Fotheringham, A. S., and Charlton, M. E., 1996. Geographically weighted regression: A method for exploring spatial nonstationarity. Geogr Anal. 28, 281-298.

Buyantuyev, A. and Wu, J. G., 2010. Urban heat islands and landscape heterogeneity: linking spatiotemporal variations in surface temperatures to land-cover and socioeconomic patterns. Landscape Ecol. 25, 17-33.

Cao, C., Lee, X., Liu, S., Schultz, N., Xiao, W., Zhang, M., and Zhao, L., 2016. Urban heat islands in China enhanced by haze pollution. Nat. Commun. 7, 1-7.

Chakraborty, T. and Lee, X., 2019. A simplified urban-extent algorithm to characterize surface urban heat islands on a global scale and examine vegetation control on their spatiotemporal variability. Int J Appl Earth Obs. 74, 269-280.

Chakraborty, T., Sarangi, C., and Tripathi, S. N., 2017. Understanding Diurnality and Inter-Seasonality of a Sub-tropical Urban Heat Island. Bound-Lay Meteorol. 163, 287-309.

Chakraborty, T., Hsu, A., Manya, D., and Sheriff, G., 2020. A spatially explicit surface urban heat island database for the United States: Characterization, uncertainties, and possible applications. ISPRS J Photogramm. 168, 74-88.

Chapman, S., Watson, J. E. M., Salazar, A., Thatcher, M., and McAlpine, C. A., 2017. The impact of urbanization and climate change on urban temperatures: a systematic review. Landscape Ecol. 32, 1921-1935.

Chen, L., Jiang, R., and Xiang, W. N., 2016. Surface heat island in Shanghai and its

relationship with urban development from 1989 to 2013. Adv Meteorol

Chen, X.-L., Zhao, H.-M., Li, P.-X., and Yin, Z.-Y., 2006. Remote sensing image-based analysis of the relationship between urban heat island and land use/cover changes. Remote Sens Environ. 104, 133-146.

Clinton, N. and Gong, P., 2013. MODIS detected surface urban heat islands and sinks: Global locations and controls. Remote Sens Environ. 134, 294-304.

Deilami, K. and Kamruzzaman, M., 2017. Modelling the urban heat island effect of smart growth policy scenarios in Brisbane. Land Use Policy. 64, 38-55.

Deilami, K., Kamruzzaman, M., and Liu, Y., 2018. Urban heat island effect: A systematic review of spatio-temporal factors, data, methods, and mitigation measures. Int J Appl Earth Obs. 67, 30-42.

Dissanayake, Morimoto, Ranagalage, and Murayama, 2019. Land-Use/Land-Cover Changes and Their Impact on Surface Urban Heat Islands: Case Study of Kandy City, Sri Lanka. Climate. 7, 99-99.

Dormann, C. F., Elith, J., Bacher, S., Buchmann, C., Carl, G., Carre, G., Marquez, J. R. G., Gruber, B., Lafourcade, B., Leitao, P. J., Munkemuller, T., McClean, C., Osborne, P. E., Reineking, B., Schroder, B., Skidmore, A. K., Zurell, D., and Lautenbach, S., 2013. Collinearity: a review of methods to deal with it and a simulation study evaluating their performance. Ecography. 36, 27-46.

Du, H., Wang, D., Wang, Y., Zhao, X., Qin, F., Jiang, H., and Cai, Y., 2016. Influences of land cover types, meteorological conditions, anthropogenic heat and urban area on surface urban heat island in the Yangtze River Delta Urban Agglomeration. Sci Total Environ. 571, 461-470.

Feranec, J., Kopecka, M., Szatmari, D., Holec, J., Stastny, P., Pazur, R., and Bobal'ova, H., 2019. A review of studies involving the effect of land cover and land use on the urban heat island phenomenon, assessed by means of the MUKLIMO model. Geografie. 124, 83-101.

Fernandes, R. and G. Leblanc, S., 2005. Parametric (modified least squares) and non-parametric (Theil–Sen) linear regressions for predicting biophysical parameters in the presence of measurement errors. Remote Sens Environ. 95, 303-316.

Fotheringham, A. S., Brunsdon, C., and Charlton, M.: Geographically weighted regression: the analysis of spatially varying relationships, John Wiley & Sons2003.

Fotheringham, A. S., Yang, W., and Kang, W., 2017. Multiscale geographically weighted regression (MGWR). Annals of the American Association of Geographers. 107, 1247-1265.

Fu, P. and Weng, Q., 2018. Variability in annual temperature cycle in the urban areas of the United States as revealed by MODIS imagery. ISPRS J Photogramm. 146, 65-73.

Gao, J., Huang, X., and Ni, M.: Spatio-temporal distribution of heat island effect in Lhasa and its response to land-use/cover in 2012-2016, 2018.

Grimm, N. B., Faeth, S. H., Golubiewski, N. E., Redman, C. L., Wu, J., Bai, X., and Briggs, J. M., 2008a. Global change and the ecology of cities. Science. 319, 756-760.

Grimm, N. B., Faeth, S. H., Golubiewski, N. E., Redman, C. L., Wu, J. G., Bai, X. M., and Briggs, J. M., 2008b. Global change and the ecology of cities. Science. 319, 756-760.

Haashemi, S., Weng, Q., Darvishi, A., and Alavipanah, S. K., 2016. Seasonal variations of the surface urban heat Island in a semi-arid city. Remote Sens. 8, 352.

Hamed, K. H., 2008. Trend detection in hydrologic data: the Mann–Kendall trend test under the scaling hypothesis. J. Hydrol. 349, 350-363.

He, B. J., 2018. Potentials of meteorological characteristics and synoptic conditions to mitigate urban heat island effects. Urban Clim. 24, 26-33.

Hu, Y., Hou, M., Jia, G., Zhao, C., Zhen, X., and Xu, Y., 2019. Comparison of surface and canopy urban heat islands within megacities of eastern China. ISPRS J Photogramm. 156, 160-168.

Huang, X. and Wang, Y., 2019. Investigating the effects of 3D urban morphology on the surface urban heat island effect in urban functional zones by using high-resolution remote sensing data: A case study of Wuhan, Central China. ISPRS J Photogramm. 152, 119-131.

Jin, K., Wang, F., Chen, D., Liu, H., Ding, W., and Shi, S., 2019. A new global gridded anthropogenic heat flux dataset with high spatial resolution and long-term time series. Scientific Data. 6, 139.

Jin, M. S., 2012. Developing an Index to Measure Urban Heat Island Effect Using Satellite Land Skin Temperature and Land Cover Observations. J Climate. 25, 6193-6201.

Kalnay, E. and Cai, M., 2003. Impact of urbanization and land-use. Nature. 425, 102-102.

Lai, J., Zhan, W., Huang, F., Quan, J., Hu, L., Gao, L., and Ju, W., 2018. Does quality control matter? Surface urban heat island intensity variations estimated by satellite-derived land surface temperature products. ISPRS J Photogramm. 139, 212-227.

Lai, J., Zhan, W., Quan, J., Bechtel, B., Wang, K., Zhou, J., Huang, F., Chakraborty, T., Liu, Z., and Lee, X., 2021. Statistical estimation of next-day nighttime surface urban heat islands. ISPRS J Photogramm. 176, 182-195.

Lazzarini, M., Marpu, P. R., and Ghedira, H., 2013. Temperature-land cover interactions: The inversion of urban heat island phenomenon in desert city areas. Remote Sens Environ. 130, 136-152.

Lee, X., Goulden, M. L., Hollinger, D. Y., Barr, A., Black, T. A., Bohrer, G., Bracho, R., Drake, B., Goldstein, A., Gu, L. H., Katul, G., Kolb, T., Law, B. E., Margolis, H., Meyers, T., Monson, R., Munger, W., Oren, R., Kyaw, T. P. U., Richardson, A. D., Schmid, H. P., Staebler, R., Wofsy, S., and Zhao, L., 2011. Observed increase in local cooling effect of deforestation at higher latitudes. Nature. 479, 384-387.

Li, D., Liao, W., Rigden, A. J., Liu, X., Wang, D., Malyshev, S., and Shevliakova, E., 2019. Urban heat island: Aerodynamics or imperviousness? Sci. Adv. 5, eaau4299.

Li, H., Meier, F., Lee, X., Chakraborty, T., Liu, J., Schaap, M., and Sodoudi, S., 2018. Interaction between urban heat island and urban pollution island during summer in Berlin. Sci Total Environ. 636, 818-828.

Li, L., Zha, Y., and Zhang, J., 2020a. Spatially non-stationary effect of underlying driving factors on surface urban heat islands in global major cities. Int J Appl Earth Obs. 90, 102131.

Li, L., Zha, Y., and Zhang, J., 2020b. Spatial and dynamic perspectives on surface urban heat island and their relationships with vegetation activity in Beijing, China, based on Moderate Resolution Imaging Spectroradiometer data. Int J Remote Sens. 41, 882-896.

Li, Z.-L., Si, M., and Leng, P., 2020c. A review of remotely sensed surface urban heat islands from the fresh perspective of comparisons among different regions (Invited Review). Prog. Electromagn. Res. C. 102, 31-46.

Liu, H. and Weng, Q., 2009. Scaling effect on the relationship between landscape pattern and land surface temperature. Photogramm. Eng. Remote Sens. 75, 291-304.

Liu, Y. S., 2018. Introduction to land use and rural sustainability in China. Land Use Policy. 74, 1-4.

Lu, D. and Weng, Q., 2006. Spectral mixture analysis of ASTER images for examining the relationship between urban thermal features and biophysical descriptors in Indianapolis, Indiana, USA. Remote Sens Environ. 104, 157-167.

Manoli, G., Fatichi, S., Schläpfer, M., Yu, K., Crowther, T. W., Meili, N., Burlando, P., Katul, G. G., and Bou-Zeid, E., 2019. Magnitude of urban heat islands largely explained by climate and population. Nature. 573, 55-60.

Martin-Vide, J., Sarricolea, P., and Moreno-García, M. C., 2015. On the definition of urban heat island intensity: the “rural” reference. Front. Earth Sci. 3, 24.

Meng, C. and Dou, Y., 2016. Quantifying the Anthropogenic Footprint in Eastern China. Sci Rep-Uk. 6

Mika, J., Forgo, P., Lakatos, L., Olah, A. B., Rapi, S., and Utasi, Z., 2018. Impact of 1.5 K global warming on urban air pollution and heat island with outlook on human health effects. Curr. Opin. Environ. Sustain. 30, 151-159.

Mohajerani, A., Bakaric, J., and Jeffrey-Bailey, T., 2017. The urban heat island effect, its causes, and mitigation, with reference to the thermal properties of asphalt concrete. J Environ Manage. 197, 522-538.

Mondal, A., Khare, D., and Kundu, S., 2015. Spatial and temporal analysis of rainfall and temperature trend of India. Theor Appl Climatol. 122, 143-158.

Moran, P. A., 1950. A test for the serial independence of residuals. Biometrika. 37, 178-181.

O'Loughlin, J., Witmer, F. D. W., Linke, A. M., Laing, A., Gettelman, A., and Dudhia, J., 2012. Climate variability and conflict risk in East Africa, 1990–2009. Proceedings of the National Academy of Sciences. 109, 18344.

Oke, T. R., 1982. The energetic basis of the urban heat island. Q. J. R. Meteorol. Soc. 108, 1-24.

Oshan, T. M., Li, Z., Kang, W., Wolf, L. J., and Fotheringham, A. S., 2019. mgwr: A Python implementation of multiscale geographically weighted regression for investigating process spatial heterogeneity and scale. Isprs Int J Geo-Inf. 8, 269.

Patz, J. A., Campbell-Lendrum, D., Holloway, T., and Foley, J. A., 2005. Impact of regional climate change on human health. Nature. 438, 310-317.

Pede, T. and Mountrakis, G., 2018. An empirical comparison of interpolation methods for MODIS 8-day land surface temperature composites across the conterminous Unites States. ISPRS J Photogramm. 142, 137-150.

Peng, J., Jia, J., Liu, Y., Li, H., and Wu, J., 2018a. Seasonal contrast of the dominant factors for spatial distribution of land surface temperature in urban areas. Remote Sens Environ. 215, 255-267.

Peng, J., Ma, J., Liu, Q., Liu, Y., Hu, Y. n., Li, Y., and Yue, Y., 2018b. Spatial-temporal change of land surface temperature across 285 cities in China: An urban-rural contrast perspective. Sci Total Environ. 635, 487-497.

Peng, S., Piao, S., Ciais, P., Friedlingstein, P., Ottle, C., Bréon, F.-M., Nan, H., Zhou, L., and Myneni, R. B., 2012. Surface Urban Heat Island Across 419 Global Big Cities. Environ. Sci. Technol. 46, 696-703.

Planque, C., Carrer, D., and Roujean, J.-L., 2017. Analysis of MODIS albedo changes over steady woody covers in France during the period of 2001–2013. Remote Sens Environ. 191, 13-29.

Quan, J., Chen, Y., Zhan, W., Wang, J., Voogt, J., and Wang, M., 2014. Multi-temporal trajectory of the urban heat island centroid in Beijing, China based on a Gaussian volume model. Remote Sens Environ. 149, 33-46.

Rajasekar, U. and Weng, Q., 2009. Urban heat island monitoring and analysis using a non-parametric model: A case study of Indianapolis. ISPRS J Photogramm. 64, 86-96.

Rasul, A., Balzter, H., Smith, C., Remedios, J., Adamu, B., Sobrino, J., Srivanit, M., and Weng, Q., 2017. A Review on Remote Sensing of Urban Heat and Cool Islands. Land. 6, 38-38.

Rozenfeld, H. D., Rybski, D., Andrade, J. S., Batty, M., Stanley, H. E., and Makse, H. A., 2008. Laws of population growth. Proc. Natl. Acad. Sci. U. S. A. 105, 18702-18707.

Rubel, F. and Kottek, M., 2010. Observed and projected climate shifts 1901-2100 depicted by world maps of the Köppen-Geiger climate classification. Meteorol Z. 19, 135-141.

Santamouris, M., 2015. Analyzing the heat island magnitude and characteristics in one hundred Asian and Australian cities and regions. Sci Total Environ. 512, 582-598.

Santamouris, M., Cartalis, C., Synnefa, A., and Kolokotsa, D., 2015. On the impact of urban heat island and global warming on the power demand and electricity consumption of buildings—A review. Energ Buildings. 98, 119-124.

Shepherd, J. M., 2005. A Review of Current Investigations of Urban-Induced Rainfall and Recommendations for the Future. Earth Interact. 9, 1-27.

Simwanda, M., Ranagalage, M., Estoque, R. C., and Murayama, Y., 2019. Spatial Analysis of Surface Urban Heat Islands in Four Rapidly Growing African Cities. Remote Sens. 11, 1645.

Song, W. and Deng, X. Z., 2017. Land-use/land-cover change and ecosystem service provision in China. Sci Total Environ. 576, 705-719.

Stewart, I. D. and Oke, T. R., 2012. Local climate zones for urban temperature studies. Bull. Am. Meteorol. Soc. 93, 1879-1900.

Sulla-Menashe, D. and Friedl, M. A., 2018. User guide to collection 6 MODIS land cover (MCD12Q1 and MCD12C1) product. USGS: Reston, VA, USA, 1-18.

Sun, R., Lü, Y., Yang, X., and Chen, L., 2019. Understanding the variability of urban heat islands from local background climate and urbanization. J Clean Prod. 208, 743-752.

Sun, Y., Wang, S., and Wang, Y., 2020. Estimating local-scale urban heat island intensity using nighttime light satellite imageries. Sustain Cities Soc. 57, 102125.

Sun, Y., Zhang, X., Ren, G., Zwiers, F. W., and Hu, T., 2016. Contribution of urbanization to warming in China. Nat. Clim. Change. 6, 706-709.

Thompson, J. A. and Paull, D. J., 2017. Assessing spatial and temporal patterns in land surface phenology for the Australian Alps (2000–2014). Remote Sens Environ. 199, 1-13.

Tran, H., Uchihama, D., Ochi, S., and Yasuoka, Y., 2006. Assessment with satellite data of the urban heat island effects in Asian mega cities. Int J Appl Earth Obs. 8, 34-48.

United Nations Department of Economic Social Affairs Population Division, World Urbanization Prospects (The 2018 Revision). New York, NY, USA, 197-236, https://population.un.org/wpp/Download/Standard/Population/.

Vitousek, P. M., Mooney, H. A., Lubchenco, J., and Melillo, J. M., 1997. Human domination of Earth's ecosystems. Science. 277, 494-499.

Wan, Z., 2008. New refinements and validation of the MODIS Land-Surface Temperature/Emissivity products. Remote Sens Environ. 112, 59-74.

Wang, W. and Shu, J., 2020. Urban renewal can mitigate urban heat islands. Geophys Res Lett. 47, e2019GL085948.

Wen, L., Peng, W., Yang, H., Wang, H., Dong, L., and Shang, X.: An analysis of land surface temperature (LST) and its influencing factors in summer in western Sichuan Plateau: A case study of Xichang City, 2017.

Weng, Q., 2001. A remote sensing-GIS evaluation of urban expansion and its impact on surface temperature in the Zhujiang Delta, China. Int J Remote Sens. 22, 1999-2014.

Weng, Q. and Lu, D., 2008. A sub-pixel analysis of urbanization effect on land surface temperature and its interplay with impervious surface and vegetation coverage in Indianapolis, United States. Int J Appl Earth Obs. 10, 68-83.

Weng, Q., Lu, D., and Schubring, J., 2004. Estimation of land surface temperature-vegetation abundance relationship for urban heat island studies. Remote Sens Environ. 89, 467-483.

Weng, Q., Firozjaei, M. K., Sedighi, A., Kiavarz, M., and Alavipanah, S. K., 2019. Statistical analysis of surface urban heat island intensity variations: A case study of babol city, iran. Gisci Remote Sens. 56, 576-604.

Wu, Z. and Ren, Y., 2019. A bibliometric review of past trends and future prospects in urban heat island research from 1990 to 2017. Environ. Rev. 27, 241-251.

Xie, M., Wang, Y., and Fu, M.: An Overview and Perspective about Causative Factors of Surface

Urban Heat Island Effects, 2011.

Yan, Z. W., Wang, J., Xia, J. J., and Feng, J. M., 2016. Review of recent studies of the climatic effects of urbanization in China. Adv. Clim. Chang. Res. 7, 154-168.

Yang, Q., Huang, X., and Li, J., 2017. Assessing the relationship between surface urban heat islands and landscape patterns across climatic zones in China. Sci Rep-Uk. 7, 1-11.

Yang, Q., Huang, X., and Tang, Q., 2019. The footprint of urban heat island effect in 302 Chinese cities: Temporal trends and associated factors. Sci Total Environ. 655, 652-662.

Yao, R., Wang, L., Huang, X., Niu, Y., Chen, Y., and Niu, Z., 2018a. The influence of different data and method on estimating the surface urban heat island intensity. Ecol Indic. 89

Yao, R., Wang, L., Huang, X., Niu, Z., Liu, F., and Wang, Q., 2017. Temporal trends of surface urban heat islands and associated determinants in major Chinese cities. Sci Total Environ. 609, 742-754.

Yao, R., Wang, L., Huang, X., Zhang, W., Li, J., and Niu, Z., 2018b. Interannual variations in surface urban heat island intensity and associated drivers in China. J Environ Manage. 222, 86-94.

Yao, R., Wang, L., Huang, X., Liu, Y., Niu, Z., Wang, S., and Wang, L., 2021. Long-term

trends of surface and canopy layer urban heat island intensity in 272 cities in the mainland of China. Sci Total Environ. 772, 145607.

Yu, Z., Yao, Y., Yang, G., Wang, X., and Vejre, H., 2019. Spatiotemporal patterns and characteristics of remotely sensed region heat islands during the rapid urbanization (1995–2015) of Southern China. Sci Total Environ. 674, 242-254.

Yue, W., Liu, X., Zhou, Y., and Liu, Y., 2019. Impacts of urban configuration on urban heat island: An empirical study in China mega-cities. Sci Total Environ. 671, 1036-1046.

Zhang, P., Imhoff, M. L., Wolfe, R. E., and Bounoua, L., 2010. Characterizing urban heat islands of global settlements using MODIS and nighttime lights products. Can J Remote Sens. 36, 185-196.

Zhao, L., 2018. Urban growth and climate adaptation. Nat. Clim. Change. 8, 1034-1034.

Zhao, L., Lee, X., Smith, R. B., and Oleson, K., 2014. Strong contributions of local background climate to urban heat islands. Nature. 511, 216-219.

Zhao, S., Liu, S., and Zhou, D., 2016a. Prevalent vegetation growth enhancement in urban environment. Proceedings of the National Academy of Sciences. 113, 6313.

Zhao, S., Zhou, D., and Liu, S., 2016b. Data concurrency is required for estimating urban heat island intensity. Environ Pollut. 208, 118-124.

Zhou, B., Rybski, D., and Kropp, J. P., 2013. On the statistics of urban heat island intensity. Geophys Res Lett. 40, 5486-5491.

Zhou, B., Rybski, D., and Kropp, J. P., 2017. The role of city size and urban form in the surface urban heat island. Sci Rep-Uk. 7, 1-9.

Zhou, D., Zhao, S., Zhang, L., and Liu, S., 2016a. Remotely sensed assessment of urbanization effects on vegetation phenology in China's 32 major cities. Remote Sens Environ. 176, 272-281.

Zhou, D., Zhao, S., Liu, S., Zhang, L., and Zhu, C., 2014a. Surface urban heat island in China's 32 major cities: Spatial patterns and drivers. Remote Sens Environ. 152, 51-61.

Zhou, D., Zhao, S., Zhang, L., Sun, G., and Liu, Y., 2015. The footprint of urban heat island effect in China. Sci Rep-Uk. 5, 2-12.

Zhou, D., Zhang, L., Hao, L., Sun, G., Liu, Y., and Zhu, C., 2016b. Spatiotemporal trends of urban heat island effect along the urban development intensity gradient in China. Sci Total Environ. 544, 617-626.

Zhou, D., Xiao, J., Bonafoni, S., Berger, C., Deilami, K., Zhou, Y., Frolking, S., Yao, R., Qiao, Z., and Sobrino, J. A., 2019. Satellite remote sensing of surface urban heat islands: Progress, challenges, and perspectives. Remote Sens. 11, 1-36.

Zhou, D. C., Zhang, L. X., Li, D., Huang, D. A., and Zhu, C., 2016c. Climate-vegetation

control on the diurnal and seasonal variations of surface urban heat islands in China. Environ Res Lett. 11, 074009.

Zhou, W., Qian, Y., Li, X., Li, W., and Han, L., 2014b. Relationships between land cover and the surface urban heat island: seasonal variability and effects of spatial and thematic resolution of land cover data on predicting land surface temperatures. Landscape Ecol. 29, 153-167.

Résumé des travaux en français

Etude globale des dynamiques spatio-temporelles et des facteurs déterminants des ilots de chaleur urbain

Doctorant : Menglin SI

Directeur de Thèse : Françoise NERRY

Laboratoire : Laboratoire des sciences de l'ingénieur, de l'informatique et de l'imagerie (ICube), UMR 7357, CNRS-Université de Strasbourg, 300 bd Sébastien Brant, CS 10413, F-67412 Illkirch Cedex, France

Etude globale des dynamiques spatio-temporelles et des facteurs déterminants des ilots de chaleur urbain

1. Introduction

1.1. Contexte

Depuis le début du 21e siècle, l'urbanisation rapide et les activités anthropiques qui y sont associées influencent régulièrement les propriétés de la surface du sol et les conditions climatiques urbaines, perturbant ainsi l'équilibre énergétique de surface (Grimm et al., 2008). Dans le contexte de l'accélération de l'urbanisation et du réchauffement climatique, l'effet d'îlot de chaleur urbain (ICU) est progressivement devenu un problème environnemental thermique urbain qui a été largement pris en compte par le monde scientifique de même que par l'ensemble de la société écivile. L'effet UHI peut menacer le développement durable de l'humanité ; il est donc urgent de caractériser scientifiquement les modèles d'UHI mondiaux dans un cadre de recherche systématique (Bai et al., 2018).

Avec le développement de la technologie de télédétection, de multiples études sur les modèles spatio-temporels, les mécanismes moteurs et les stratégies d'atténuation de l'UHI de surface (SUHI), allant de l'échelle locale, nationale et régionale à l'échelle mondiale, ont été rapportées sur la base de données satellitaires de température de surface terrestre (LST). Le phénomène SUHI dans les pays en développement ou développés d'Asie, d'Amérique du Nord et d'Europe a reçu le plus d'attention, tandis que celui des pays sous-développés d'Afrique, d'Amérique du Sud et d'Océanie, a rarement été étudié (Zhou et al., 2019). De plus, pour mieux comprendre la dynamique mondiale de la SUHI, il est nécessaire d'approfondir l'étude à long terme de la SUHI mondiale concernant le changement d'utilisation des terres (Chakraborty et Lee, 2019). En outre, les facteurs moteur de la SUHI à l'échelle mondiale ont été détectés de manière préliminaire, alors que leur variation spatiale est à peine détectée par les modèles statistiques traditionnels. La non-stationnarité spatiale des mécanismes moteurs doit être révélée plus avant grâce aux progrès de la technologie des statistiques spatiales. Du point de

vue temporel, les facteurs qui déterminent la tendance à long terme de la SUHI mondiale ne sont pas clairs. En général, l'intensité de la SUHI (SUHII) est quantifiée par la différence de LST dans les zones urbaines et rurales, dans lesquelles le type de terrain rural est déterminant pour le résultat de la quantification. L'effet de l'arrière-plan rural avec divers types de terres sur la méthode de la différence urbaine-rurale pour décrire le modèle spatial et temporel de la SUHII régionale est incertain.

1.2. Objectifs et structure de la thèse

Cette thèse est consacrée à l'étude des modèles spatio-temporels des îlots de chaleur urbains de surface mondiaux de 2003 à 2019 par un schéma amélioré d'étendue urbaine dynamique (DUE), puis à l'exploration des facteurs moteurs des variations spatiales et des tendances à long terme des SUHII, le but final étant d'améliorer la recherche systémique sur les SUHI mondiaux et de fournir des indications pour l'atténuation des SUHI dans la planification urbaine. Plus précisément, trois objectifs de recherche ont été définis dans cette thèse:

(1) Premièrement, une base de données mondiale à long terme sur les SUHII est construite pour analyser son modèle spatial et sa dynamique temporelle à plusieurs échelles.

(2) Deuxièmement, les facteurs potentiels d'entraînement sont utilisés pour analyser le mécanisme d'entraînement du SUHII global d'un point de vue spatial et temporel. Parallèlement, le modèle statistique spatial multi-échelle est adopté pour analyser quantitativement la non-stationnarité spatio-temporelle des facteurs multiples.

(3) Enfin, les indices permettant de quantifier le SUHI avec différents types d'utilisation des terres rurales doivent être construits afin de vérifier la faisabilité de la méthode de différence de température urbaine-rurale dans les études régionales du SUHI.

Pour atteindre les objectifs de recherche, le contenu principal de cette thèse est organisé en six chapitres comme suit.

Le chapitre 1 donne une brève introduction sur le contexte, les objectifs de la recherche et les objectifs de cette thèse.

Le chapitre 2 présente les informations sur la zone d'étude et les principales sources de données. Tout d'abord, les principes de détermination de la zone d'étude, le modèle spatial et la

taille de la population des villes cibles sont présentés. Ensuite, les données d'images de télédétection, les données météorologiques, les données démographiques, etc. impliquées dans cette étude sont décrites en détail.

Dans le chapitre 3, l'étendue urbaine et rurale annuelle des agglomérations urbaines mondiales a été identifiée sur la base de la méthode DUE améliorée. Les modèles spatiaux et temporels du SUHII mondial de 2003 à 2019 ont été présentés aux échelles annuelle, estivale, hivernale et mensuelle. Ensuite, les contrastes régionaux de SUHII ont été révélés avec les zones latitudinales et climatiques. Enfin, les tendances interannuelles du SUHII global sont montrés à différentes échelles temporelles.

Dans le chapitre 4, les facteurs en termes de propriétés de surface, de conditions climatiques et de processus d'urbanisation ont été sélectionnés comme facteurs potentiels de SUHII à l'échelle annuelle, estivale, hivernale et diurne. La contribution de plusieurs facteurs a été étudiée séparément du point de vue spatial et temporel. Sur la base du modèle de régression multi-échelle géographiquement pondéré, la non-stationnarité spatiale de ces facteurs sur SUHII a été étudiée.

Dans le chapitre 5, plusieurs grandes villes de Chine ont été choisies pour analyser les changements de leurs formes et de leurs échelles urbaines entre 2003 et 2019. Le SUHII a été quantifié par différents types d'utilisation des terres rurales afin de vérifier la faisabilité de la méthode de différence de température entre les zones urbaines et rurales. Enfin, l'analyse multi-échelle du SUHII dans les sous-régions de la Chine révèle que le SUHII quantifié avec l'ensemble du type d'utilisation des terres rurales n'est pas affecté par la diversité de l'utilisation des terres lors de l'exploration des modèles temporels et spatiaux régionaux.

Le chapitre 6 présente les conclusions et les perspectives de la thèse.

2. Zone d'étude et source de données

Dans l'étude du SUHI mondial, des grandes villes du monde entier sont choisies comme cible de la recherche en fonction de la taille de leur population. Les villes de plus de 300 000 habitants, qui connaissent une croissance démographique rapide et des problèmes

environnementaux progressifs, sont sélectionnées comme objets de cette étude. Les ensembles de données utilisés dans cette étude comprennent les données sur la population urbaine et la localisation géographique, les données du spectroradiomètre imageur à résolution modérée (MODIS), les ensembles de données de la grille mondiale de la population et d'autres données.

Les données relatives à la population et à la localisation géographique proviennent du dernier WUP (édition révisée de 2018) publié par la Division de la population du Département des affaires économiques et sociales des Nations unies (United-Nations, 2019). La température de la surface terrestre peut être extraite du produit LST (MOD11A1 et MOD11A1, version 6) avec une résolution spatiale de 1 km. Les types de couverture terrestre annuelle sont extraits du produit MODIS land cover type (MCD12Q1, Version 6). L'indice de végétation est extrait du produit d'indice de végétation (MOD13A2 et MYD13A2, version 6) avec une résolution spatiale de 1 km. Une résolution spatiale de 500 m à des intervalles de 16 jours. L'élévation de la surface est extraite du jeu de données GTOPO30 avec une résolution spatiale de 1km de l'US Geological Survey (USGS). Les éléments météorologiques sont extraits des jeux de données mensuelles sur le climat et le bilan hydrique des surfaces terrestres mondiales - TerraClimate avec une résolution spatiale de 2,5 minutes d'arc (~ 5 km). La densité de population provient de l'ensemble de données d'estimation de la densité de la grille de population de Gridded Population of the World (GPW, v4.11). La carte vectorielle des divisions administratives mondiales à tous les niveaux du GADM (https://gadm.org/data.html) et les divisions administratives de la Chine du Resource and Environmental Science Data Center de l'Académie chinoise des sciences (https://www.resdc.cn/data.aspx?DATAID=201) ont également été utilisées. En outre, la division de la zone climatique de Köppen provient d'une carte au format vectoriel (http://koeppen-geiger.vu-wien.ac.at/shifts.htm).

3. Dynamique spatio-temporelle des îlots de chaleur urbains de surface à l'échelle globale

Ce chapitre concerne principalement les recherches sur la dynamique spatio-temporelle des SUHI mondiaux dans les grandes villes. Tout d'abord, un schéma amélioré d'extension

urbaine dynamique (DUE) est utilisé pour identifier la région urbaine annuelle et la zone rurale correspondante de 2003 à 2019. Ensuite, sur la base de l'ensemble des données mondiales quotidiennes (jour/nuit) de LST de 2003 à 2019, la méthode de la différence de température entre les zones urbaines et rurales a été utilisée pour calculer le SUHII global. Le modèle spatio-temporel des SUHII à l'échelle mondiale, dans les zones climatiques et le long des variations latitudinales est présenté. La variation mensuelle et le cycle jour-nuit des SUHII sont également explorés par grandes zones climatiques. Enfin, les tendances interannuelles des SUHII mondiaux et régionaux sont révélées à l'échelle de la moyenne annuelle, de la moyenne estivale et de la moyenne hivernale. Le workflow pour calculer les SUHII quotidiens par DUE est présenté dans la figure 1.

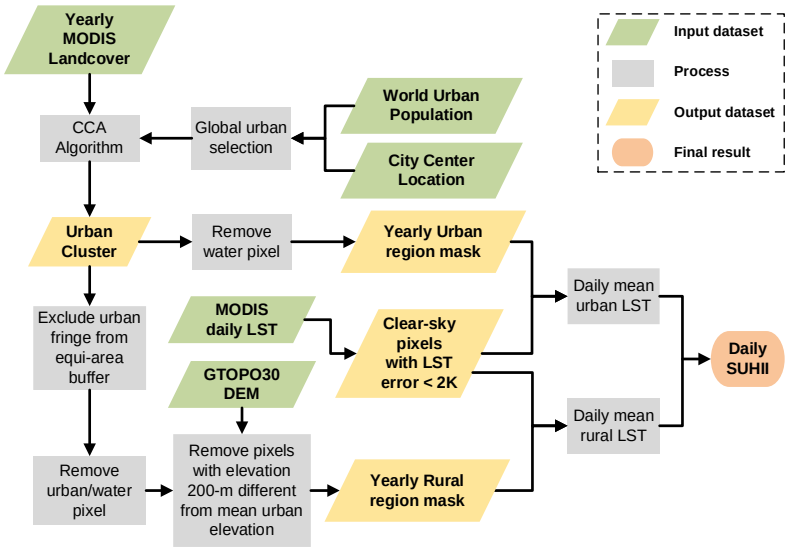

Figure 1. Workflow pour calculer le SUHII quotidien. Les parallélogrammes verts représentent les données d'entrée, les rectangles gris la procédure de traitement, les parallélogrammes jaunes les données de sortie et l'ellipse le résultat final.

La figure 2 présente un résumé des statistiques mondiales des moyennes temporelles des SUHII pendant la période 2003-2019 pour chaque ville à l'échelle annuelle, estivale et hivernale. Les valeurs moyennes mondiales des moyennes temporelles annuelles du SUHII diurne et du SUHII nocturne étaient respectivement de 0,97 °C et 0,94 °C.

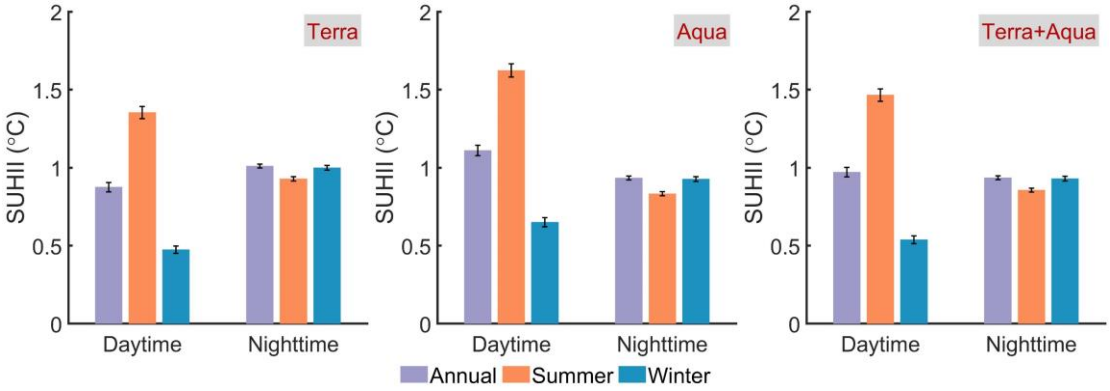

Figure 2. Résumé des valeurs moyennes globales et des erreurs standard des SUHIIs à moyenne temporelle pour chaque ville. Les barres de couleur représentent les valeurs moyennes de 1711 SUHIIs à moyenne temporelle. Les barres d'erreur indiquent les erreurs standard des valeurs moyennes.

La figure 3 présente les statistiques régionales des SUHII mondiaux par rapport aux quatre principales zones climatiques (équatoriale, aride, tempérée chaude et neige) accompagnées de la moyenne mondiale. Globalement, le SUHII diurne était positif dans toutes les zones climatiques, à l'exception de la zone aride, qui est généralement devenue positive la nuit. Néanmoins, les SUHII diurnes et nocturnes dans la zone aride ont démontré une valeur positive dans des études précédentes.

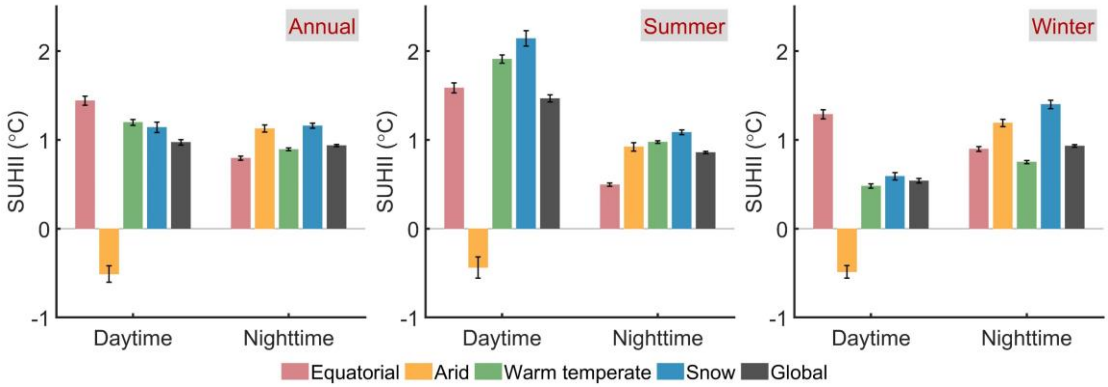

Figure 3. SUHII global pour les différentes zones climatiques. Les colonnes de couleur indiquent les valeurs moyennes, tandis que les barres d'erreur indiquent les erreurs standard.

La figure 4 présente les variations du SUHII global à pour chaque ceinture latitudinale. À l'échelle annuelle, les variations du SUHI dans les ceintures latitudinales sont plus évidentes pendant la journée. Le contraste jour-nuit est inversé (flip-flop) au-delà de ces régions, qui sont

principalement distribuées dans les villes arides et semi-arides. En été, les variations diurnes et nocturnes ont fluctué de manière plus significative qu'en hiver, alors qu'aucune inversion diurne n'a été observée le long des ceintures latitudinales.

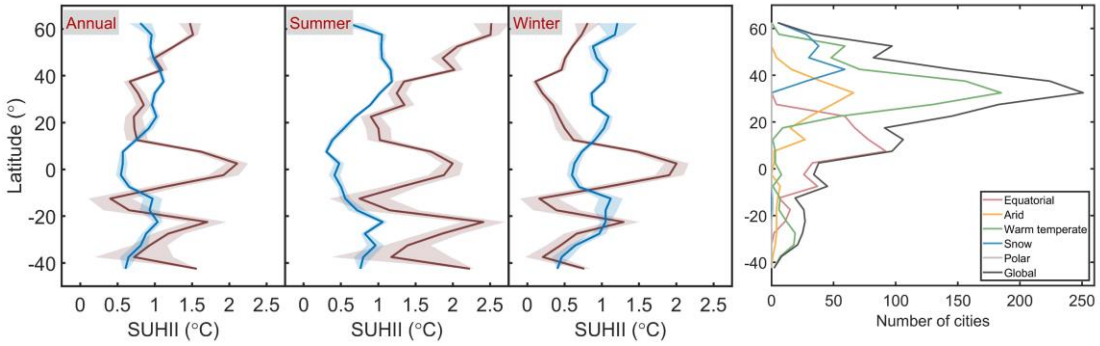

Figure 4. Variations latitudinales du SUHII global à un intervalle de 5 °. Les valeurs moyennes sont indiquées par des lignes pleines, leurs erreurs standard sont présentées dans des zones ombrées. Les courbes rouges et bleues représentent les SUHII diurnes et nocturnes, respectivement.

La figure 5 illustre les variations interannuelles de la moyenne mondiale du SUHII pour les 1711 villes. De jour, le SUHII a augmenté significativement en moyenne annuelle (0,15 °C/décennie) et en été (0,11 °C/décennie), alors qu'il a diminué (-0,03 °C/décennie) en hiver. Aucune tendance interannuelle significative n'a été observée pour le SUHII de nuit, sauf en été (0,02 °C/décennie).

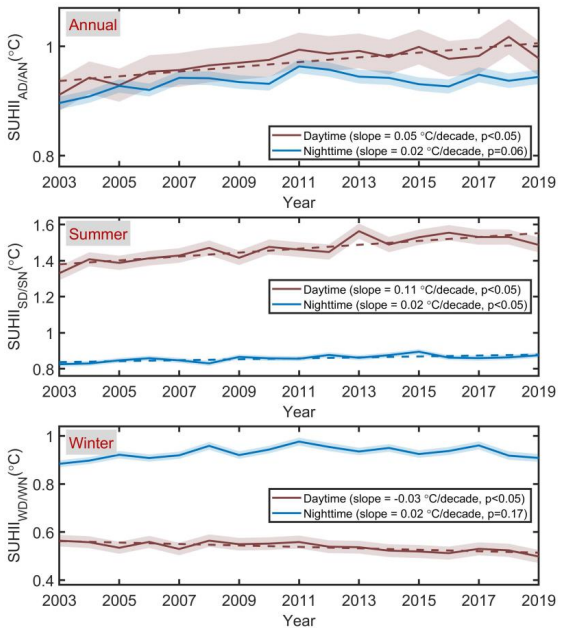

Figure 5. Variations interannuelles de la moyenne globale du SUHII pour 1711 villes pendant la période 2003-2019. La ligne continue et la zone ombrée représentent la valeur moyenne et ses erreurs standard. La pente de Sen a été calculée à un intervalle de signification de 95 %. Les variations avec des tendances significatives sont indiquées par une ligne en pointillés.

4. Facteurs déterminants à l'échelle globale des îlots de chaleur urbains de surface

Ce chapitre explore principalement les facteurs moteurs de SUHI concernant les propriétés de surface, les conditions climatiques et le processus d'urbanisation. Plus précisément, les facteurs potentiels de SUHII sont explorés d'un point de vue spatial. De plus, les facteurs des tendances interannuelles des SUHII sont étudiés d'un point de vue temporel. Par la suite, la non-stationnarité spatiale de chaque facteur est pleinement explorée par des modèles statistiques spatiaux avancés.

Une analyse de corrélation de Pearson entre les SUHII et les indices pertinents est effectuée pour identifier ces facteurs. Les coefficients de Pearson entre chaque facteur et les SUHII annuels diurnes et nocturnes sont présentés dans la figure 6. La distribution spatiale des coefficients de régression de chaque facteur de conduite obtenus à partir du modèle MGWR correspondant au SUHII annuel diurne est présentée dans la Figure 7. On peut constater que la contribution de multiples facteurs est spatialement non stationnaire à l'échelle mondiale. En général, les résultats du modèle MGWR avec la méthode de régression locale à largeur de bande variable permettent une estimation optimale du coefficient de contribution par rapport au modèle GWR.

La régression linéaire multiple par étapes entre la pente du SUHII et la pente des facteurs associés est effectuée et les coefficients et la contribution des principaux facteurs moteurs sont donnés dans le tableau 1. L'état interannuel de la végétation (ΔEVI) présente les corrélations négatives les plus évidentes avec le SUHII diurne à long terme, avec des taux de contribution de 34 %, 54 % et 38 % aux échelles annuelle, estivale et hivernale, respectivement. La pente de l'albédo de surface (ΔWSA), qui fait référence aux propriétés de surface, contribue

principalement de manière négative à la pente du SUHII nocturne, avec des contributions de 17 %, 33 % et 22 % aux échelles annuelle, estivale et hivernale, respectivement. Cela implique que les propriétés de surface vulnérables aux changements d'utilisation et de couverture des sols, la verdure dans les zones urbaines et les activités humaines doivent être prises en compte spécifiquement dans l'atténuation de la SUHI.

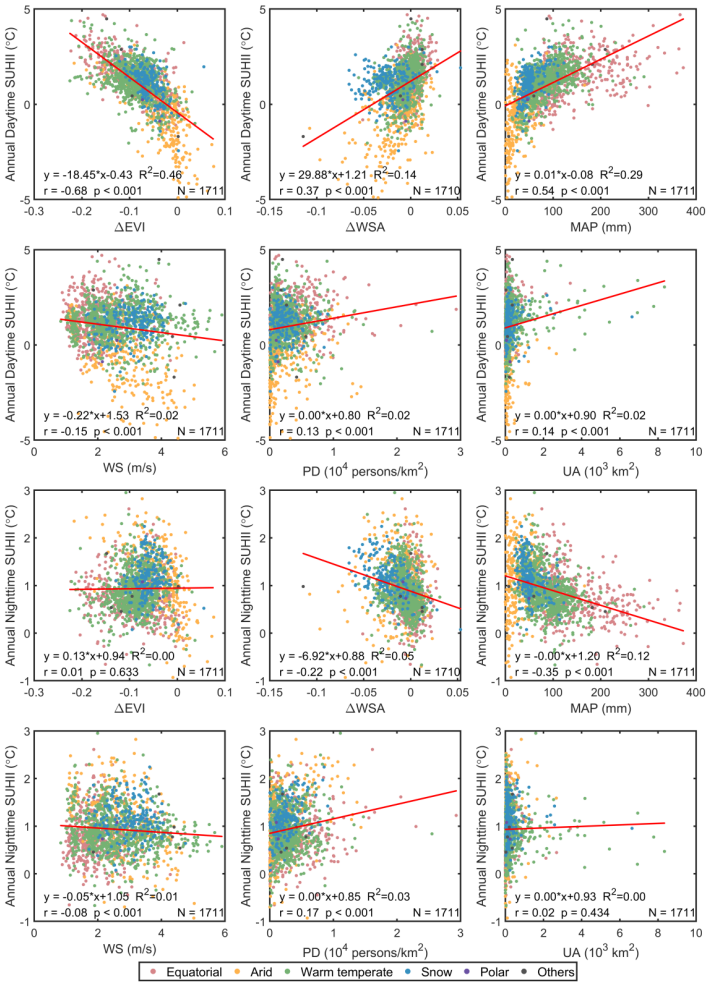

Figure 6. Corrélation de Pearson entre les SUHII mondiales annuelles diurnes et nocturnes et les facteurs moteurs associés. La formule représente l'équation de régression linéaire (r : coefficient de corrélation de Pearson, p : signification). EVI : indice de végétation amélioré, WSA : albédo du ciel blanc, MAP : précipitations moyennes, WS : vitesse du vent, PD : densité de population, UA : zone urbaine.

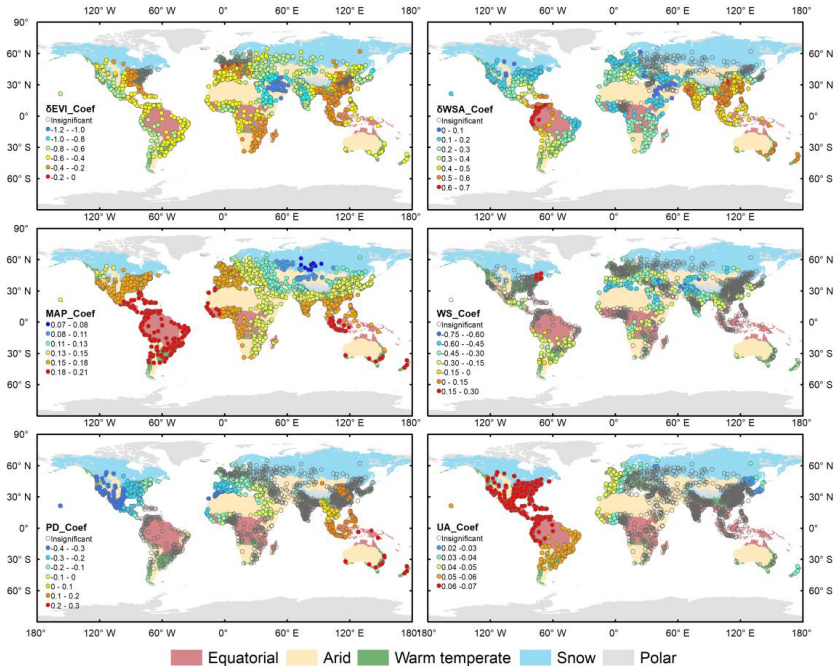

Figure 7. Variation spatiale des coefficients des multi indépendants pour le SUHII annuel de jour.

Table 1. Coefficients et la contribution (R2, %) de chaque facteur d'entraînement à la pente du SUHII mondial en 2003 et 2019.

	Coefficients et R^2 (%)					
	Annuel		Eté		Hiver	
	jour	nuit	jour	nuit	jour	nuit
Intercept	-0.01	0.00	-0.02	-0.01	-0.02	0.01
ΔEVI_{slope}	-18.45**	-2.54*	-27.43**	-4.25*	-14.82**	-
(R^2)	**(33.69)**	(2.14)	**(54.07)**	(5.86)	**(37.78)**	(-)
ΔWSA_{slope}	11.55**	-14.05**	14.23*	-18.06**	-	-14.72**
(R^2)	(3.01)	**(17.43)**	(2.06)	**(32.79)**	(-)	**(21.79)**

(**: p<0.01, *: p<0.05)

5. Quantification des îlots de chaleur urbains de surface sous de multiples types d'utilisation des terres rurales

Afin de vérifier la crédibilité de la méthode de quantification et d'exclure l'impact de la diversité des types d'utilisation des terres rurales sur le SUHII, ce chapitre sélectionne 34 grandes villes de Chine comme zone d'étude. Tout d'abord, la composition et la composante principale des différents types d'utilisation des terres rurales pour chaque ville sont explorées. Ensuite, de nouveaux calculs du SUHII sont proposés sur la base de types d'utilisation des sols uniques ou multiples dans les zones rurales. Ensuite, afin de vérifier la faisabilité et la crédibilité de la méthode de la différence urbaine-rurale dans la description du modèle régional et de la variation temporelle du SUHII régional, l'intégration spatiale et la variation temporelle du SUHII provenant de différentes méthodes quantitatives sont comparées au sein de chaque division géographique. Enfin, une analyse comparative multi-échelle de la SUHII dans différentes régions géographiques de la Chine est effectuée sur le cycle jour-nuit, la moyenne mensuelle et la variation interannuelle.

Contrairement à la méthode précédente de détermination de la LST moyenne sur l'ensemble de la surface rurale, les pixels LST ruraux valides pour le principal et le second type d'utilisation des terres rurales sont sélectionnés pour calculer la LST de référence correspondante, respectivement, et les nouvelles quantifications du SUHII sont présentées dans les équations (1) et (2) comme suit :

$$SUHII_1 = T_u - T_{r1} \tag{1}$$

$$SUHII_2 = T_u - T_{r2} \tag{2}$$

où T_u est la LST urbaine moyenne, T_{r1} et T_{r2} sont la LST moyenne des principaux et seconds types d'utilisation des terres rurales, respectivement, et $SUHII_1$ et $SUHII_2$ sont l'intensité correspondante de SUHI. Par la suite, le SUHII indique la quantification originale de l'intensité du SUHI par l'ensemble de la LST rurale.

La figure 8 montre le cycle jour-nuit de la moyenne annuelle, estivale et hivernale du SUHII. La figure 9 montre la variation de la moyenne mensuelle du SUHII en Chine. On peut voir que le modèle du cycle jour-nuit et les variations mensuelles de SUHII1 et SUHII sont similaires, ce qui indique que dans l'analyse spatio-temporelle à l'échelle régionale, la moyenne

régionale de SUHII quantifiée par la "méthode originale de différence de température urbaine-rurale" avec une référence rurale entière n'est pas affectée par la diversification des types d'utilisation des terres rurales, et peut révéler avec précision les modèles spatio-temporels de SUHII régionale.

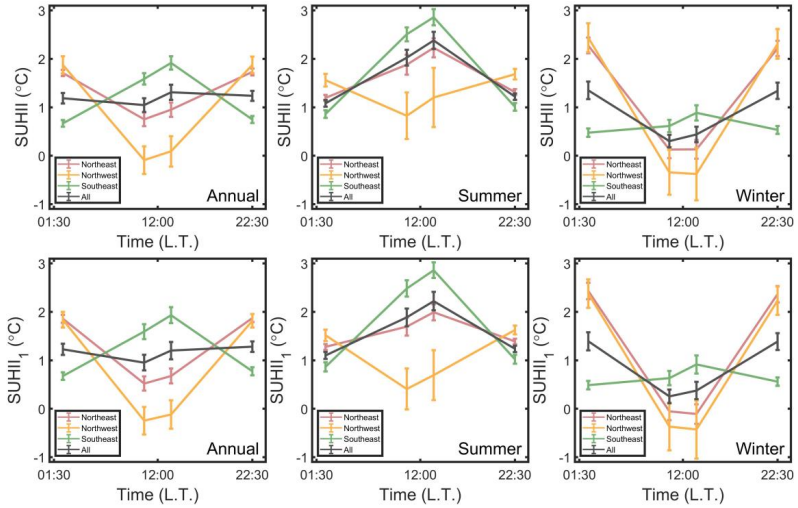

Figure 8. Cycles jour-nuit des moyennes annuelles, estivales et hivernales de SUHII et SUHII1 pour 34 villes chinoises de différentes régions. Les lignes pleines indiquent les valeurs moyennes, les barres d'erreur représentent la norme. errors.

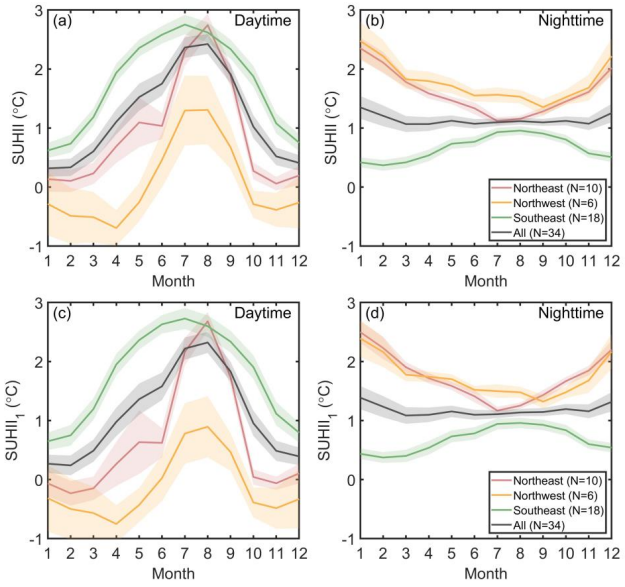

Figure 9. Variations du SUHII mensuel diurne et nocturne (SUHII et SUHII1) pour 34 villes chinoises dans différentes régions. Valeur moyenne indiquée par des lignes pleines, erreurs standard dans les zones ombrées.

6. Conclusions et perspectives

Compte tenu de la carence de la recherche mondiale multi-échelle et à long terme sur les SUHI et de l'incohérence des méthodes de quantification des SUHI, cette étude met en avant la nécessité d'enquêter sur le modèle spatio-temporel des SUHI mondiaux et sur leurs facteurs d'entraînement. Premièrement, l'ensemble des données SUHII mondiales sur la période 2003-2019 a été généré dans une optique de recherche exhaustive. Deuxièmement, le mécanisme d'entraînement du SUHI dans différentes régions géographiques et régions climatiques est moins concerné, ce qui fournira des indications ciblées pour les politiques d'atténuation dans la gestion urbaine. Sur la base du modèle de bilan énergétique de surface, le facteur déterminant pour le SUHI global d'un point de vue spatial et temporel, ainsi que la non-stationnarité spatiale ont été montré. Enfin, en construisant de nouveaux indicateurs quantitatifs pour l'intensité des SUHI, la faisabilité de la méthode classique de la différence de température entre les zones urbaines et rurales concernant l'ensemble de la référence rurale dans l'étude régionale des SUHI a été vérifiée.

Pour une meilleure interprétation du modèle spatial et temporel de SUHI, les SUHII positifs et négatifs pourraient être étudiés séparément. En outre, il est nécessaire d'évaluer les facteurs potentiels supplémentaires concernant les activités anthropogéniques et les paysages urbains. Les SUHII dérivés de la couverture complète des TSM devraient être spécifiquement concernés.

Références

Bai, X., Dawson, R. J., Ürge-Vorsatz, D., Delgado, G. C., Salisu Barau, A., Dhakal, S., Dodman, D., Leonardsen, L., Masson-Delmotte, V., Roberts, D. C., and Schultz, S., 2018. Six research priorities for cities and climate change. Nature. 555, 23-25.

Chakraborty, T. and Lee, X., 2019. A simplified urban-extent algorithm to characterize surface urban heat islands on a global scale and examine vegetation control on their spatiotemporal variability. Int J Appl Earth Obs. 74, 269-280.

Grimm, N. B., Faeth, S. H., Golubiewski, N. E., Redman, C. L., Wu, J. G., Bai, X. M., and Briggs, J. M., 2008. Global change and the ecology of cities. Science. 319, 756-760.

Zhou, D., Xiao, J., Bonafoni, S., Berger, C., Deilami, K., Zhou, Y., Frolking, S., Yao, R., Qiao, Z., and Sobrino, J. A., 2019. Satellite remote sensing of surface urban heat islands: Progress, challenges, and perspectives. Remote Sens. 11, 1-36.

TRAVAUX PUBLIES LORS DE LA THESE

Articles:

M. Si, Z.-L. Li, F. Nerry, Tang, B.-H. Tang, P. Leng, H., Wu, X. Zhang, and G. Shang. Spatiotemporal pattern and long-term trend of global surface urban heat islands characterized by dynamic urban-extent method and MODIS data. ISPRS Journal of Photogrammetry and Remote Sensing, 2022, 183: 321-335.

M. Si, B.-H. Tang, Z.-L. Li, F. Nerry, X. Zhang, and G. Shang. “An artificial neuron network with parameterization scheme for estimating net surface shortwave radiation from satellite data under clear sky--Application to simulated GF-5 data set,” IEEE Transactions on Geoscience and Remote Sensing, 2021, 59(5): 4262-4272.

Z.-L. Li, M. Si, P. Leng. “A review of remotely sensed surface urban heat islands from the fresh perspective of comparisons among different regions (Invited Review),” Progress In Electromagnetics Research C, 2020, 102: 31-46.

Proceedings:

M. Si, B.-H. Tang, R. Tang, H. Wu, Z.-L. Li, and G. Shang. “Estimation of net surface shortwave radiation from simulated Chinese Gaofen-5 satellite data,” 2019 IEEE International Geoscience and Remote Sensing Symposium, 2019: 1978-1981.

M. Si, B.-H. Tang, Z.-L. Li. “Estimation of land surface temperature from unmanned aerial vehicle loaded thermal imager data,” 2018 IEEE International Geoscience and Remote Sensing Symposium, 2018: 1210-1213.

Menglin SI

Etude globale des dynamiques spatio-temporelles et des facteurs déterminants des ilots de chaleur urbain

Résumé

Mots-clés: Surface d'îlot de chaleur urbain mondial, Dynamique spatio-temporelle, Facteurs moteurs, Google Earth Engine

Le phénomène d'îlot de chaleur urbain de surface (SUHI), qui constitue l'un des problèmes environnementaux thermiques urbains les plus graves, fait l'objet de recherches depuis des décennies. Cependant, la quantification de l'intensité de l'îlot de chaleur urbain (SUHII) est incohérente, en particulier dans les études mondiales à long terme. Les facteurs qui déterminent l'intensité de l'îlot de chaleur à l'échelle mondiale ne sont pas clairs en termes de tendance à long terme et de caractère spatial ou non stationnaires. La faisabilité de la détermination du SUHII pour de multiples types de sols doit être étudiée plus avant dans des études régionales. Compte tenu de ces problèmes, le SUHII global pour 1711 villes au cours de la période 2003-2019 a été quantifié par le schéma dynamique de l'étendue urbaine avec les ensembles de données de température de surface terrestre provenant des spectroradiomètres imageurs à résolution modérée Terra et Aqua par le biais de la plateforme Google Earth Engine. Le SUHII quotidien a été intégré pour décrire les SUHII annuels, estivaux et hivernaux pour le modèle global et les contrastes régionaux. En outre, le taux de changement interannuel des SUHII a été révélé. Le facteur déterminant pour les SUHII du point de vue spatial au point de vue temporel, et la non-stationnarité spatiale a été montré. De nouveaux indicateurs quantitatifs pour le SUHII ont été construits pour vérifier la faisabilité de la méthode de la différence de température urbaine-rurale dans l'étude régionale du SUHII.

Résumé en anglais

Keywords: Global surface urban heat island, Spatiotemporal dynamic, Driving factors, Google Earth Engine

As one of the most severe urban thermal environmental problems, the surface urban heat island (SUHI) phenomenon in the field of academic research has been focused for decades. However, the quantification of SUHI intensity (SUHII) is inconsistent especially in global long-term studies. The driving factors for global SUHI are unclear in terms of its long-term trend and spatial non-stationarity. The feasibility of SUHII under multiple rural land types need to be further investigated in regional studies. Given this, the global SUHII for 1711 cities during 2003–2019 was quantified by the dynamic urban-extent scheme with the land surface temperature datasets through the Google Earth Engine platform. The annual, summer, and winter SUHIIs are analyzed for the global pattern and regional contrasts. Further, the interannual changing rate of SUHIIs were revealed. The driving factor for SUHII from the spatial to the temporal perspectives, and the spatial non-stationarity were revealed. New quantitative indicators for the SUHII were constructed to verify the feasibility of the urban-rural temperature difference method in the regional study of SUHII.